UNCLASSIFIED

AD NUMBER

AD875549

NEW LIMITATION CHANGE

TO

Approved for public release, distribution unlimited

FROM

Distribution authorized to U.S. Gov't. agencies and their contractors; Critical Technology; APR 1970. Other requests shall be referred to School of Aerospace Medicine, Brooks AFB, TX.

AUTHORITY

SAM USAF ltr, 10 Sep 1976

THIS PAGE IS UNCLASSIFIED

THIS REPORT HAS BEEN DELIMITED
AND CLEARED FOR PUBLIC RELEASE
UNDER DOD DIRECTIVE 5200.20 AND
NO RESTRICTIONS ARE IMPOSED UPON
ITS USE AND DISCLOSURE.

DISTRIBUTION STATEMENT A

APPROVED FOR PUBLIC RELEASE;
DISTRIBUTION UNLIMITED.

AD 875549

Final Report - Part I

ATMOSPHERIC EFFECTS UPON LASER EYE SAFETY

By: WARREN B. JOHNSON WILLIAM E. EVANS EDWARD E. UTHE

Prepared for:

UNITED STATES AIR FORCE
SCHOOL OF AEROSPACE MEDICINE
AEROSPACE MEDICAL DIVISION
BROOKS AIR FORCE BASE, TEXAS

DDC
RECEIVED
OCT 20 1970

STANFORD RESEARCH INSTITUTE
Menlo Park, California 94025 · U.S.A.

Reproduced by the
CLEARINGHOUSE
for Federal Scientific & Technical
Information Springfield Va. 22151

STANFORD RESEARCH INSTITUTE
Menlo Park, California

Final Report - Part I *April 1970*

ATMOSPHERIC EFFECTS UPON LASER EYE SAFETY

STATEMENT #2 UNCLASSIFIED
This document is subject to special export controls and each transmittal to foreign governments or foreign nationals may be made only with prior approval of

By: WARREN B. JOHNSON WILLIAM E. EVANS EDWARD E. UTHE

Prepared for:

UNITED STATES AIR FORCE
SCHOOL OF AEROSPACE MEDICINE
AEROSPACE MEDICAL DIVISION
BROOKS AIR FORCE BASE, TEXAS

CONTRACT F41609-69-C-0001

SRI Project 7472

Approved by:

R. T. H. COLLIS, *Director*
Aerophysics Laboratory

RAY L. LEADABRAND, *Executive Director*
Electronics and Radio Sciences Division

Copy No. 26

ABSTRACT

The results of two laser scintillation experiments in the atmosphere are presented, as is a revised eye-hazard evaluation procedure incorporating these results. The objective of the research is to determine the influence of atmospheric thermal turbulence on laser eye safety.

The experimental work on a 3.5-km near-ground horizontal propagation path was designed to determine the effect of range upon laser scintillation magnitude, represented by the log intensity standard deviation (σ). It was found that for very short ranges and low thermal turbulence, the measured values (σ_m) agree well with theory (σ_t). However, for longer ranges and higher thermal turbulence, the values of σ_m reached a maximum value of approximately 1.25 at $\sigma_t = 2.50$, and then decreased beyond, fitting the empirical function $\sigma_m = \sigma_t/(1 + 0.16\,\sigma_t^2)$ fairly well. This "supersaturation effect" is quite significant in reducing eye-damage probabilities for typical ranges and thermal turbulence conditions.

The second experiment was an attempt to confirm that scintillation saturation occurs on a slant path between a ground-based laser and a receiver on an orbiting aircraft. Some evidence of saturation was found, but the effect was not clearly established because of the limited ranges necessitated by the laser used.

The eye-hazard evaluation procedure is quite generally applicable, and requires only readily available input data. The method covers propagation on a slant path with either a ground-based or airborne laser, as well as near-ground horizontal propagation. The airborne-laser slant-path configuration is shown to give the lowest eye-damage probability, other factors being the same.

CONTENTS

ABSTRACT iii

LIST OF ILLUSTRATIONS vii

LIST OF TABLES xiii

FOREWORD xv

I INTRODUCTION 1

II TECHNICAL BACKGROUND, SUMMARY OF RESULTS, AND RECOMMENDATIONS 5

A. Background and Summary of Results 5

B. Recommendations for Additional Research 8

III HORIZONTAL PROPAGATION EXPERIMENT 11

A. General 11

B. Site Description 12

C. Instrumentation 12

1. Laser Measurements 12

2. Meteorological Measurements 17

D. Experimental Procedures 22

E. Data Analysis 23

F. Results 28

1. Comparison of Scintillation Measurements with Theory 28

2. Log-Normality of Probability Distributions 37

3. Spectra of Scintillation 44

4. Comparison of Standard Deviations Obtained by Digital and Analog Processing 46

IV SLANT-PATH PROPAGATION EXPERIMENT 49

A. General 49

B. Site Description 49

C. Instrumentation 51

1. Laser Measurements 51

2. Meteorological Measurements 57

D. Experimental Procedures 57

E. Data Analysis 58

F. Results 63

1. Meteorological and Horizontal Control Path Measurements 63

2. Slant-Path Measurements 70

V INCORPORATION OF EXPERIMENTAL RESULTS INTO LASER EYE SAFETY GUIDELINES 79

A. General 79

B. Eye-Hazard Evaluation Procedure 79

C. Basis for Eye-Hazard Evaluation Procedure 91

D. Examples of Use of Eye-Hazard Evaluation Procedure. . . 96

Appendix--DERIVATION OF EQUATIONS FOR PROBABILITY OF EYE DAMAGE FROM A SINGLE EVENT 99

REFERENCES 103

DD Form 1473

ILLUSTRATIONS

Figure 1 Beam Pattern of Ruby Laser at 11.6 km 2

Figure 2 Location of Woodland Field Site 13

Figure 3 View of Woodland Field Site, Looking NW 14

Figure 4 Plan View of Woodland Field Site 15

Figure 5 Expanded View of Layout of Central Portion of Field Site 16

Figure 6 Control Receiver (Left) and Mobile Receiver Setup at 460 m 18

Figure 7 Block Diagram of Receiver System 19

Figure 8 Differential Thermometer, Utilizing 0.0005-inch Thermocouples 20

Figure 9 Micrometeorological Instrumentation at Woodland Field Site 21

Figure 10 Experimental Configuration for Phase 1 Horizontal-Path Experiments 22

Figure 11 Fifteen-Second Oscilloscope Time Exposures of Logged Signals from Mobile Receiver (Top Trace in Each Photograph) and Control Receiver at 460 m (Bottom Trace), on 27 November 1968. The Control Receiver Range is Given beneath Each Photograph. Vertical Scale 14 dB/Division, Horizontal Scale 10 ms/Division 27

Figure 12 Measured Relation Between the Log Intensity Standard Deviation at the Control Receiver at 460 m Range, and the Refractive Index Structure Constant (C_n) Derived from the Differential Thermometer Data 32

Figure 13 Comparison of Measured Values of Log Intensity Standard Deviation at the Mobile Receiver with Values Predicted by Tatarski's Theory, Showing the Supersaturation Effect 33

Figure 14 Measured (σ_m) Versus Theoretical (σ_t) Values of Log Intensity Standard Deviation, as Measured by Gracheva (1967) and Corrected by De Wolf (1968). The Curves Represent Various Theoretical Formulations by (A) Tatarski (1961), (B) Tatarski (1966), and (C) De Wolf (1968), Plus the Empirical Function Fitted to the SRI Data (D) 34

Figure 15 Measured Log Intensity Standard Deviation at the Mobile Receiver as a Function of Range, for Various Class Intervals of C_n 36

Figure 16 One-Minute Probability Distributions for (a) Control Receiver, and (b) Mobile Receiver at 3500 m Range, for Run 51 38

Figure 17 Composite Five-Minute Probability Distributions and Gaussian Fit for (a) Control Receiver, and (b) Mobile Receiver at 3500 m Range, for Run 51 . . 39

Figure 18 Comparison of Composite Probability Distributions for Control and Mobile Receivers for Run 51 40

Figure 19 Example of Change in Shape of Probability Distributions as Beam Drift Causes Detector Location to Change from Center to Edge of Beam (Run 12, Mobile Receiver, Range 2700 m) 41

Figure 20 (a) One-Minute and (b) Composite Five-Minute Probability Distributions for ΔT for Run 51 42

Figure 21 Example of Fit of Compound Normal Distribution to Observed ΔT Probability Distribution. (a) Fitted Compound Normal Distribution, (b) Components of Fitted Compound Normal Distributions. The Parameters n_1 and n_2 Represent the Total Number of Occurrences in Each of the Component Distributions 43

Figure 22 Approximate Analog Power Spectra for Cross-Path Wind Component of (a) 1 m/s, and (b) 4 m/s 45

Figure 23 Comparison of Standard Deviations Obtained by Digital and Analog Processing 47

Figure 24 Experimental Site Location at Brooks AFB. Three Aircraft Ground Tracks Used in the Experiment Are Shown 50

Figure 25 Site Layout for Slant-Path Experiment at Brooks Air Force Base 51

Figure 26 Laser Tracking Mount 53

Figure 27 (a) Broad View, and (b) Close-Up View of Laser Signal Receiver Installation in Window Opening of U.S. Air Force C-97 Aircraft 54

Figure 28 Airborne Receiver Aiming Assembly 55

Figure 29 (a) Airborne Receiver and Electronics Installation Inside C-97 Aircraft, and (b) Receiver Aiming Assembly in Operating Position 56

Figure 30 Experimental Configuration for Slant-Path Measurements 58

Figure 31 Examples of Slant-Path Laser Data from 20 April 1969 in the Form of 15-Second Oscilloscope Time Exposures of Signal Output from Log Amplifier . . . 61

Figure 32 Sample Histograms for Slant-Path Experiment Showing (a) Good Signal-to-Noise Ratio (SNR), and (b) Poor SNR 62

Figure 33 Log-Intensity Standard Deviation (σ_m) Measured on 350-m Horizontal Control Range Versus Refractive Index Structure Constant (C_n), for the Slant-Path Experiment 64

Figure 34 Time Variations on 19 April 1969 of (a) Laser Scintillation on 350-m Horizontal Control Range (σ_m), and (b) Thermal Turbulence Level [$\sigma(\Delta T)$] 65

Figure 35 Time Variations on 20 April 1969 of (a) Laser Scintillation on 350-m Horizontal Control Range (σ_m), and (b) Thermal Turbulence Level [$\sigma(\Delta T)$]. Downward Excursions of Traces Were Caused by Cloud Shadows Drifting Across Range 66

Figure 36 Initial Portion of Figure 35 on Enlarged Time Scale, Showing Degree of Correlation Between Laser Scintillation and Thermal Turbulence Level 67

Figure 37 Time Variations on 23 April 1969 of (a) Laser Scintillation on 350-m Horizontal Control Range (σ_m), and (b) Thermal Turbulence Level [$\sigma(\Delta T)$] . . . 68

Figure 38 Vertical Temperature Profiles Obtained During Slant-Path Experiment 71

Figure 39 Assumed Exponential Form for Vertical Profile of Normalized Refractive Index Structure Constant . . 72

Figure 40 Measured Log-Intensity Standard Deviation on the Slant Path as a Function of the Theoretical Value, Assuming Two Values of k in the Exponential Model $C_n = C_{no} \exp(-kz)$. The Dashed Curves Represent the Empirical Function Previously Fit to the Data from the Woodland Horizontal Propagation Experiment 75

Figure 41 Solar Elevation Angle (α) as a Function of Hour of Day and Latitude (ϕ) for Various Times of Year 80

Figure 42 Insolation Category (S) as a Function of Solar Elevation Angle (α) and Tenths of Opaque Cloud Cover (N) 81

Figure 43 Range Integral (A) as a Function of Range (R) and Slant-Path Elevation Angle (θ), for the Two Types of Slant Paths 84

Figure 44 Log-Intensity Standard Deviation (σ) as a Function of Range Integral (A) and Refractive Index Structure Constant (C_n), for Various Wavelengths (λ) of an Airborne or Ground-Based Laser 85

Figure 45 Log-Intensity Standard Deviation (σ) as a Function of Refractive Index Structure Constant (C_n) and Range (R), for Various Laser Wavelengths (λ) and a Near-Ground Horizontal Propagation Path 86

Figure 46 Normalized Mean Power Density ($\bar{I}/P$) as a Function of Beam Divergence Angle (β) and Range (R), for Various Values of Atmospheric Visibility (V) 87

Figure 47 Instantaneous Probability of Eye Damage (γ) as a Function of Log Intensity Standard Deviation (σ) and Safe-to-Mean-Power-Density Ratio ($I_{safe}/\bar{I}$) 90

Figure 48 Integrated Probability of Eye Damage (Γ) as a Function of Event Frequency (F) and Instantaneous Probability of Eye Damage (γ), for Three Different Exposure Times (T). 90

TABLES

Table I	Laser Data Summary, Woodland Experiment	24
Table II	Results from Woodland Data Processing	29
Table III	Means and Standard Deviations for Run 12 (Mobile Receiver)	41
Table IV	Chronological Summary, Slant-Path Experiment	59
Table V	Laser Data Summary, Slant-Path Experiment	60
Table VI	Reduced Slant-Path Data, April 1969 Experiment	74
Table VII	Relation of Near-Ground (2 m) Refractive Index Structure Constant (C_n) to Weather Conditions	82
Table VIII	Maximum Safe Power Density Levels (I_{safe}) for Corneal Exposures (Recommended by USAF Manual AFM 161-8, 1969)	89
Table IX	Examples of Laser Eye-Hazard Evaluation	97

FOREWORD

This research program was sponsored by the USAF School of Aerospace Medicine, Aerospace Medical Division, Brooks Air Force Base, Texas, under Contract No. F41609-69-C-0001. The project technical monitors were Lt. Col. J. A. Carpenter and Capt. P. D. Walker. The research was directed by Dr. W. B. Johnson of Stanford Research Institute, under the supervision of Mr. R. T. H. Collis, Director of the Aerophysics Laboratory.

Publication of this report does not constitute U.S. Air Force approval of its findings and conclusions.

The authors appreciate the help of Mr. N. Nielsen and Mr. D. F. Alves in the experimental work, Mr. H. Shigeishi in the computer programming, and Dr. A. Vassiliadis in furnishing advice regarding ocular laser damage threshold levels.

I INTRODUCTION

The rapid proliferation of laser systems for civilian and military applications urgently requires the development of suitable guidelines to ensure safety in their use. In the absence of appropriate and realistic guidelines, excessively conservative "safety factors" may be proposed that could unduly restrict the use of laser systems.

The U.S. Air Force is actively conducting and sponsoring research studies (1) to determine threshold levels for laser eye damage (Vassiliadis et al., 1969),* and (2) to determine the effects of atmospheric thermal turbulence on eye-damage probabilities. The latter is the objective of our present work and the subject of this report. A previous report (Johnson et al., 1968) described the results of the first year's research.

The effect of atmospheric temperature inhomogeneities in increasing eye-damage probabilities is exemplified in Figure 1, which illustrates the resulting characteristic breakup of a propagating laser beam. To a viewer, this appears as scintillation (fluctuations in intensity). The "hot spots," or areas of localized beam intensification, typically have intensities that are tens or hundreds of times the average beam intensity. Thus, as the state of the atmosphere changes from a thermally "quiet" situation (no scintillation) to one of increasing thermal turbulence and scintillation, the probability of laser eye damage increases drastically.

During the first year, substantial progress was made toward clarifying and parameterizing the effects of atmospheric thermal turbulence

---

*References are listed at the end of the report.

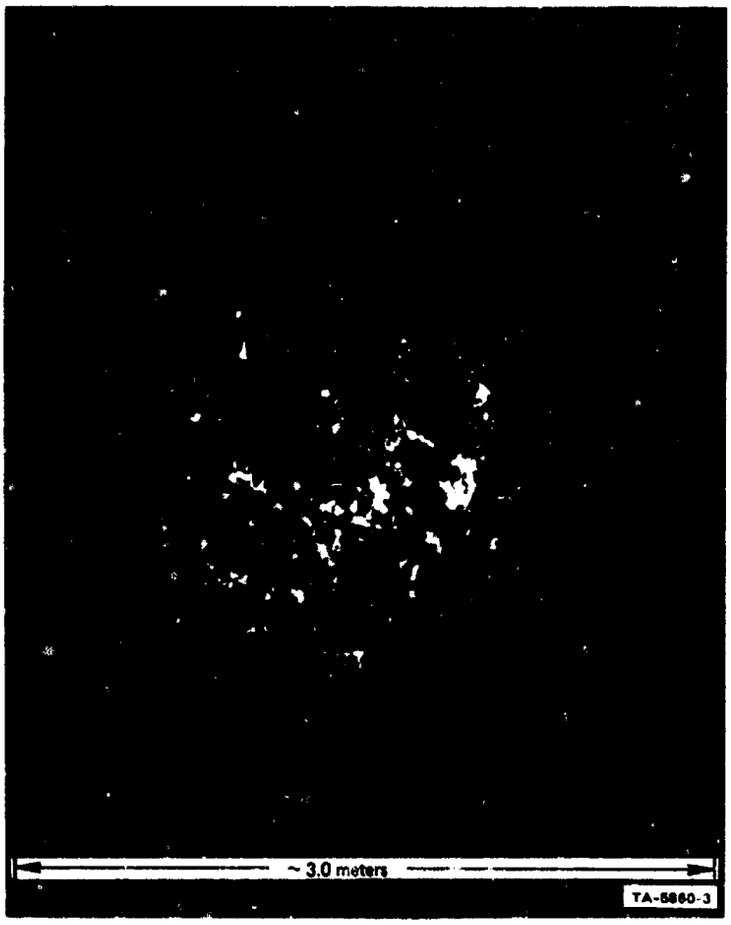

FIGURE 1 BEAM PATTERN OF RUBY LASER AT 11.6 km

upon laser propagation and upon the associated eye-damage probabilities. It was determined experimentally that the amplitude probability distribution of the laser intensity measured by a 5-mm-aperture detector is well described by a log-normal distribution, in accordance with Tatarski's (1961) theory. The results demonstrated that, although the observed probability distributions departed somewhat from log normal at the extreme upper end of the distribution (possibly because of the finite laser power), the assumption of a log-normal distribution gave safe (conservative) eye-damage probability estimates. These analyses were carried out to probabilities approaching 10^{-7}, almost three orders of magnitude lower than previously available.

Using the log-normal model, a preliminary set of laser safety guidelines for atmospheric effects were developed. These tentative guidelines are based upon readily available, conventional weather observations. However, a number of approximations had to be made in developing the guidelines, because of the basic lack of information. During the past year, additional experiments were carried out in order to clarify certain unresolved propagation effects and to permit the guidelines to be extended to a broader range of usage of laser systems in terms of path geometry, nature of the platform, and turbulence conditions. The results of this research and the incorporation of this information into the laser eye-safety guidelines are described in the remainder of this report. It should be emphasized that these safety guidelines should be considered tentative and used with caution until the new experimental results that they reflect can be confirmed for a variety of laser-beam and propagation-path configurations.

II TECHNICAL BACKGROUND, SUMMARY OF RESULTS, AND RECOMMENDATIONS

A. Background and Summary of Results

Classical optical propagation theory (Tatarski, 1961) predicts that the scintillation magnitude (σ_t) is directly proportional to thermal turbulence intensity (C_n), approximately directly proportional to range (R), and approximately inversely proportional to the square root of the optical wavelength; the exact form is

$$\sigma_t = K R^{11/12} (2\pi/\lambda)^{7/12} C_n \quad . \tag{1}$$

Here σ_t is the theoretical log signal intensity standard deviation, and K is a dimensionless constant. This theory, which is based on the so-called Rytov approximation, fits observations well for low-thermal-turbulence conditions and short ranges.

Application of the theory to longer ranges and higher turbulence levels has not been intuitively appealing, however, since for these conditions the predicted scintillation magnitude (and hence the eye-damage probability) increases indefinitely without bound. But no better theory has been available, and indeed, recent advances have come principally through experimentation.

The first breakthrough came from experiments in Russia by Gracheva and Gurvich (1965) and by Gracheva (1967), which showed a saturation, or levelling off, of the scintillation magnitude with increasing range beyond about 1 km. (The longest range at which measurements are reported in the Russian work is 1.75 km.) Subsequently, Tatarski (1966) and DeWolf (1968) developed variations of the propagation theory that conform to some degree to the Russian observations.

In November 1968, at an excellent site near Woodland, California, we carried out a horizontal propagation experiment designed primarily to check and extend the Russian results regarding the range dependence of the saturation magnitude. Our results, which cover a broad range of thermal-turbulence conditions and ranges out to 3.5 km, were surprising and are believed to be extremely significant in the context of the eye-safety problem. We found that, for our experimental conditions, the scintillation magnitude not only saturated with increasing range and thermal turbulence level (as represented by σ_t), but actually reached a peak and decreased thereafter--an effect that we have called "supersaturation." An analytical expression that fits our measured data well is

$$\sigma_m = \frac{\sigma_t}{1 + 0.16\,\sigma_t^2} \quad , \tag{2}$$

where σ_m is the measured log intensity standard deviation.

Subsequent to the horizontal propagation experiment, we learned that Deitz and Wright (1969) had reported some indications of such an effect in their data, which extended in range to 1.5 km. In addition, Mevers et al. (1969) reported in April 1969 that their data, which extended to 5 km, definitely shows a supersaturation effect; Ochs (1969) also hints of such an effect in his results. Thus, three or four independent experiments, in which the investigators were unaware of each other's results, have produced results that indicate the existence of the supersaturation phenomenon. Furthermore, a close examination of the Russian data reveals that they, too, reveal such a tendency within the limited range covered.

Other significant results obtained from the horizontal propagation experiment include the following:

(1) The frequency spectrum of the scintillation shifts to higher frequencies with longer range and increasing supersaturation, and tends to become bimodal.

(2) The intensity probability distribution remains approximately log-normal for both subsaturation and supersaturation conditions, for a detector centered in the laser beam.

(3) Systematic deviations from log-normal occur when the detector is not centered in the laser beam.

(4) Values of C_n derived from measurements with a fast-response differential thermometer system show excellent correlation with scintillation magnitude for subsaturation conditions, in accordance with Eq. (1). The constant K was determined to be 1.06.

A slant-path experiment using an orbiting aircraft was carried out in April 1969 at Brooks AFB. The quantity of data obtained (28 good runs in two days) was less than desired because of the limited availability of the aircraft. Some indications of saturation of scintillation on the slant path were found in the limited data sample obtained. The maximum range used was approximately 4000 m, which was not far enough to produce supersaturation. Saturation effects were observed on the horizontal control range at a distance of 350 m.

The pseudo-wind effects caused by the aircraft and laser-beam movement were readily apparent in the higher frequencies of scintillation on the slant path, typically greater than 1 kHz.

B. Recommendations for Additional Research

Although available information shows that the supersaturation effect definitely exists, the data from the experiments by various investigators do not agree in terms of the maximum scintillation magnitude and the rate of decrease of scintillation with increasing range and thermal turbulence level. The maximum scintillation magnitude (σ_m^*) effectively sets an upper limit for the eye-damage hazard (probability). Thus, it is particularly important for the eye-safety problem that σ_m^* be accurately determined, and that we determine the nature of any dependence upon propagation-path geometry (e.g., elevation), meteorological conditions, or laser characteristics. Additional measurements on the slant path and also at night under stable conditions are needed. Our laser safety guidelines in their present form must be considered tentative and used with caution until the characteristics of the supersaturation effect are determined for conditions other than those used in our experiments.

Present indications are that σ_m^* is a universal constant for a given laser and path configuration. However, it might be expected that σ_m^* would vary with path height, since the turbulence structure changes. Also, laser variables--such as transmitted beam diameter, divergence, and wavelength--might well have an effect, as mentioned by Kerr (1970). Mevers et al., (1969) have tentatively found that σ_m^* is less than half as large for a wavelength of 1.15 μ as it is for 0.514 μ. This wavelength dependency should be confirmed and further quantified.

The observed variation of scintillation frequency with saturation should also be examined in more detail, since eye damage depends upon the duration as well as the intensity of a pulse.

When sufficient data of this nature are available, they should be incorporated into a more comprehensive and accurate laser eye-safety guide. In view of the findings of our recent research, it is probable that previous guidelines can be safely revised to be less restrictive.

III HORIZONTAL PROPAGATION EXPERIMENT

A. General

The specific objectives of this experiment were as follows:

(1) To verify the existence and nature of the saturation effect with regard to optical scintillation, and to determine if the saturation level for increasing thermal turbulence is equivalent to that for increasing range under low-turbulence conditions.

(2) To check the quality of the log-normal fit to the probability distribution of the intensity fluctuations under saturation conditions.

(3) To establish firmer relationships between the meteorological conditions and the strength of the optical fluctuations.

Toward these ends, we carried out an experimental program to measure the intensity fluctuations in the horizontal beam from a 3-mW helium/neon laser at a height of 1.7 m above the ground. Two 5-mm-aperture receivers were used, one fixed at 460-m range and the other movable over a range from 460 to 3500 m. The fixed control receiver sampled the beam simultaneously with the mobile receiver by means of a small diagonal mirror, and thus served as a reference for each set of measurements at different ranges. In this way the control receiver supplemented the independent meteorological measurements in monitoring the meteorological conditions as the range was varied for the mobile receiver from run to run.

B. Site Description

As shown in Figure 2, the site selected for this experiment is located in an area of rice fields approximately midway between Woodland and Sacramento, California. The site and surrounding area are extremely level, with scattered low dikes and levees being the only significant relief. In addition, the ground cover is relatively uniform over much of the area. The particular field we used is approximately 2 × 5 km and had a recently plowed and smoothed bare surface. With this type of site, we could be reasonably confident that the meteorological conditions and thermal turbulence would be horizontally uniform; hence, meteorological measurements at a fixed location could be considered representative of the entire propagation path. Some idea of the flatness and uniformity of this site may be gained from the photograph in Figure 3. The detailed layout of the laser propagation path and instrumentation is illustrated in Figures 4 and 5.

C. Instrumentation

1. Laser Measurements

A Spectra-Physics Model 115 helium/neon laser (wavelength 6328 Å), with an output power of approximately 3 mW, was used for this experiment. The laser was positioned so that the beam was 1.7 m above the ground. Pointing was controlled by means of a precision table with micropositioners. Suitable beam-expanding optics were used to obtain a transmitted beam diameter of approximately 30 mm (between e^{-2} intensity points). Beam divergence was maintained at about 0.5 mrad (full angle), to give a 25-cm beam diameter at the control receiver range of 460 m, and a 190-cm beam diameter at the farthest mobile receiver range of 3500 m. A spatial filter with an aperture of 20μ was used to ensure a smooth mean (Gaussian) intensity profile across the beam.

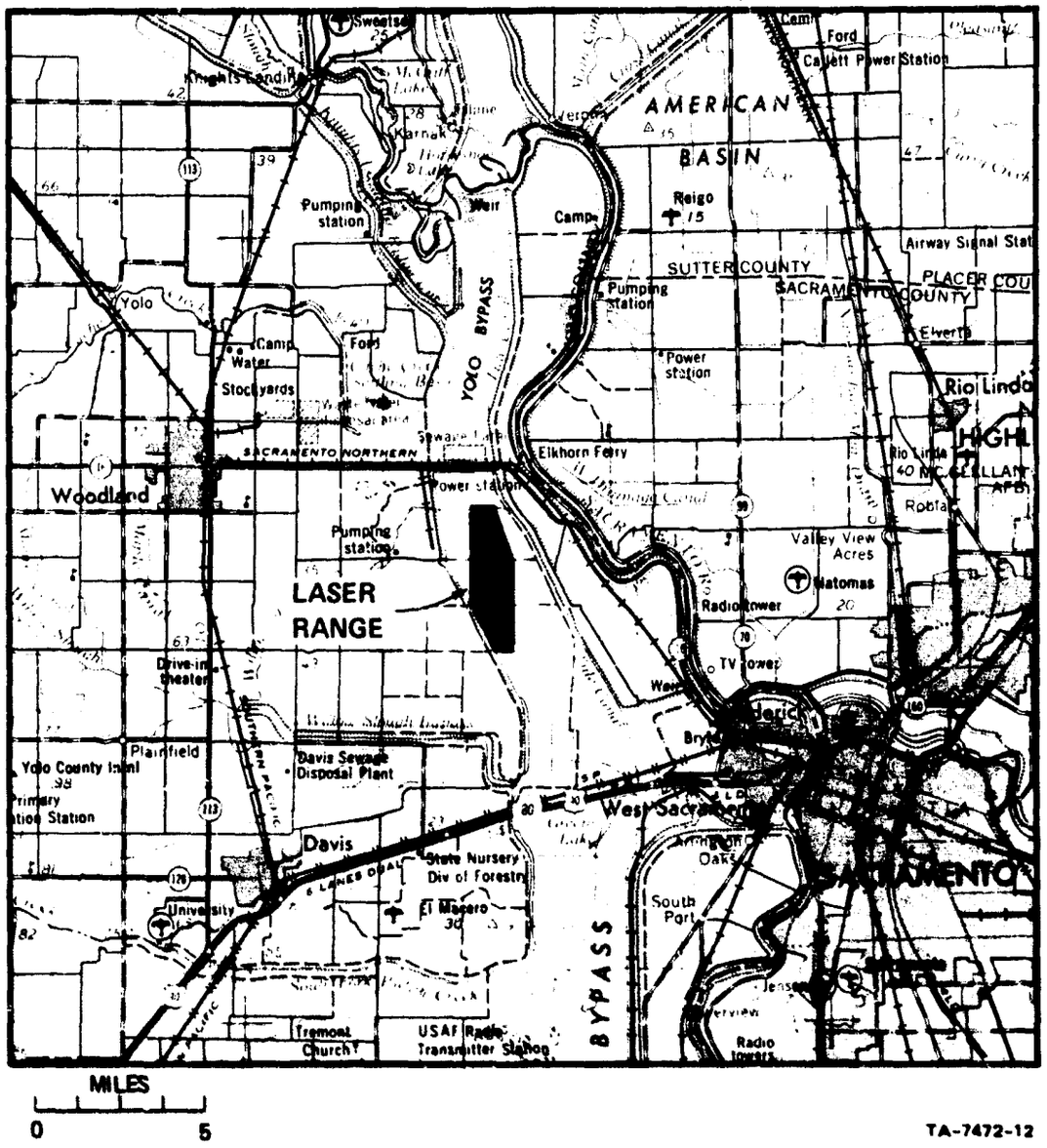

TA-7472-12

FIGURE 2 LOCATION OF WOODLAND FIELD SITE

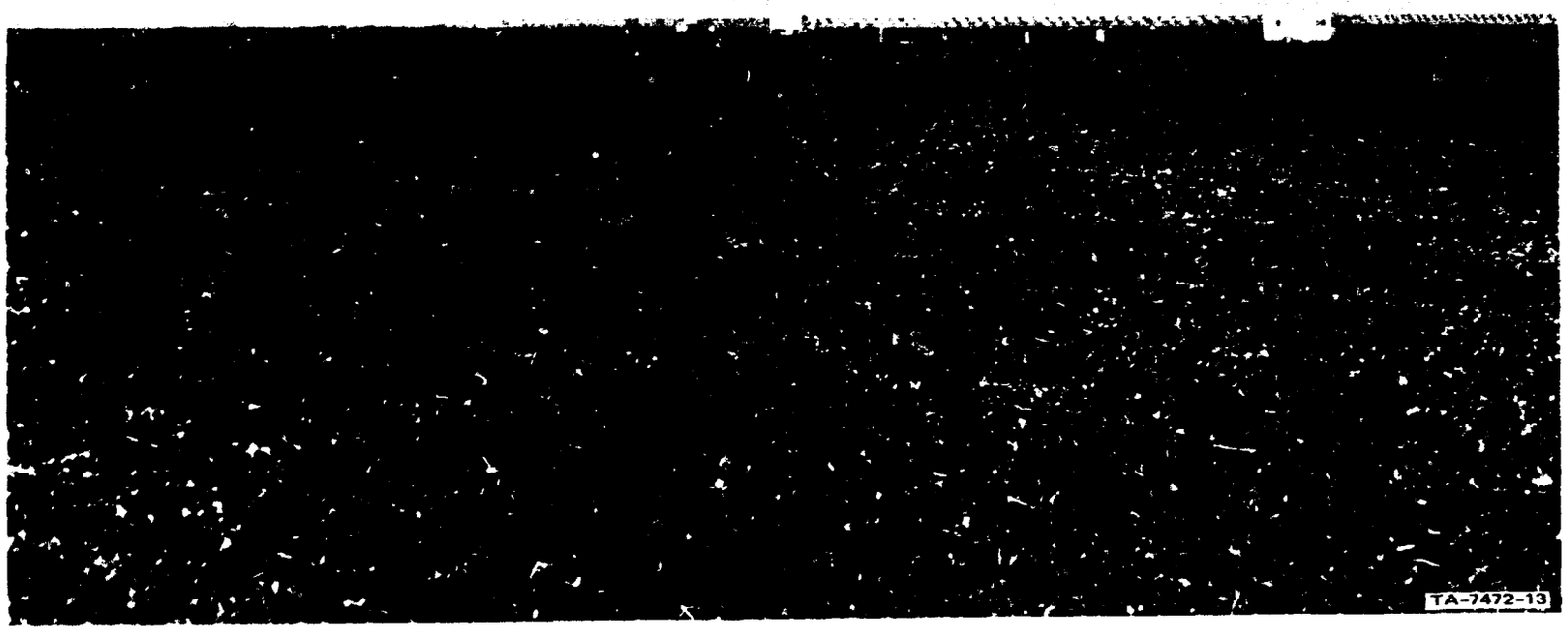

FIGURE 3 VIEW OF WOODLAND FIELD SITE, LOOKING NW

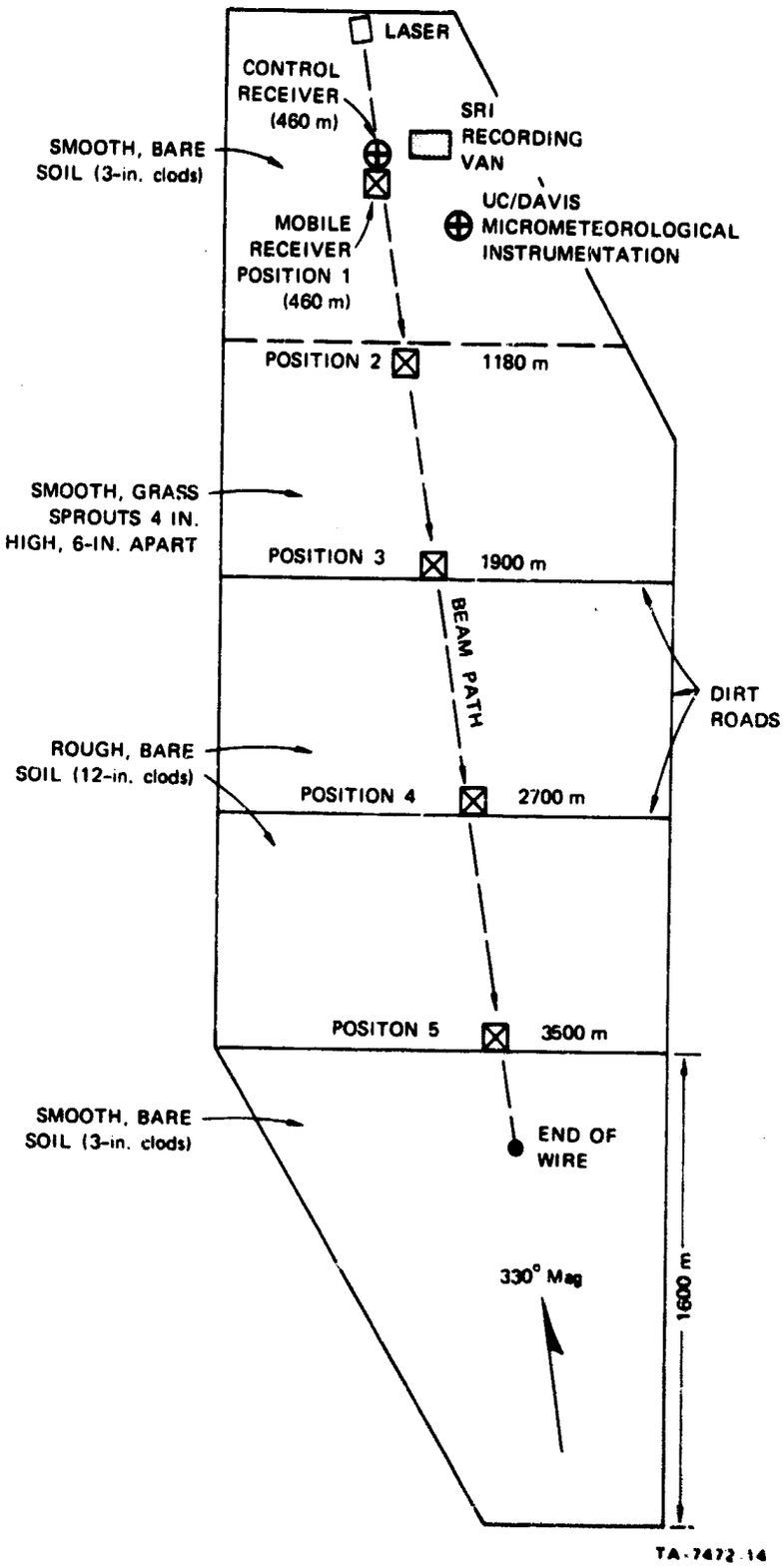

FIGURE 4 PLAN VIEW OF WOODLAND FIELD SITE

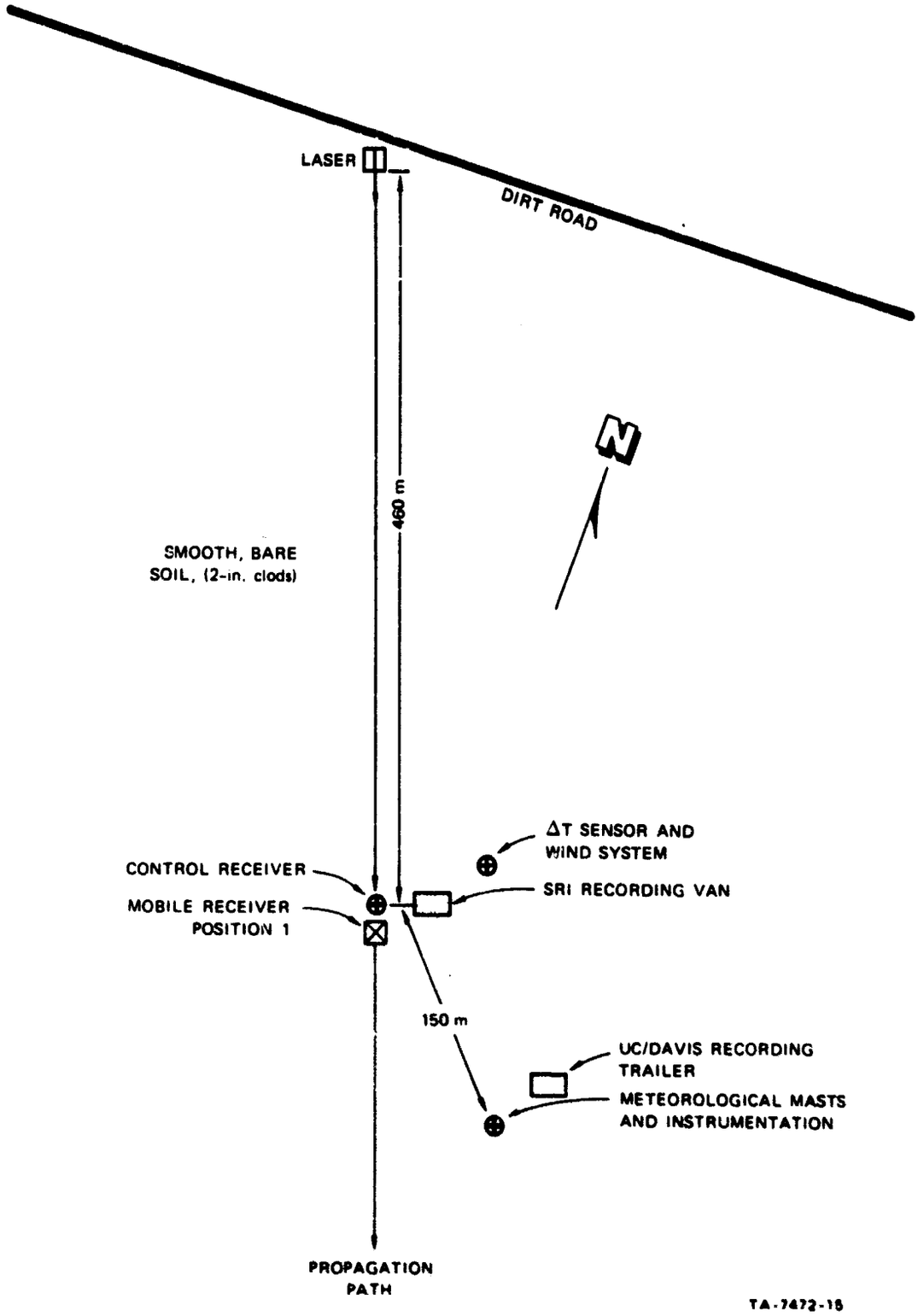

FIGURE 5 EXPANDED VIEW OF LAYOUT OF CENTRAL PORTION OF FIELD SITE

Two essentially identical receivers were used in the experiment to measure the signal simultaneously at two ranges. As shown in Figure 6, the control receiver assembly was fitted with a 2-cm-diameter diagonal mirror so that the main portion of the receiver could be positioned outside of and at right angles to the beam propagation path. The basic receiver system is illustrated in Figure 7. Each receiver employed a 5-mm diameter aperture (to simulate the average size of a human eye pupil), and a 10 Å interference filter to reduce background radiation. An RCA Model 7265 photomultiplier tube (PMT) with an S-20 photocathode surface was used in each receiver. The output signal from the PMT was fed into a logarithmic amplifier, whose output was then recorded in FM mode on an analog magnetic tape recorder. The mean PMT output current was monitored by a meter using an R-C network with a time constant of approximately seven seconds.

2. Meteorological Measurements

The primary meteorological instrument was a fast-response differential thermometer (Figure 8) designed to furnish a measurement of the temperature structure function. The mechanical design of the instrument was patterned after the differential thermometer used by Wright and Schutz (1967). In both instruments a vane is used to maintain the orientation of two horizontally separated temperature sensors perpendicular to the wind direction. However, in our device we used two 0.0005-inch-diameter chromel-constantan thermocouples, physically separated by 30 cm but electrically connected in series. The voltage generated by the temperature difference between the thermocouples (64 μ V/°C, as determined from repeated calibration tests) is then amplified by a high-gain differential amplifier (Tektronix Model 1A7A) and recorded in FM mode on an analog magnetic tape recorder. The time constant of the differential thermometer was determined experimentally

FIGURE 6 CONTROL RECEIVER (LEFT) AND MOBILE RECEIVER SET-UP AT 460 m RANGE

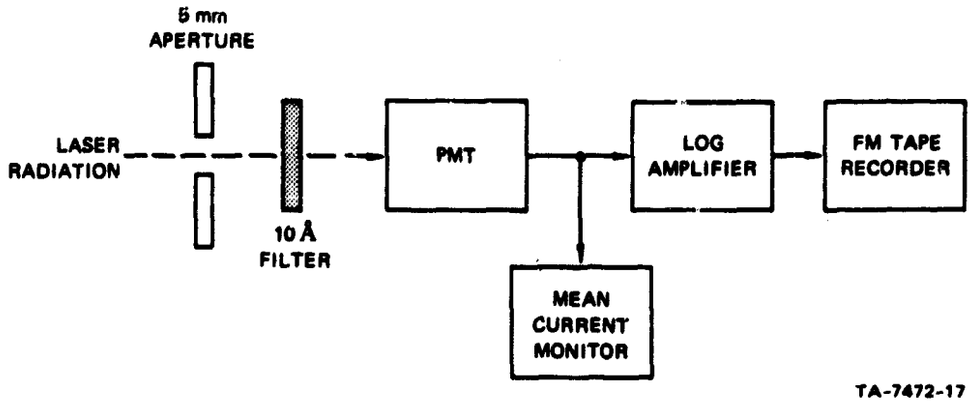

FIGURE 7 BLOCK DIAGRAM OF RECEIVER SYSTEM

to be 0.015 s when ventilated at 2 m/s. This response is fast enough so that the error in the computed fluctuation variance caused by neglecting higher frequencies should be small.

The differential thermometer was installed on a mast at the approximate laser beam level (1.7 m) near the control receiver, 460 m from the laser. Also located at this point were an anemometer and vane for measuring mean wind velocity.

Extensive supplementary micrometeorological measurements were obtained under subcontract by the Department of Water Science and Engineering of the University of California at Davis. Their instrumentation installation (Figure 9) included Thornthwaithe anemometers at five levels and aspirated temperature sensors at nine levels to furnish detailed wind and temperature profiles up to 4-m height. These measurements were later used to compute Richardson numbers to serve as estimates of atmospheric stability. Additional measurements included soil temperature and water vapor vertical gradients, and net radiation. These were used to establish the surface heat budget and the vertical heat flux.

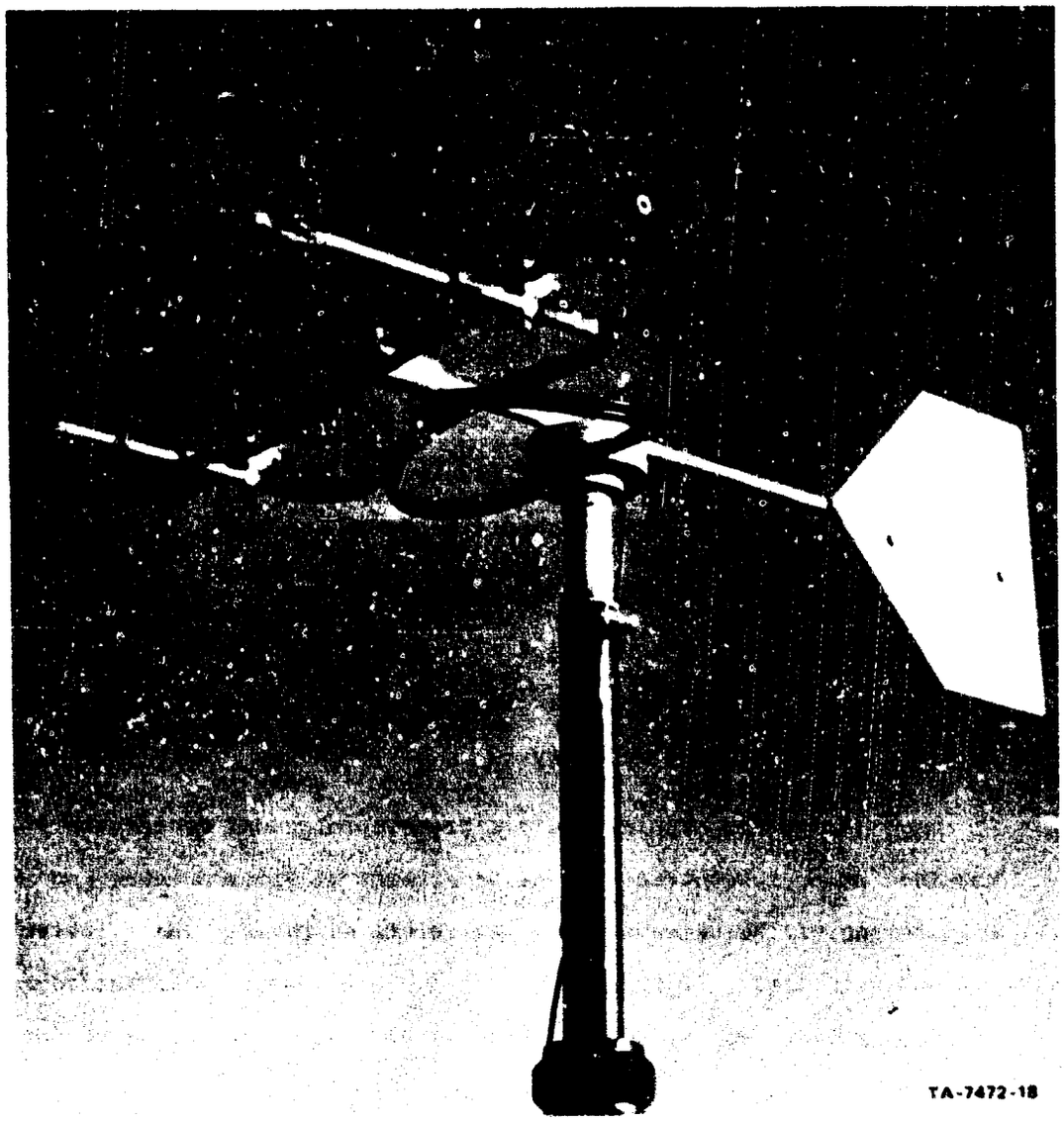

FIGURE 8 DIFFERENTIAL THERMOMETER, UTILIZING 0.5-MIL THERMOCOUPLES

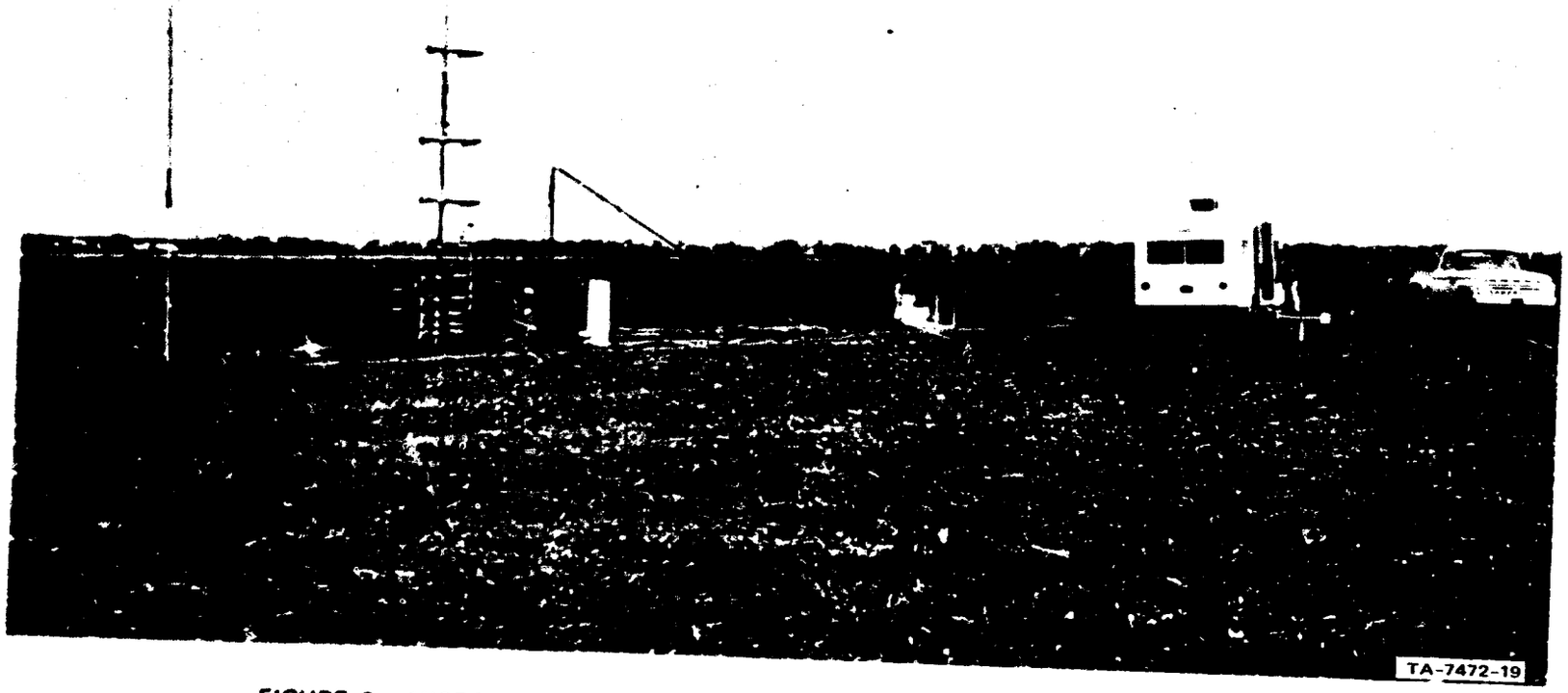

FIGURE 9 MICROMETEOROLOGICAL INSTRUMENTATION AT WOODLAND FIELD SITE

D. Experimental Procedures

The basic experimental configuration is illustrated in Figure 10. The control receiver was located 460 m from the laser, and five positions were established for the mobile receiver: 460, 1180, 1900, 2700, and

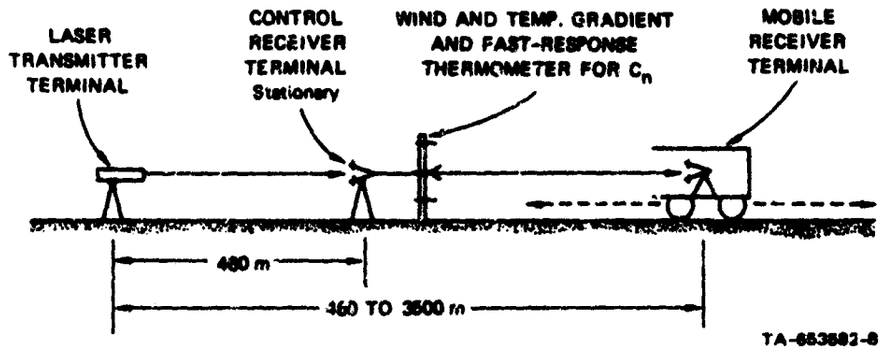

FIGURE 10 EXPERIMENTAL CONFIGURATION FOR HORIZONTAL-PATH EXPERIMENT

3500 m from the laser. The signal inputs from the two receivers and the differential thermometer were brought into a central recording van, which was located at about 500 m range, near the control receiver and the meteorological tower. The signal from the mobile receiver was brought back in FM mode from the various receiver positions by means of a 3-km length of field wire, with taps at the appropriate ranges. In this way, dependable low-noise data recordings were obtained.

The experimental technique consisted of 5-minute runs with both receivers measuring the signal simultaneously at different ranges. The mobile receiver was moved from one point to the next point between runs by means of a light truck, which housed the electronics. After completing a run, the truck was driven to the next point, the receiver was aligned and connected to the signal wire, 10 seconds of 60-Hz test signal was transmitted, and then the recording of a 5-min run, including calibration levels, was begun. This procedure, from the start of one run to

the start of the next, took approximately 15 to 20 min. The runs where the mobile receiver was at the same range as the control receiver served to furnish a comparison of the two outputs, which should be equivalent at the same range.

Prior to each run, the PMT supply voltage on each receiver was adjusted to give an approximate mean output current of 10 μA. The log amplifiers were adjusted to give zero output for an input of 10 μA, so that the means of the recorded (logged) signals would be near zero.

E. Data Analysis

As detailed in Table I, a total of 89 five-minute experimental runs (less three aborted runs) were recorded during the period 10-27 November 1968. These data were processed by both analog and digital techniques. The primary aim was to compute the standard deviation of the signal in each of the three channels--control receiver, mobile receiver, and differential temperature (ΔT)--for each of the runs.

A Meteorology Research Incorporated "Sigma Meter" was used for the analog processing. This is a two-channel device that half-wave rectifies the incoming signal, takes the average of the rectified signal (which represents $\overline{|V|}$, the average signal deviation from the mean), and then determines the standard deviation σ from the relation $\sigma = 1.25\ \overline{|V|}$, which holds for a Gaussian distribution. The time constant for the Sigma Meter is about 30 s for the particular averaging time selected.

Since past work has repeatedly shown that measured log intensity amplitude probability distributions conform well to Gaussian distributions, the restriction of the Sigma Meter on distribution shape did not affect the standard deviations computed for the two laser signal channels. However, it was found that the ΔT distributions were non-Gaussian, and hence the output of the analog computer was not a true

Table I

LASER DATA SUMMARY, WOODLAND EXPERIMENT

Exp. No.	Date	(PST) Start Time	Rec. Site	Weather	Tape No.	(μV/cm) ΔT Sens.	Remarks
1-A	11/10/68	1546	1	○10 160/10	1	20	Foggy earlier
1-B		1615	2	○10 200/3		20	
1-C		1636	3	/◐ 15		20	
2-A	11/11/68	1331	1	100◍/◍5H 160/10+15		20	
3		1350	1	Same		10	Abort
4		1353	1	Same		10	
5		1412	2	100⊕5H 180/10		10	
6		1433	3	Same		10	
7		1459	4	Same		10	
8		1524	5	100⊕5H 180/15		10	ΔT small
9	11/12/68	1115	1	○25 315/5	2	50	
10		1133	2	Same		50	
11		1155	3	○25 330/10		50	
12		1222	4	○25 330/7		50	
13		1249	5	Same		50	
14		1344	5	Same		50	
15		1404	4	○25 320/7		50	
16		1434	3	Same		20	
17		1456	2	Same		20	
18		1512	1	○25 330/10		20	Ch.B low cal. noisy
19		1540	5	Same		10	
20	11/13/68	1327	1	○15 300/20+25	3	20	
21		1343	2	Same		20	
22		1403	3	/◐V◍ 15 300/20+25		20	
23		1422	4	Same		10	
24		1448	5	Same		10	ΔT small
25		1501	5	Same		10	
26		1532	4	/◐V◍ 15 300/15+20		10	ΔT very small
27		1609	3	Same		10	
28		1627	2	Same		10	
29		1644	1	/◐V◍ 15 290/13+16		20	Ch.B atten. accid. moved
30	11/14/68	0917	1	150◍/⊕15 150/5	4	10	
31		0930	2	150◍/⊕15 135/8		10	
32		0944	3	Same		10	UC/Davis off
33		1012	-5-	150◍/⊕15 140/6		10	
34		1032	3	Same		10	UC back on
35		1049	2	150◍/⊕15 150/7		10	
36		1103	-1-	150◍/⊕15 150/7		10	
37		1122	2	Same		10	Temp. 48° F
38		1137	3	Same		10	
39		1152	4	Same		10	
40		1210	-5-	150◍/⊕15 135/6		10	5 min. extra run on recorder
41		1224	4	Same		10	Ch. B cals. 10 x slow
42		1241	3	Same		10	
43		1254	2	80⊕7 140 6		10	
44		1307	1	Same		10	Light rain beginning

Table I (Continued)

Exp. No.	Date	(PST) Start Time	Rec. Site	Weather	Tape No.	(μV/cm) ΔT Sens.	Remarks
45	11/25/68	1005	1	○20 320/5	5	20	Abort
46		1012	1	○25 300/7		20	
47		1026	2	○20 315/6		20	
48		1042	3	Same		20	Abort
49		1052	3	○20 300/8		20	
50		1156	4	○20 300/15		20	Run called 51 on tape
51		1215	-5-	○20 300/15+20		20	
52		1232	4	○20 300/16+22		20	
53		1249	3	○20 310/15+22		20	
54		1302	2	○20 310/16+22		20	
55		1317	1	Same		20	Neg. spikes Ch. B
56		1404	1	Same		20	
57		1429	2	○20 315/15+20		10	ΔT small
58	11/26/68	0836	1	/◐20 020/7	6	10	
59		0854	2	/◐20 350/5		20	
60		0912	3	Same		20	
61		0937	4	Same		20	
62		0955	-5-	/-◐20 045/4		20	
63		1011	4	/-◐20 030/6		20	
64		1033	3	/-◐20 030/5		20	
65		1046	2	/-◐20 315/3		20	Spikes Ch. B
66		1158	-1-	/-◐20 360/10		20	
67		1214	2	/-◐20 330/12		20	Spikes Ch. B
68		1230	3	/-◐ 330/12+16		20	
69		1252	4	/-◐ 320/12+16		20	
70		1310	4	/-◐ 315/10		20	Beam ht. exp.
71		1330	-5-	/-◐20 320/12		20	
72		1351	4	/ ◐20 360/10		10	
73		1441	3	Same		10	
74		1424	2	/ ◐20 325/6		10	ΔT small
75		1436	1	/ ◐20 315/3		10	ΔT very small
76	11/27/68	1058	1	X1/3GF 310/5	7	20	Sun dimly vis.
77		1124	2	-X/-◐2GF 325/5		20	
78		1203	3	/-◐10 330/5		20	
79		1219	1	○10 330/3		20	
80		1243	-5-	/-◐10 330/3		20	
81		1257	4	/-◐15 325/6		20	
82		1311	3	/-◐15 325/8		20	
83		1322	2	/-◐15 320/11		20	
84		1345	-1-	/-◐15 020/8		20	Fuse changed
85		1358	2	/-◐15 020/7		20	Cal. timing off
86		1409	3	/-◐10 045/7		20	
87		1426	4	/-◐10 040/8		20	
88		1442	5	/-◐10 040/7		20	

measure of the standard deviation. The ΔT signal is quite intermittent, with quiet periods alternating with disturbed periods as the wind brings pockets of warm air past the sensor. This gives rise to a highly lepto-kurtic frequency distribution, as will be illustrated in the next section.

The problem with the ΔT distribution necessitated reprocessing the data in digital fashion. Since it took little additional effort, the two laser signal channels were reprocessed as well as the ΔT channel. The procedure involved digitizing each channel at a sampling rate of approximately 2000 samples/s, and then compiling the signal amplitudes into 256-cell histograms, from which means and standard deviations could be computed. In order to reduce the influence of any trends in the mean levels upon the standard deviations, each run was broken up into approximate 1-min segments. The means of each of these segments were then used to correct for any trends, and a composite distribution with a common mean was formed from the segment distributions. The standard deviation of this composite distribution was then taken to represent the entire five-minute run.

Several of the runs were also processed using a bank of third-octave filters to obtain approximate analog power spectral distributions. The power spectra were used to determine the dominant frequencies in the signals on each of the three channels.

Each of the signals was monitored in the field on an oscilloscope (CRO). It was found desirable to take Polaroid photographs of a short time sample of each signal as displayed on the CRO, for later use in examining and editing the data. An example of one series of such CRO time exposures is given in Figure 11. The width of the signal envelope is approximately proportional to the standard deviation. It may be noted in the figure that while the width of the signal envelope for the control receiver remains about the same from run to run, that for the

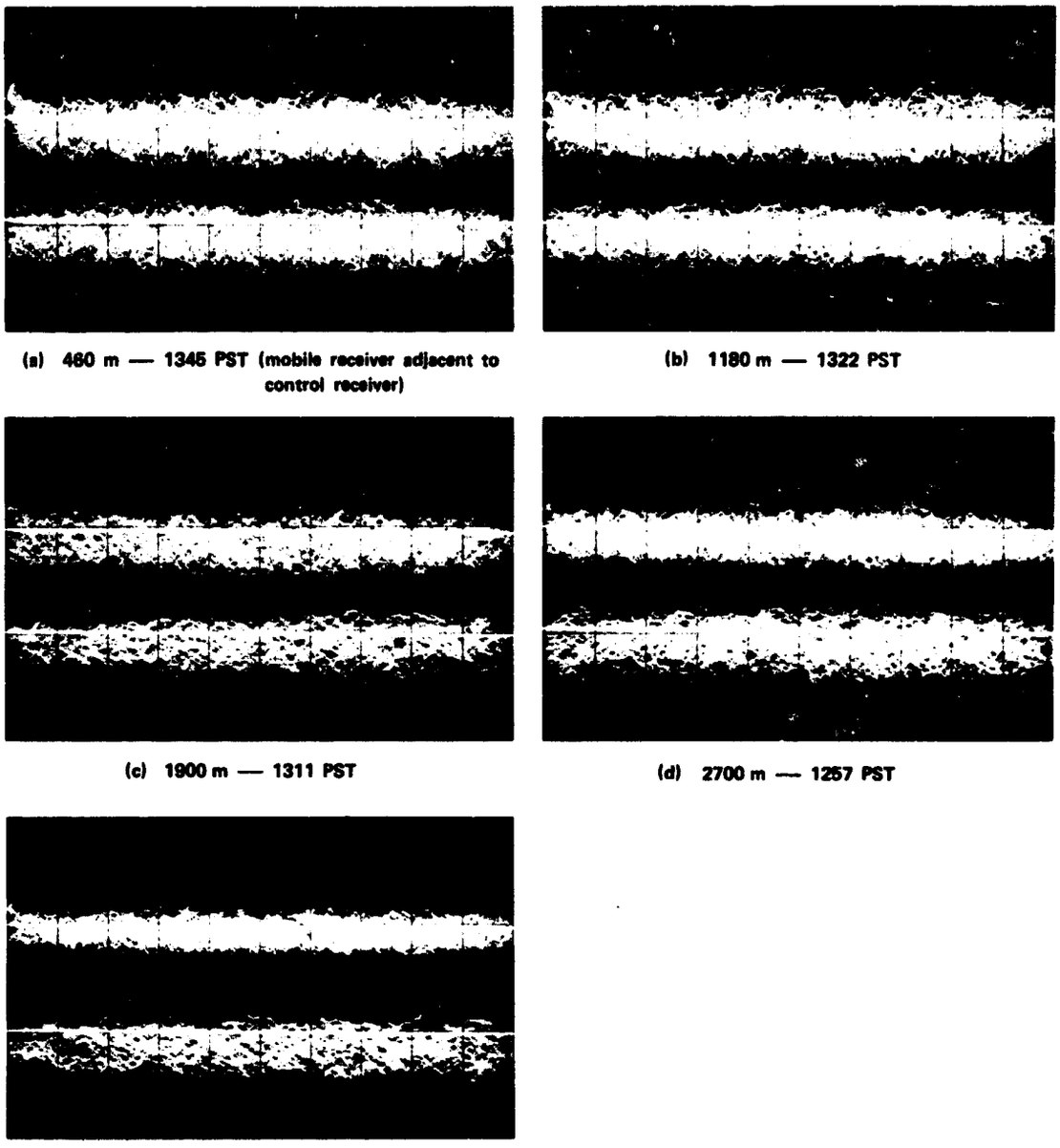

(a) 460 m — 1345 PST (mobile receiver adjacent to control receiver)

(b) 1180 m — 1322 PST

(c) 1900 m — 1311 PST

(d) 2700 m — 1257 PST

(e) 3500 m — 1243 PST

TA-7472-20

FIGURE 11 FIFTEEN-SECOND OSCILLOSCOPE TIME EXPOSURES OF LOGGED SIGNALS FROM MOBILE RECEIVER (TOP TRACE IN EACH PHOTOGRAPH) AND CONTROL RECEIVER AT 460 m (BOTTOM TRACE), ON 27 NOVEMBER 1968. The control receiver range is given beneath each photograph. Vertical scale 14 dB/division: Horizontal scale 10 ms/division.

mobile receiver decreases with increasing range. This feature of the data will be discussed in the next section.

F. Results

1. Comparison of Scintillation Measurements with Theory

The analysis procedure described in the preceding section yielded values of the standard deviations of the two (log-amplified) signals from the control and mobile laser receivers, and of the signal from the differential thermometer (ΔT). These values are listed in Table II.

The measurements of $\sigma(\Delta T)$ were used to derive values of C_n, the refractive index structure constant, in the following manner. The temperature structure function D_T is defined as

$$D_T = \overline{(T_1 - T_2)^2} = \sigma^2(\Delta T) \quad . \tag{3}$$

The well confirmed Kolmogorov "two-thirds law" predicts that in the inertial subrange,

$$D_T = C_T^2 \, r^{2/3} \quad , \tag{4}$$

where C_T is the temperature structure constant and r is the distance between measurement points. Thus

$$C_T = \sigma(\Delta T) \, r^{-1/3} \quad . \tag{5}$$

It can easily be shown that the structure constants for refractive index and temperature are essentially proportional and related by

$$C_n = (79 \times 10^{-6}) \, (p/T^2) \, C_T \quad , \tag{6}$$

Table II

RESULTS FROM WOODLAND DATA PROCESSING

Run No.	σ_m (control), dB†	σ_m (mobile), dB	$\sigma(\Delta T)$, °C
1A	1.19	1.23	0.055
1B	0.80	1.62	0.051
1C	1.20	3.61	0.060
2	4.32	3.45	0.187
4	3.48	3.39	0.133
5	2.61	4.98	0.103
6	1.34	4.26	0.057
7	0.68	2.33	0.038
8	0.25	2.52	0.019
9	5.30	5.20	0.301
10	5.37	5.52	0.302
11	5.20	4.04	0.297
12	5.29	3.64	0.323
13	5.13	**	0.304
14	4.72	3.44	0.243
15	4.16	3.44	0.202
16	3.22	4.59	0.158
17	2.31	4.87	0.119
18	1.74	1.97	0.088
19	0.66	3.83	0.035
20	3.40	3.67	0.165
21	3.41	4.81	0.160
22	2.83	4.63	0.131
23	2.44	4.77	0.104
24	1.14	5.14	0.047
25	0.84	4.14	0.035
26	0.44*	**	0.016*
27	1.35*	4.40*	0.058*
28	1.96*	4.25*	0.089*
29	2.38*	2.49*	0.106*
30	2.01	2.24	0.098
31	2.24	5.28	0.086
32	2.38	6.06	0.105
33	2.28	5.18	0.101
34	2.17	5.49	0.107
35	2.07	5.21	0.102
36	2.16	2.39	0.107
37	1.99	5.23	0.092
38	1.86	5.56	0.077
39	1.63	5.60	0.074
40	1.05	5.30	0.053
41	0.60	2.56	0.030

†Divide values by 4.34 to convert from dB to conventional natural logarithms

*Stable conditions (surface-based temperature inversion)

**Data missing or invalid

Table II (Continued)

Run No.	σ_m (control), dB	σ_m (mobile), dB	$\sigma(\Delta T)$, ^oC
42	0.51	1.85	0.030
43	0.51	1.31	0.027
44	0.52	0.57	0.029
46	5.14	5.46	0.261
47	4.73	5.16	0.260
49	5.38	4.60	0.266
50	4.83	4.30	0.247
51	4.61	3.55	0.220
52	4.37	4.00	0.203
53	4.15	4.49	0.183
54	4.12	4.85	0.179
55	4.03	2.89	0.181
56	2.74	2.85	0.112
57	1.91	**	0.074
58	1.62	1.75	0.085
59	2.49	5.33	0.145
60	2.85	5.74	0.141
61	3.18	5.07	0.170
62	4.41	3.50	0.180
63	4.44	4.06	0.204
64	3.60	5.30	0.190
65	4.29	**	0.211
66	4.40	4.50	0.211
67	4.27	**	0.206
68	4.23	4.95	0.203
69	2.74	5.38	0.122
70	2.02	5.27	0.085
71	2.24	5.13	0.102
72	1.23	5.02	0.051
73	1.29	4.42	0.044
74	0.79	2.01	0.028
75	0.86	0.92	0.029
76	4.96	5.37	0.217
77	5.46	5.69	0.199
78	5.37	4.78	0.268
79	5.48	3.70	0.251
80	5.18	2.80	0.288
81	5.40	4.08	0.274
82	5.23	4.61	0.268
83	4.58	5.06	0.237
84	4.84	5.00	0.216
85	4.59	5.82	0.217
86	4.59	4.97	0.190
87	3.93	4.81	0.183
88	3.39	4.53	0.155
89	0.86	**	0.046

where p is atmospheric pressure in millibars and T is absolute air temperature in °K. Combining Eqs. (5) and (6), we have

$$C_n = (79 \times 10^{-6})\ (p/T^2)\ (r^{-1/3})\ \sigma(\Delta T) \quad . \tag{7}$$

Based upon a value for r of 30 cm for our differential thermometer, which is the distance between the thermocouple probes, and a typical value of 1000 millibars for p, we obtain

$$C_n = 0.116\ \sigma(\Delta T)\ /T^2 \quad , \tag{8}$$

where $\sigma(\Delta T)$ and T are in units of °K and C_n is in units of $m^{-1/3}$. This is the equation that was used to calculate C_n.

The derived values of C_n are plotted versus the measured log intensity standard deviations at the control receiver, σ_m (control), in Figure 12. The control receiver was always at a fixed range of 460 m. The dashed line in the figure is the least-squares fit to the data for $C_n < 0.35 \times 10^{-6} m^{-1/3}$. Values for higher C_n show evidence of saturation, even at the 460 m range, and hence were excluded from the fit, although they are shown on the plot. Knowing that the range R is 460 m, and that the wavelength λ is 0.6328μ, the slope of the fitted line can be used to derive the coefficient in Tatarski's theoretical expression for log-normal scintillation, σ_t (Eq. 1). The fitted form of the equation comes out to be

$$\sigma_t = 1.06\ R^{11/12}\ (2\pi/\lambda)^{7/12}\ C_n \quad . \tag{9}$$

Tatarski gives theoretical values that yield comparable coefficients of 1.11 for a plane wave and 0.72 for a spherical wave. The measured value of 1.06 agrees well with these values.

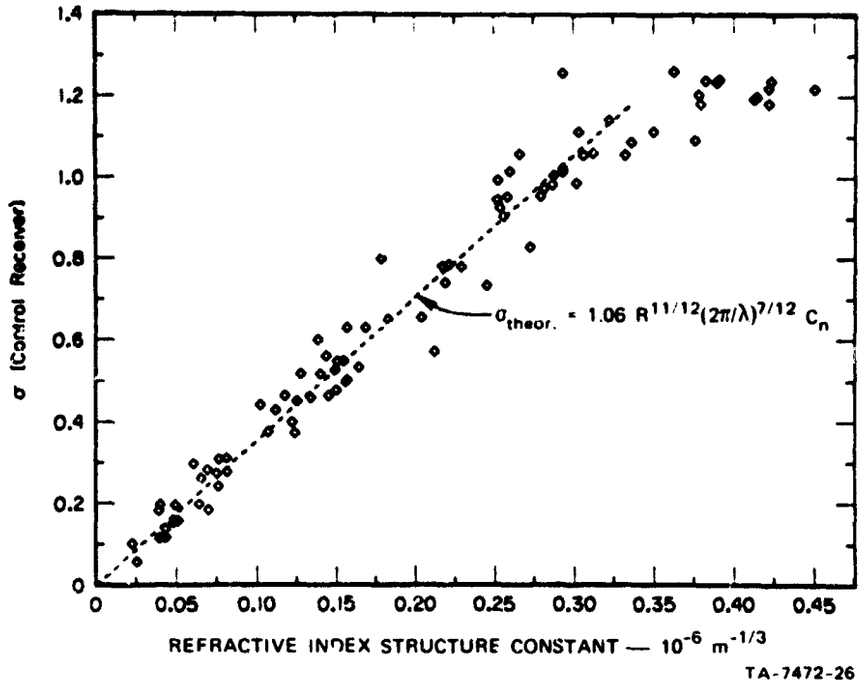

FIGURE 12 MEASURED RELATION BETWEEN THE LOG INTENSITY STANDARD DEVIATION AT THE CONTROL RECEIVER AT 460 m RANGE, AND THE REFRACTIVE INDEX STRUCTURE CONSTANT (C_n) DERIVED FROM THE DIFFERENTIAL THERMOMETER DATA

The striking feature of Figure 12 is the good fit obtained to Tatarski's equation for short range and small-to-moderate values of C_n. The scatter of the data points is fairly small, considering that (1) the measurements for σ_m (control) and C_n were obtained by completely independent optical and meteorological techniques, and (2) the laser measurements represent a line integral, while the C_n values are based upon meteorological measurements at a single point.

Using Eq. (9), values of σ_t were calculated for each value of σ_m measured by the mobile receiver at the various ranges (460, 1180, 1900, 2700, and 3500 m), and plotted versus σ_m (mobile) in Figure 13. The data clearly show not only that there is a saturation of scintillation

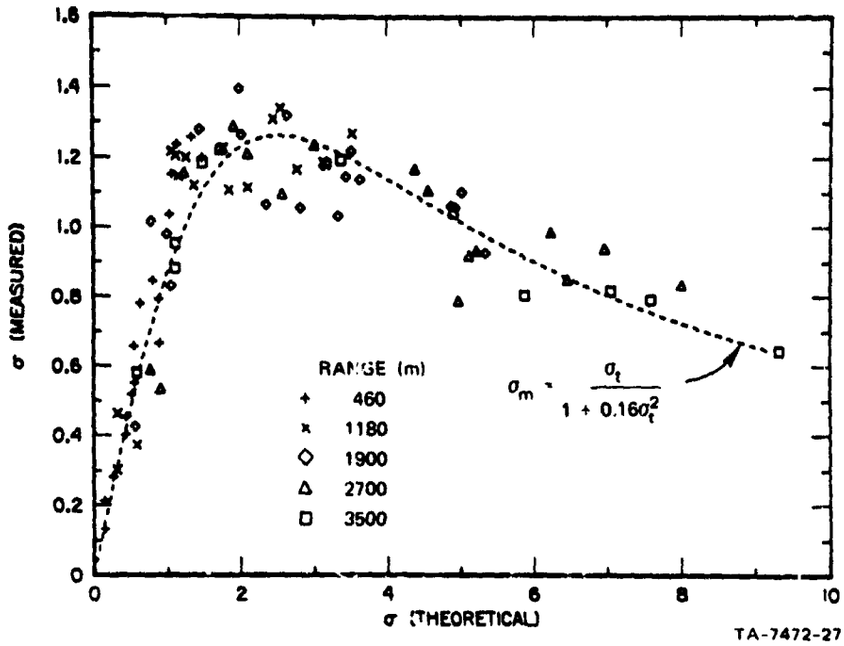

FIGURE 13 COMPARISON OF MEASURED VALUES OF LOG INTENSITY STANDARD DEVIATION AT THE MOBILE RECEIVER WITH VALUES PREDICTED BY TATARSKI'S THEORY, SHOWING THE SUPERSATURATION EFFECT

at about $\sigma_t = 2$, but also that there is a "supersaturation" region beyond, in which σ_m <u>decreases</u> with increasing σ_t. The dashed curve in the figure represents the best least-squares fit obtained with the model

$$\sigma_m = \frac{\sigma_t}{1 + a\sigma_t^2} \tag{10}$$

The equation for the fitted curve comes out to be

$$\sigma_m = \frac{\sigma_t}{1 + 0.16\,\sigma_t^2} \quad . \tag{11}$$

This function has a maximum scintillation magnitude of $\sigma_m^* = 1.27$ at $\sigma_t = 2.55$. In the limit for small σ_t, $\sigma_m = (\sigma_t)_{small}$ and the scintillation is represented by the Tatarski expression. In the limit for large σ_t, we have

$$\sigma_m = 6.49/(\sigma_t)_{large} \quad . \tag{12}$$

Figure 14 shows the result when the curve fitted to our measurements (Eq. 11) is compared with the observations by Gracheva (1967). The function is higher than the Russian measurements in the vicinity of the peak scintillation values, and slightly lower for large σ_t. The reason

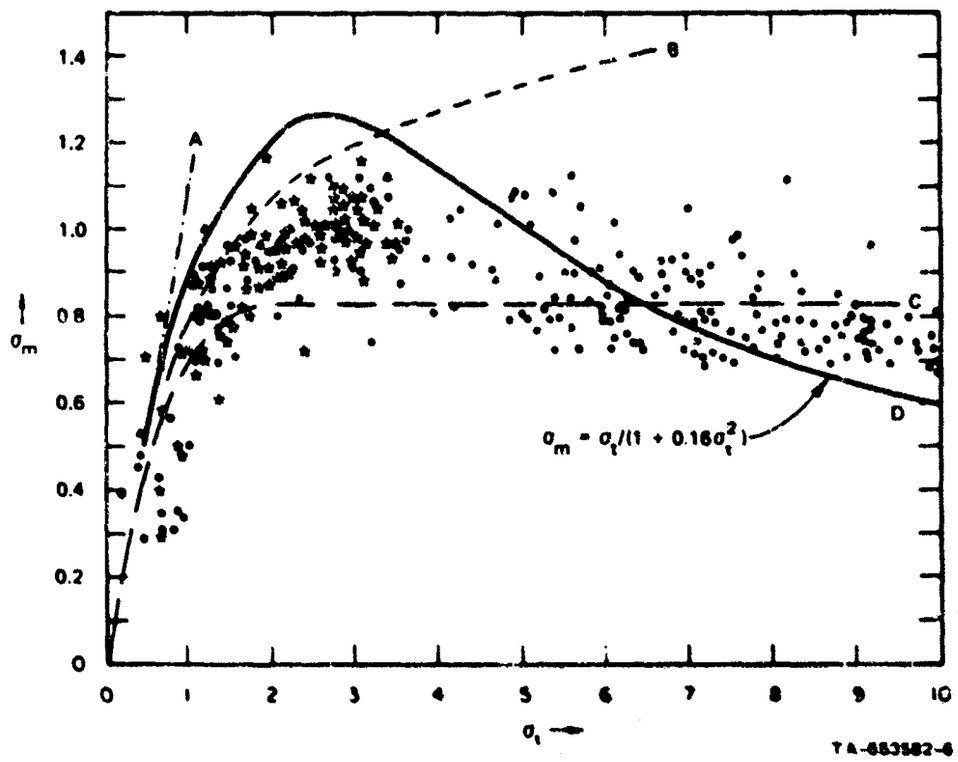

FIGURE 14 MEASURED (σ_m) VERSUS THEORETICAL (σ_t) VALUES OF LOG INTENSITY STANDARD DEVIATION, AS MEASURED BY GRACHEVA (1967) AND CORRECTED BY De WOLF (1968). The curves represent various theoretical formulations by (A) Tatarski (1961), (B) Tatarski (1966), and (C) De Wolf (1968), plus the empirical function fitted to the SRI data (D).

for this disparity is unknown, but it is possible that the Russian equipment lacked sufficient dynamic range to measure large σ_m, since they did not use log amplifiers. The Russian experiment also employed a mercury vapor lamp rather than a laser.

In addition to the Russian results (which, incidentally, the experimenter did not recognize as showing supersaturation), other recent experimental work by Deitz and Wright (1969), Meyers et al. (1969), and Ochs (1969) also show indications of the supersaturation effect.

The supersaturation effect perhaps can be visualized more clearly by referring to Figure 15, in which the measured values of σ_m are grouped according to various class intervals of C_n and plotted as a function of range. The scatter of the data points in these groups is primarily due to the widths of the class intervals used for C_n. It may be noted that the value of maximum scintillation σ_m^* is approximately equal to 1.27 and does not depend upon C_n. However, the range at which the peak scintillation occurs is a function of C_n; for larger C_n the range to the peak decreases. A surprising result is that at a given range, say 3 km, the scintillation will generally be greater for small C_n than for large C_n; it will reach the maximum value at some intermediate value of C_n.

It should be noted that the dashed curves in the four graphs in Figure 15 represent the same analytical function derived from all the data, rather than individual fits to the classed data.

The results shown in Figures 13 and 15 are quite significant in the eye-safety context. The maximum eye-damage probability is obtained at the peak value of $\sigma_m^* = 1.27$, and at long ranges the eye-damage probability goes down, rather than increasing approximately linearly with range, as Tatarski's equation predicts. The new results are incorporated into the procedure for estimating eye-damage probability, which is discussed in Section V.

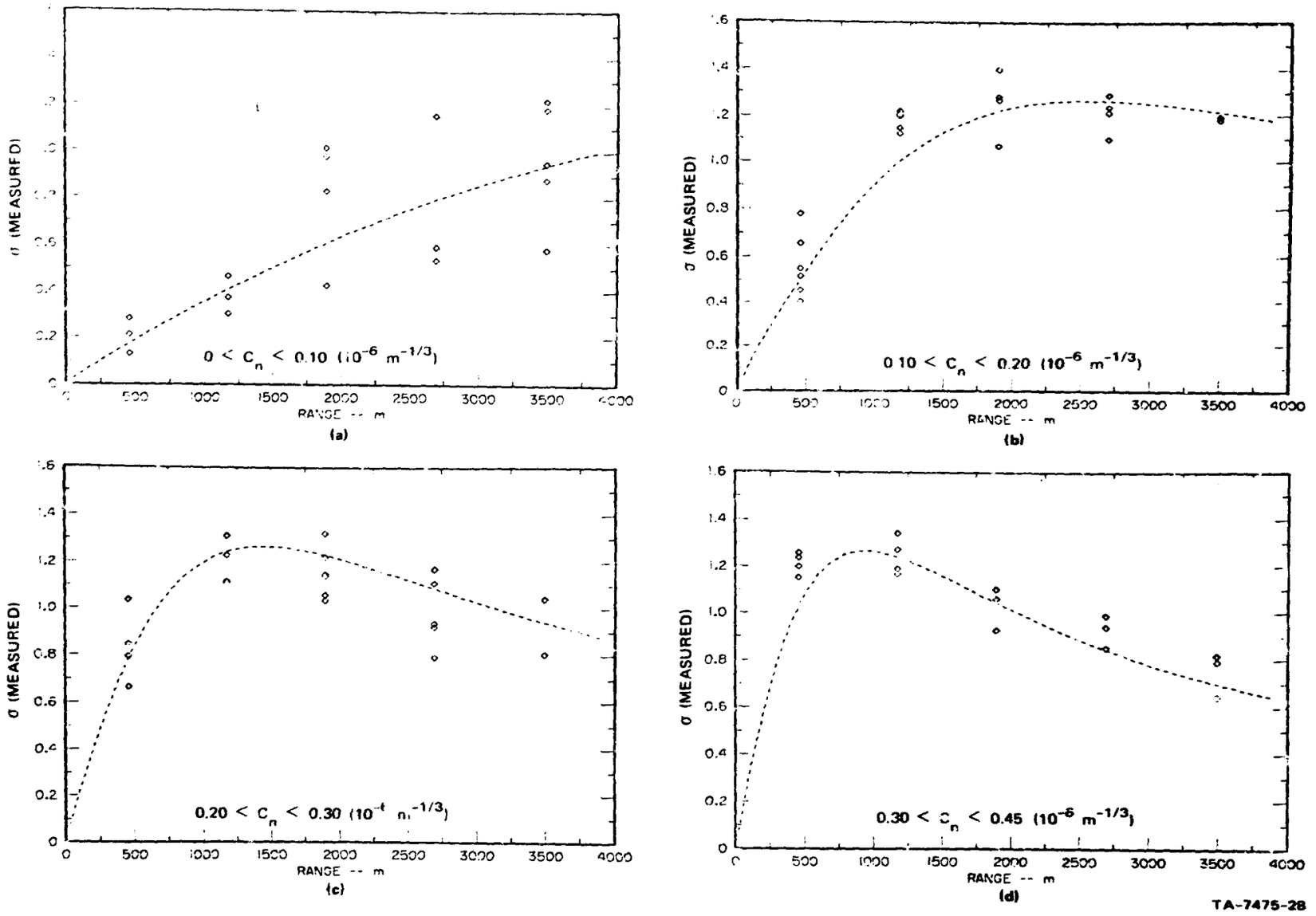

FIGURE 15 MEASURED LOG INTENSITY STANDARD DEVIATION AT THE MOBILE RECEIVER AS A FUNCTION OF RANGE, FOR VARIOUS CLASS INTERVALS OF C_n. The dashed curve in each graph represents the empirical function $\sigma_m = \sigma_t/(1 + 0.16\,\sigma_t^2)$.

2. Log-Normality of Probability Distributions

For the eye-damage estimates we assume that the intensity fluctuations follow a log-normal probability distribution, based upon the results of our first year's work. In general, the validity of this assumption is confirmed by the new results. To illustrate this, a reasonably representative run has been selected and is depicted in Figures 16-18. The probability distributions for the individual one-minute segments of the five-minute run are graphed in Figure 16 for the control and mobile receivers. The composite five-minute probability distributions for the two receivers are compared with Gaussian distributions with the same standard deviations in Figure 17, and are compared with each other in Figure 18.

As indicated in Figure 17, the actual probability distributions of the log intensity for the two receivers are fair approximations of the Gaussian curve. This is the case even though supersaturation is clearly occurring in the signal at the mobile receiver at 3500 m, as shown in Figure 18 by the smaller standard deviation for this distribution. It may be noted in Figure 17 that the distribution for the mobile receiver has a slight negative skew. This was found to be typical for detectors that were well centered in the laser beam. (Our laser had a Gaussian-shaped beam intensity profile.) When the detector was off-center by a moderate amount with respect to the beam, the probability distribution becomes positively skewed, as illustrated by the example in Figure 19. Here the beam was apparently slowly drifting, such that the originally well centered detector ended up near the edge of the beam at the end of the five-minute run. The one-minute probability distributions start out fairly symmetrical and Gaussian, but become increasingly positively skewed, probably due to the proximity of the lower bound of zero intensity. Apparently a true log-normal distribution occurs only when

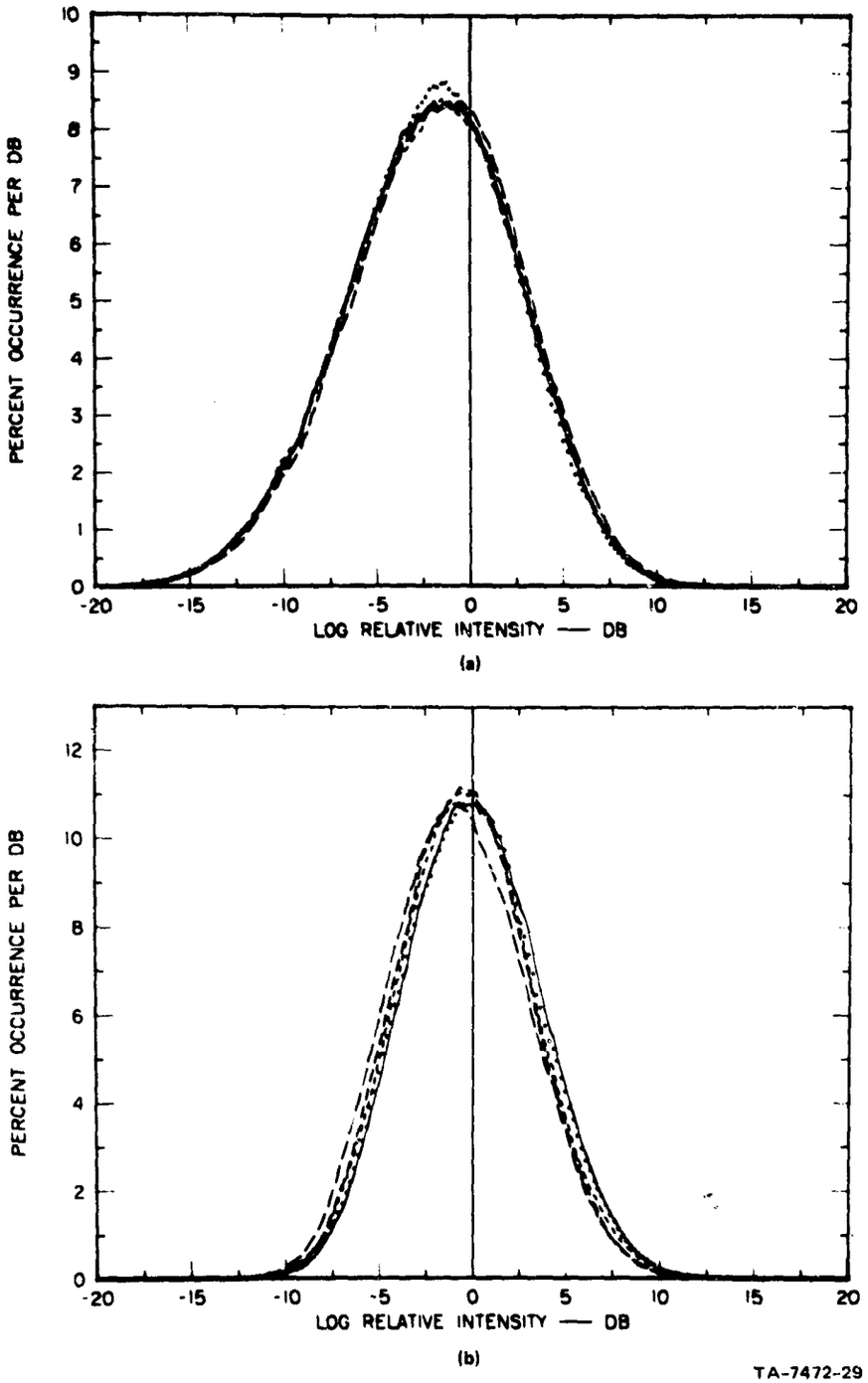

FIGURE 16 ONE-MINUTE PROBABILITY DISTRIBUTIONS FOR (a) CONTROL RECEIVER, AND (b) MOBILE RECEIVER AT 3500 m RANGE, FOR RUN 51.

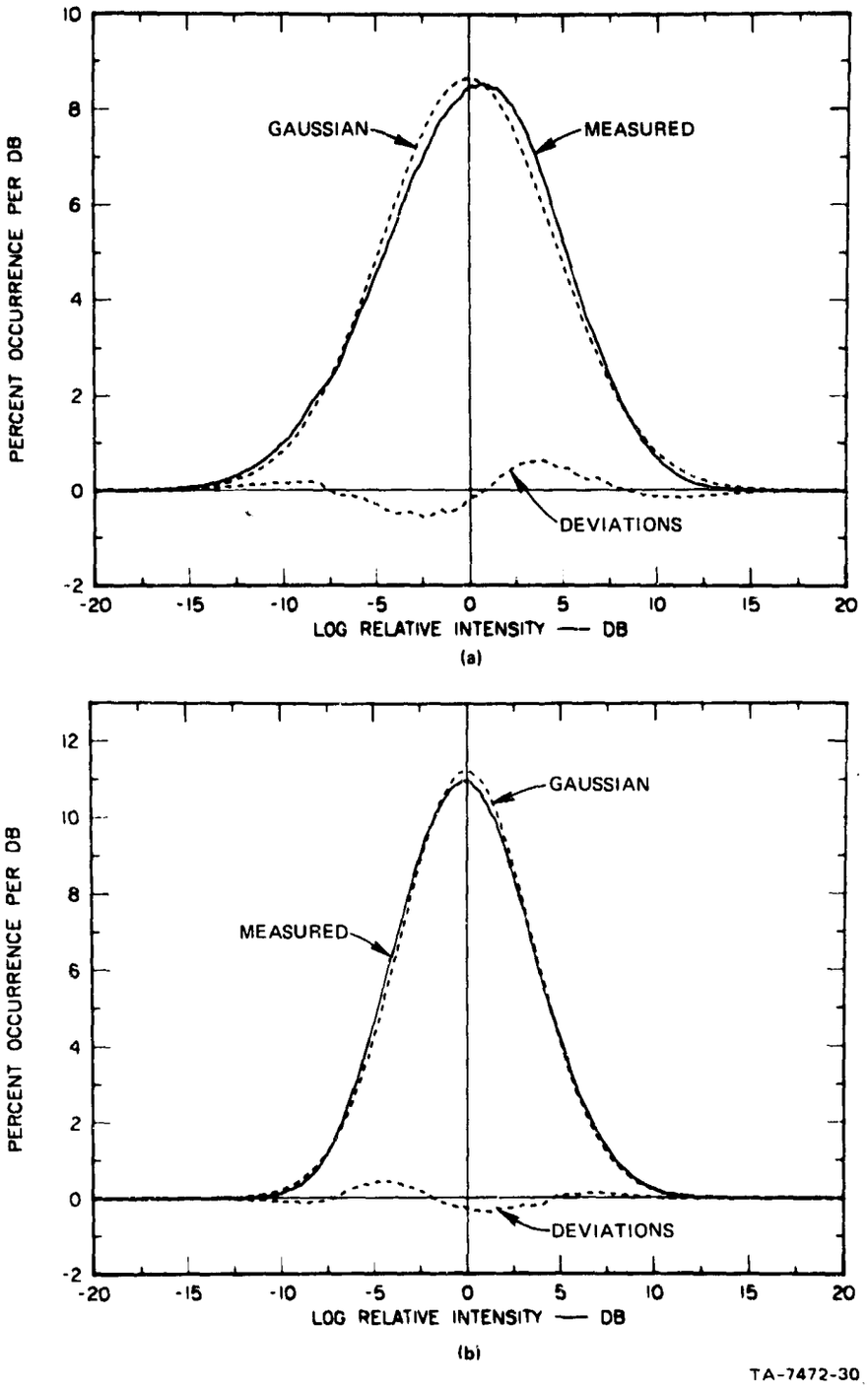

FIGURE 17 COMPOSITE FIVE-MINUTE PROBABILITY DISTRIBUTION AND GAUSSIAN FIT FOR (a) CONTROL RECEIVER, AND (b) MOBILE RECEIVER AT 3500 m RANGE, FOR RUN 51

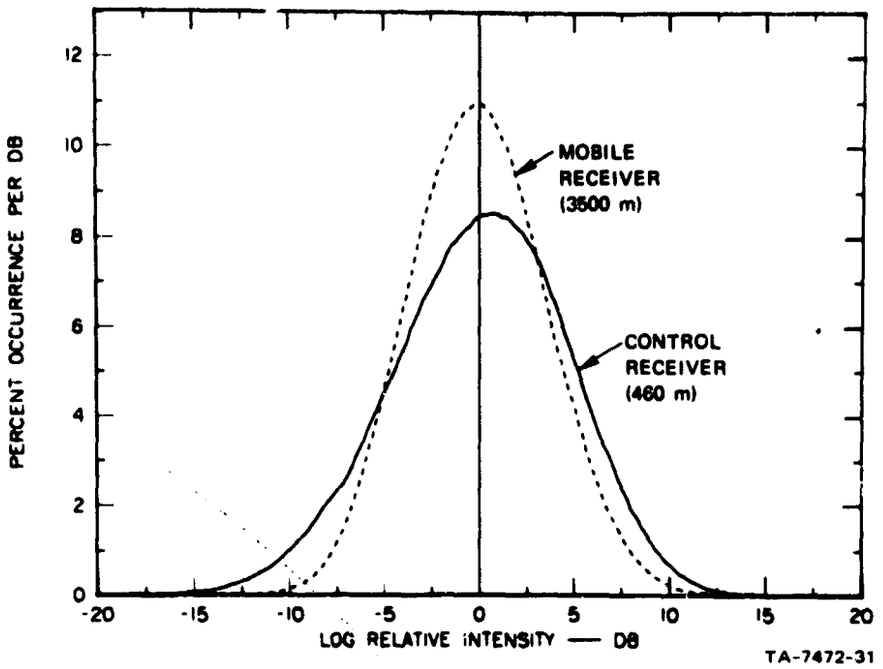

FIGURE 18 COMPARISON OF COMPOSITE PROBABILITY DISTRIBUTIONS FOR CONTROL AND MOBILE RECEIVERS FOR RUN 51.

the detector is located slightly off-center with respect to the beam axis.

The standard deviation of the distributions shown in Figure 19 might be expected to increase as the detector moves off-center. As shown in Table III, there is some indication that this may occur, but the increase in scintillation is apparently sufficiently small that this effect can be safely ignored in our analysis.

Figure 20 illustrates the characteristic non-Gaussian, lepto-kurtic nature of the probability distributions for ΔT. This is caused by the fact that the ΔT signal is typically quite intermittent, with periods of very small fluctuations interspersed with intervals of relatively large fluctuations. It turns out that, as shown in the example in Figure 21, the observed characteristic ΔT distribution is fitted

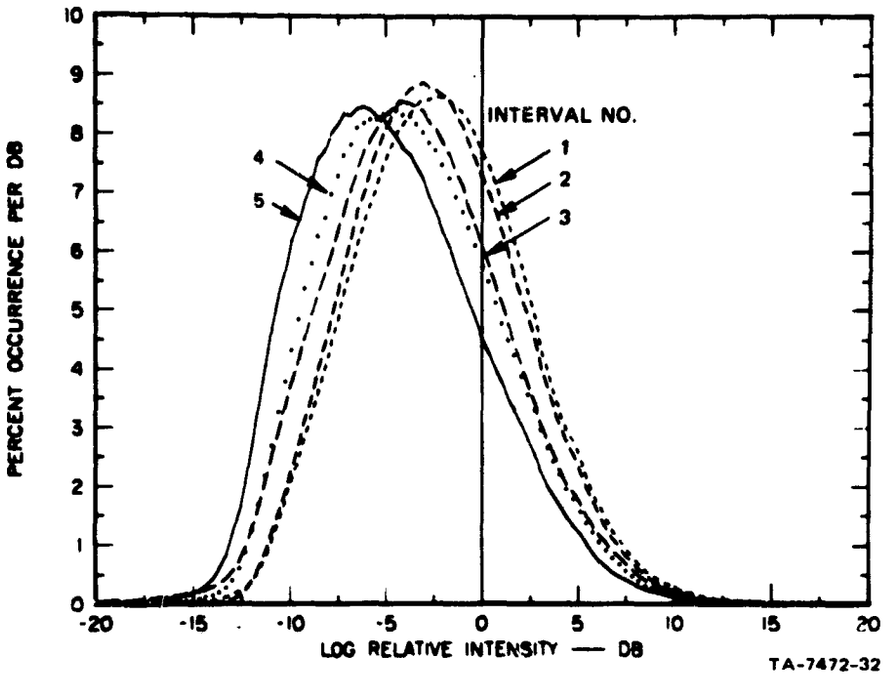

FIGURE 19 EXAMPLE OF CHANGE IN SHAPE OF PROBABILITY DISTRIBUTIONS AS BEAM DRIFT CAUSES DETECTOR LOCATION TO CHANGE TO EDGE OF BEAM (RUN 12, MOBILE RECEIVER, RANGE 2700 m).

Table III

MEANS AND STANDARD DEVIATIONS
FOR RUN 12 (MOBILE RECEIVER)

Interval No.	Mean Signal Level (dB)	Standard Deviation (dB)
1	-2.07	4.36
2	-2.37	4.28
3	-3.44	4.66
4	-3.62	4.45
5	-4.68	4.57

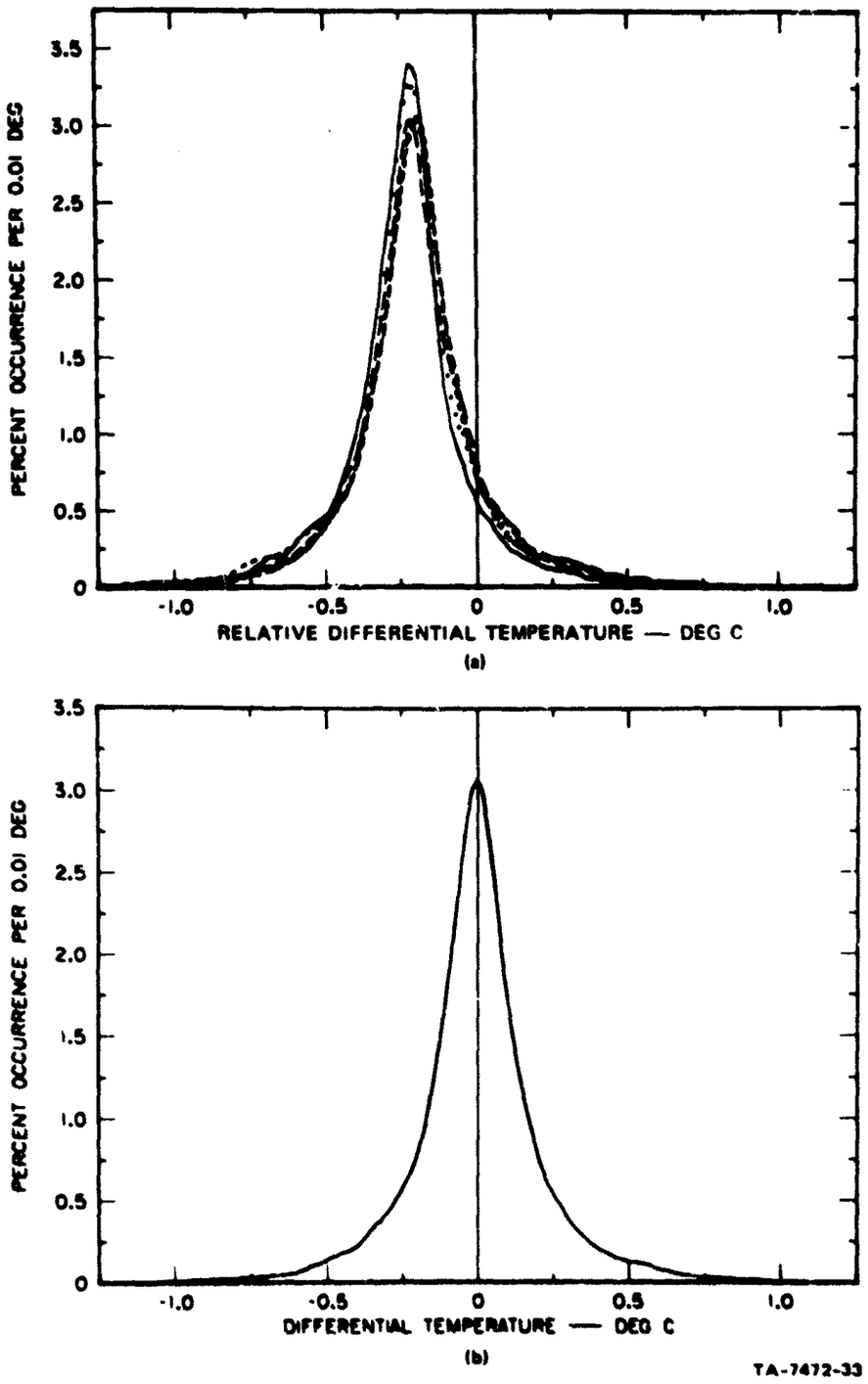

FIGURE 20 (a) ONE-MINUTE AND (b) COMPOSITE FIVE-MINUTE PROBABILITY DISTRIBUTIONS FOR ΔT FOR RUN 51

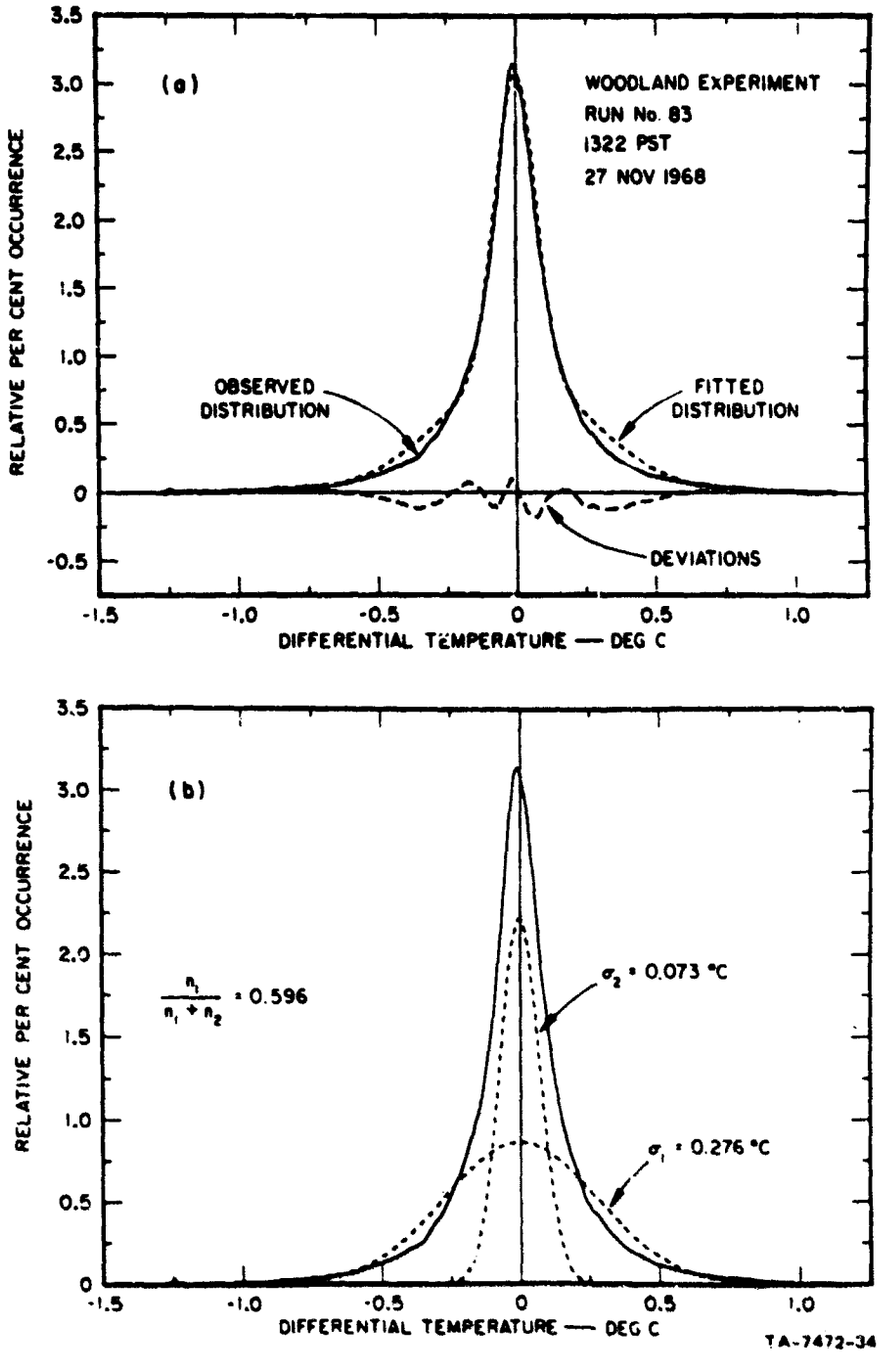

FIGURE 21 EXAMPLE OF FIT OF COMPOUND NORMAL DISTRIBUTION TO OBSERVED ΔT PROBABILITY DISTRIBUTION. (a) Fitted compound normal distribution; (b) Components of fitted compound normal distributions. The parameters n_1 and n_2 represent the total number of occurrences in each of the component distributions

reasonably well by the sum of two normal distributions with different standard deviations.

3. Spectra of Scintillation

The partition of laser signal fluctuation energy in terms of frequency was examined for several sets of runs by processing the analog data through a bank of third-octave filters. This procedure yielded values representing relative log intensity standard deviation for eight frequency bands from 8 to 1000 Hz. These approximate power spectra are presented in Figure 22 for two sets of runs obtained during reasonably stationary meteorological conditions. Figure 22(a) represents a light-wind case, when the cross-path wind component was only about 1 m/s. The spectra for the signal from the control receiver at 460 m are very consistent from run to run, for the first three runs of the series, with the peak energy at about 16 Hz. The signal spectrum for the fourth run (#83), although similar, probably shows the effect of an increase in cross-path wind component. However, the mobile receiver signal spectra show the effects of supersaturation as the receiver is moved downrange. With increasing range, the total fluctuation energy decreases, and the dominant fluctuations shift to higher frequencies, which was apparent from inspection of the signals while the data were being obtained. The spectra for the mobile receiver also become bimodal, with two peaks, one at about 16 Hz and the other at about 150-200 Hz.

Figure 22(b) shows the power spectra for a higher-wind situation, in which the cross-path component was about 4 m/s. The control receiver spectra all peak at about 125 Hz, but the spectra for the mobile receiver are quite similar to those for the light-wind case [Figure 22(a)]. This indicates that the wind speed has little effect upon fluctuation frequencies in the supersaturation region, although it is significant in

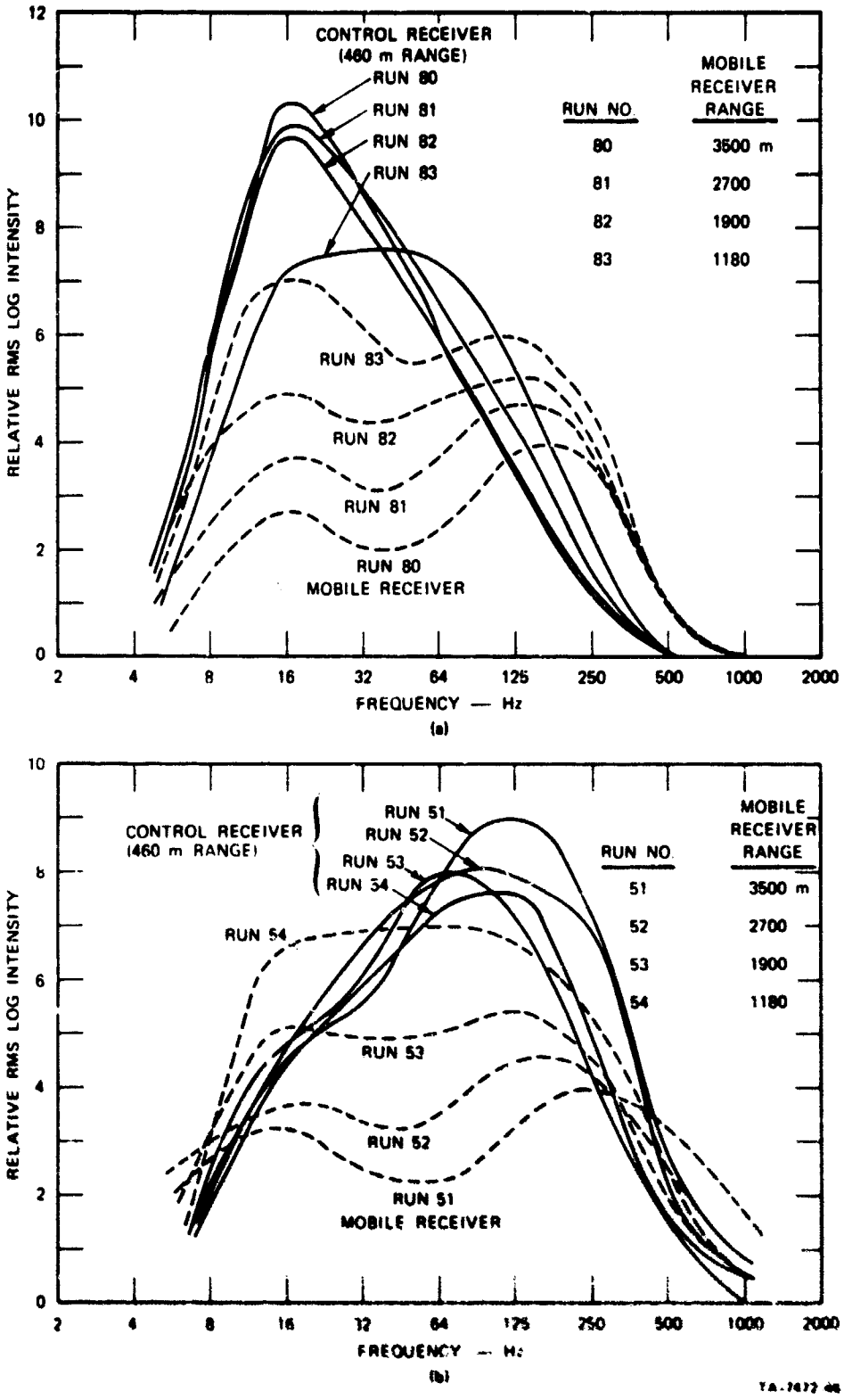

FIGURE 22 APPROXIMATE ANALOG POWER SPECTRA FOR CROSS-PATH WIND COMPONENT OF (a) 1 m/sec AND (b) 4 m/sec

the subsaturation region, as Tatarski (1961) predicted and Ryznar (1965) experimentally confirmed. The reason for the double peak in the spectra for the signals in the supersaturation region is unknown, but the lower frequency peak could be associated with beam wander. It is possible that these spectra may offer a clue into the mechanism for the supersaturation effect. This phenomenon is probably associated with multiple turbulent scattering, in which the high-and-low-intensity regions in the beam are eroded by the process of destructive interference. Deitz and Wright (1969) have offered some qualitative suggestions along this line.

4. Comparison of Standard Deviations Obtained by Digital and Analog Processing

The results of the digital data processing procedure for determining standard deviations were used exclusively in the Woodland data analysis for deriving the results just presented. However, it is worthwhile determining the degree of correlation between the standard deviations derived by the digital and analog methods. Comparisons of σ (digital) and σ (analog) are presented in Figure 23. The indicated linear least-squares fits give the following relationships:

$$[\sigma(\text{control})]_{dig} = 0.087 + 1.01\,[\sigma(\text{control})]_{anal} \tag{13}$$

$$[\sigma(\text{mobile})]_{dig} = 0.082 + 1.02\,[\sigma(\text{mobile})]_{anal} \tag{14}$$

$$[\sigma(\Delta T)]_{dig} = 0.06 + 1.37\,[\sigma(\Delta T)]_{anal} \quad . \tag{15}$$

Since the above relationships fit the data well, with relatively little scatter, they have proven useful in calibrating the Sigma Meter to correct the analog data from the control receiver and differential thermometer collected during the slant-path experiment.

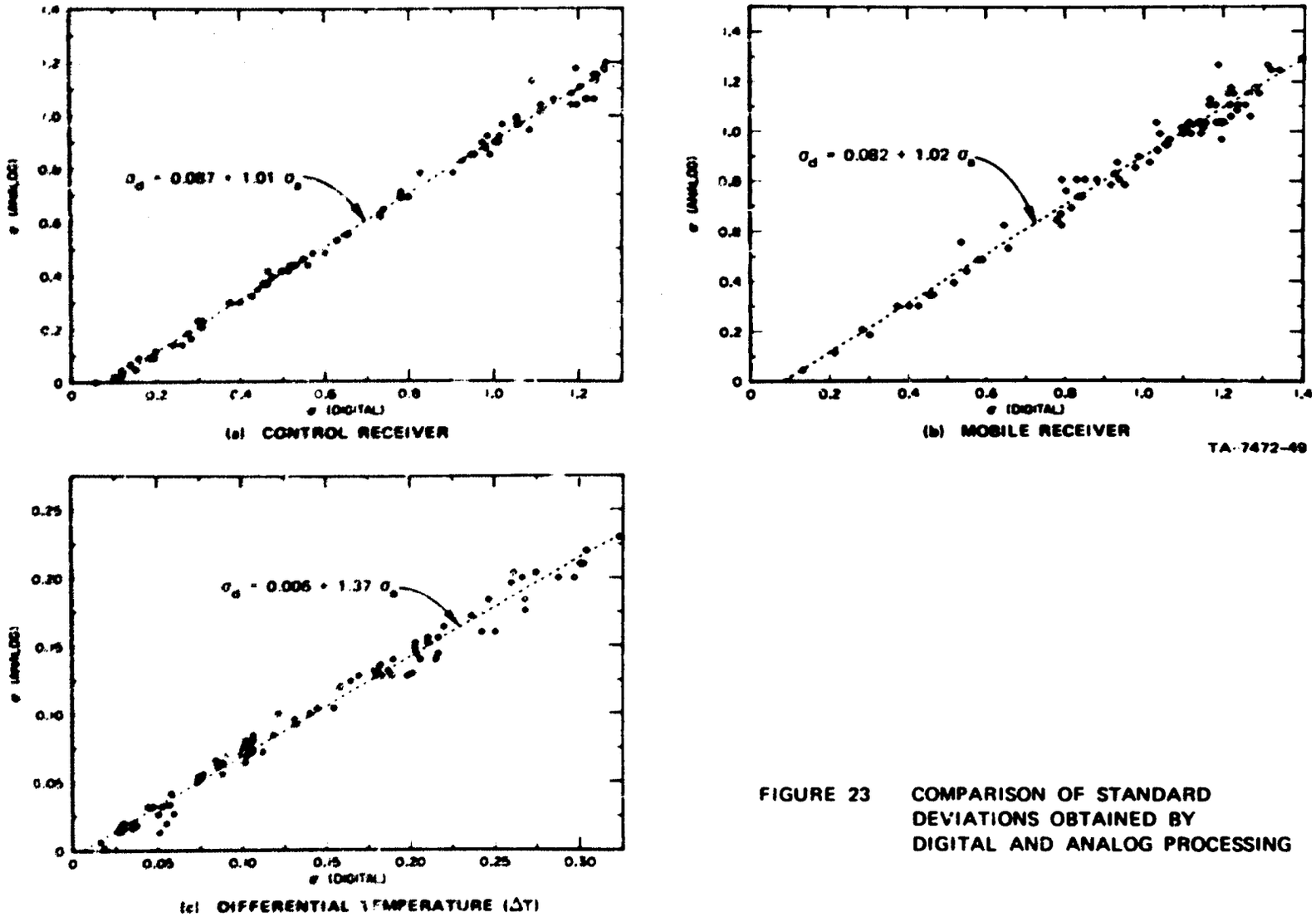

FIGURE 23 COMPARISON OF STANDARD DEVIATIONS OBTAINED BY DIGITAL AND ANALOG PROCESSING

IV EXPERIMENT B--SLANT-PATH PROPAGATION EXPERIMENT

A. General

The specific objectives of this experiment were as follows:

(1) To verify the existence of scintillation magnitude saturation for slant-path laser propagation, and to examine the magnitude of the scintillation maximum σ_m^* and its dependence upon path geometry.

(2) To develop relationships by means of concurrent measurements among slant-path scintillation, scintillation on a horizontal path near the ground, and atmospheric conditions.

(3) To determine the effect, if any, of the pseudo-wind due to aircraft motion upon scintillation magnitude.

To accomplish these aims, we fielded an experimental program at Brooks Air Force Base, Texas, during the period 14-23 April 1968. The main portion of the experiment involved tracking an airborne receiver mounted on an orbiting C-97 airplane with a ground-based laser.

B. Site Description

A plan view of the area surrounding the experimental site is presented in Figure 24. The average elevation is about 575 ft above sea level. The terrain is generally flat to slightly rolling in the area south and east of the ground site where the flights were conducted. The vegetation consists of patches of scrub brush and low trees intermixed with frequent open grassy fields and a few surbuban housing developments. The central business district of the city of San Antonio lies 7.5 miles to the northwest of the ground site.

FIGURE 24 EXPERIMENTAL SITE LOCATION ON BROOKS AFB. Three aircraft ground tracks used in the experiment are shown.

The immediate area around the ground site was level and covered with short grass. As shown in Figure 25, the recording van was situated

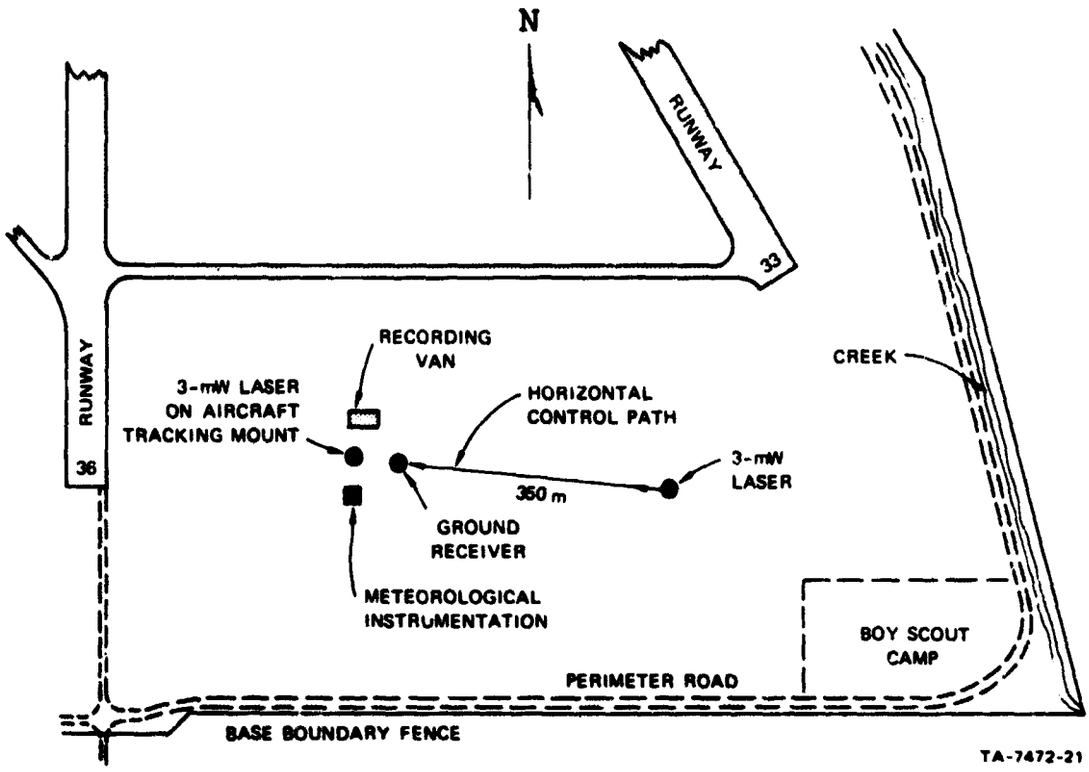

FIGURE 25 SITE LAYOUT FOR SLANT-PATH EXPERIMENT AT BROOKS AIR FORCE BASE

near the laser tracking mount, as was the meteorological instrumentation and the receiver for the ground laser.

C. Instrumentation

1. Laser Measurements

Two Spectra-Physics Model 122 3-mW helium/neon lasers were used in this experiment, one for the slant-path propagation link and the other for a 350-m horizontal control link. The instrumentation setup for the horizontal control path at about 1.7 m above the ground was

essentially identical to that used in the Woodland experiment, again with a 25-cm-diameter laser beam impinging upon a receiver with a 5-mm aperture. However, the slant-path portion of the experiment required the development of special instrumentation.

A surplus antiaircraft gun director mount was precisionized and fitted with an azimuth motor drive and optical sighting devices to permit its use in tracking the receiver on the orbiting aircraft with the laser (Figure 26). The same model laser was used here as was used in the horizontal control link. The tracking mount proved to be capable of consistently accurate tracking to within about plus or minus one-half plane-length (approximately ± 5 mrad) with an experienced operator when the airplane was in smooth, level, orbiting flight. In consideration of this tracking accuracy, the laser beam was diverged to approximately 10 mrad. The maximum azimuthal tracking rate of the mount was approximately 6°/s.

The left front side window of a USAF C-97 aircraft was removed and the laser receiver assembly installed in the opening, as shown in Figure 27. In order to reduce the background noise level in the receiver caused by reflected sunlight, it was necessary to minimize the receiver field of view. A value of 10 mrad was found to be suitable. This required that the receiver assembly (Figure 28) be mounted on a pivot with appropriate sighting devices, so that it could be manually aimed at the laser on the ground. A 50-mm corner-cube reflector was mounted on the front portion of the receiver assembly to provide a visual indication of tracking accuracy to the ground tracking mount operator. An audio monitor of the received signal level was used by the airborne receiver operator to aid in aiming the receiver. Figure 29 shows the airborne receiver and associated electronics installation in the aircraft, as well as the receiver assembly in its operating position.

FIGURE 26 LASER TRACKING MOUNT

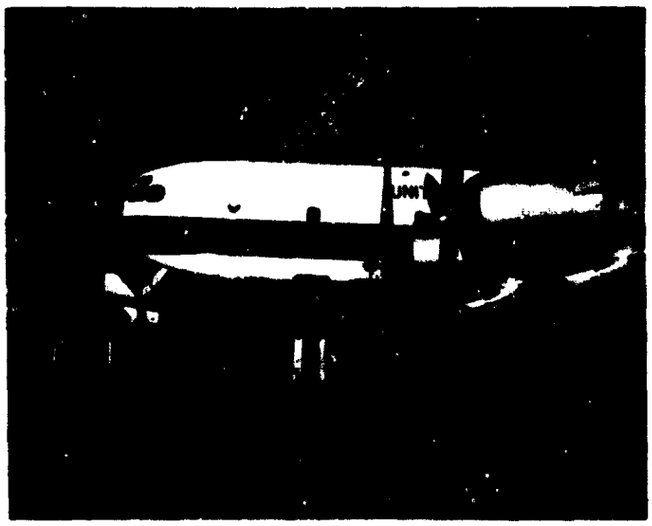

(a)

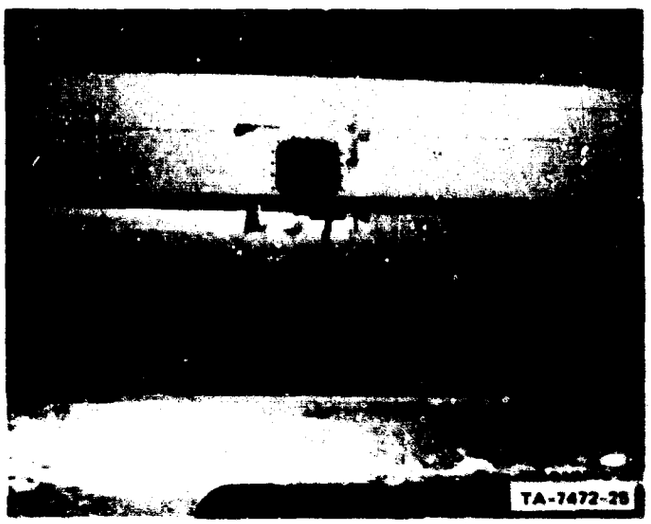

(b)

FIGURE 27 (a) BROAD VIEW, AND (b) CLOSE-UP VIEW OF LASER SIGNAL RECEIVER INSTALLATION IN WINDOW OPENING OF U.S. AIR FORCE C-97 AIRCRAFT.

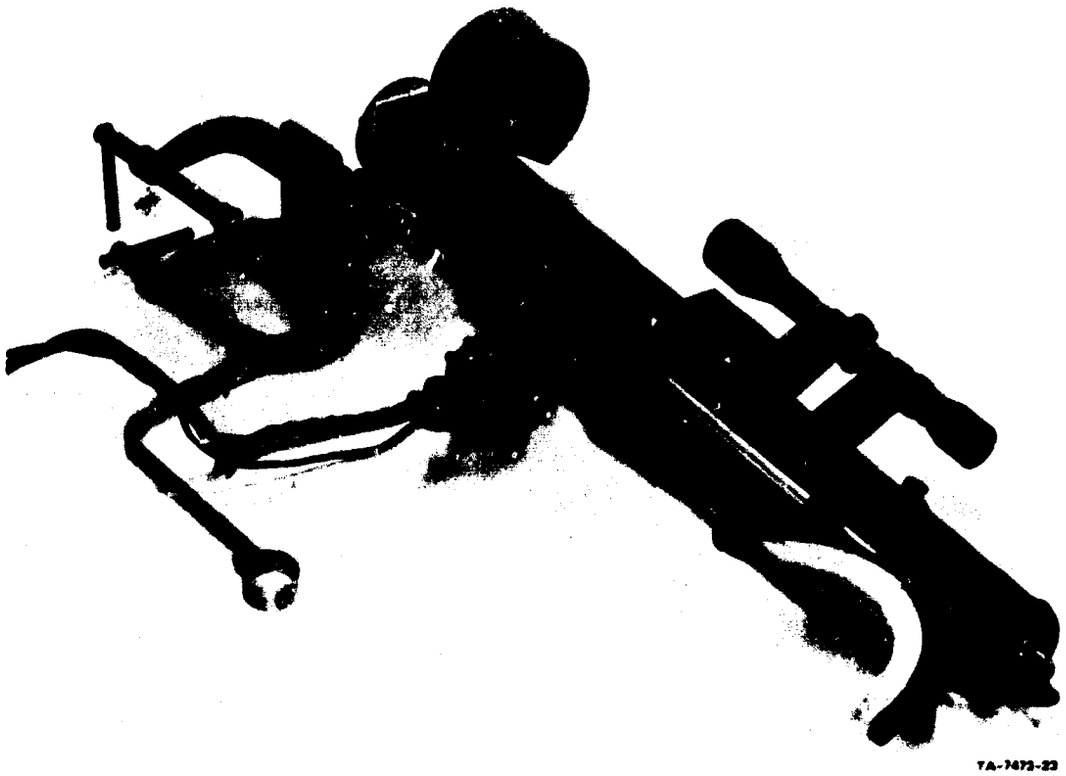

FIGURE 28 AIRBORNE RECEIVER AIMING ASSEMBLY

Provision was made for automatic sequencing of a test signal and the calibration levels at the beginning and end of each run, which was controlled by buttons in the hand grip on the receiver. The basic receiver electronics system was the same as that used in the Woodland experiment, with the signal from an RCA 7265 PMT (with 5-mm-aperture diameter) fed into a logarithmic amplifier. The output of the log amplifier was converted to FM mode and transmitted back to the recording van at the ground by means of a telemetry link, which proved to be very trouble-free. Communications between the ground station and the airplane were carried out using a UHF channel.

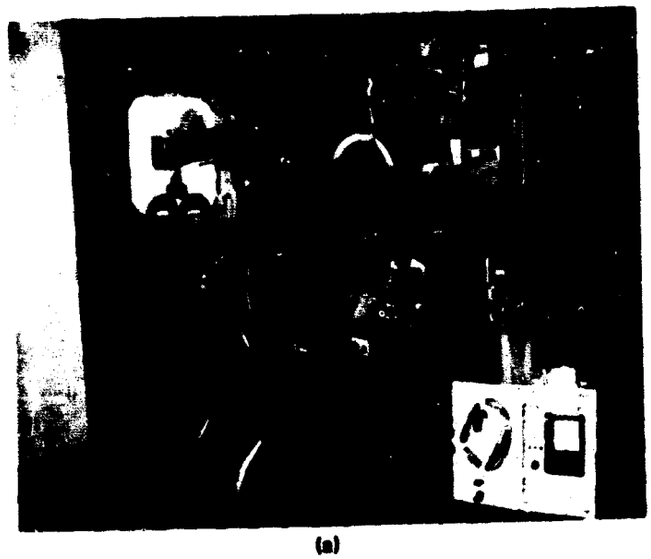

(a)

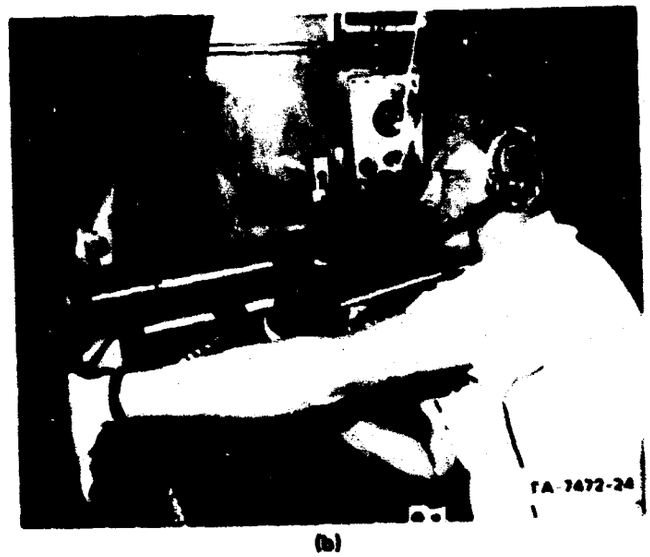

(b)

FIGURE 29 (a) AIRBORNE RECEIVER AND ELECTRONICS INSTALLATION INSIDE C-97 AIRCRAFT, AND (b) RECEIVER AIMING ASSEMBLY IN OPERATING POSITION

2. Meteorological Measurements

Ground instrumentation used in this experiment for monitoring the meteorological conditions consisted of an anemometer and wind vane for measuring mean wind velocity, and the differential thermometer previously described for measuring the temperature structure function. All instruments were positioned at the mean laser beam height, 1.7 m.

Mean temperature profiles up to 8000 ft MSL were obtained by means of a thermistor thermometer installed on the C-97 aircraft. The shielded sensor tube was exposed to the airstream by a mount on a 35-cm-long boom attached to the window clamp for the receiver assembly (Figure 28). Temperature profiles were recorded during spiral ascents and descents at the start and end of each flight by means of a chart recorder [shown at right bottom of Figure 29(a)].

D. Experimental Procedures

The basic configuration for the slant-path experiment is illustrated in Figure 30. The experimental procedure consisted of conducting a series of runs during which the airborne receiver was tracked with the laser as the C-97 flew an almost continuous circular path in a counterclockwise direction around the ground station. The tracking occurred over an approximate 180° arc from southwest to northeast of the ground station. Several aircraft altitudes between 1500 and 8000 ft above ground were employed, at various ground distances between 0.5 and 2.5 miles from the laser. The runs varied between 2 and 7 minutes in duration.

The telemetered signal from each run was recorded in FM mode on a 30 in/s analog magnetic tape recorder with a 10 kHz frequency bandwidth.

The signal from the receiver on the horizontal control path and the ΔT signal were recorded continuously in FM mode on a separate 7-1/2 in/s magnetic tape recorder. In addition, the signals were also fed into

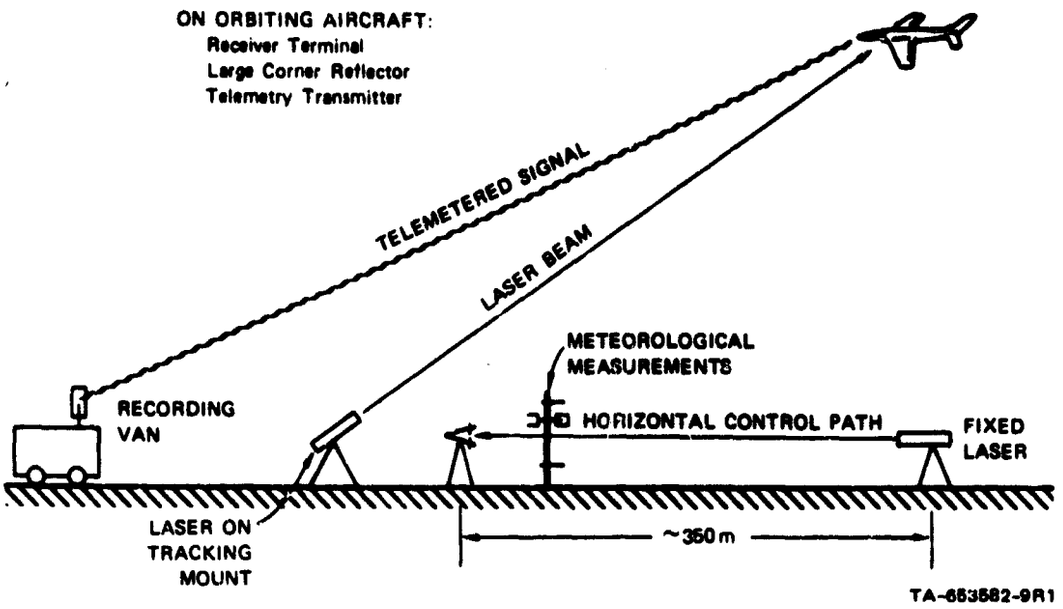

FIGURE 30 EXPERIMENTAL CONFIGURATION FOR SLANT-PATH MEASUREMENTS

the two channels of the Sigma Meter, whose output was displayed on a chart recorder. This provided a real-time indicator of turbulence conditions.

A chronological summary of activities during the slant-path experiment is presented in Table IV. Five days were required for the equipment installation and testing, followed by two days of data collection. The quantity of data collected during the field program was limited by the restricted availability of the C-97 aircraft.

E. Data Analysis

A fairly substantial number of runs were completed on the two days of 19-20 April 1969, as summarized in Table V. The slant-path signal data for each run were digitized at a rate of approximately 15,000 samples/s and converted into amplitude probability distributions (histograms) essentially as was done with the Woodland data. However, only one histogram per run was computed for the slant-path data.

Table IV

CHRONOLOGICAL SUMMARY, SLANT-PATH EXPERIMENT

Day	Activity
14 April	Unpacked equipment; began ground installation
15 April	Completed ground installation
16 April	Completed C-97 aircraft installation
17 April	Test flight, operator tracking practice
18 April	Test flight, 6 preliminary data runs collected
19 April	Data flight, 4 hours, 24 runs recorded
20 April	Data flight, 2-1/2 hours, [illegible] runs recorded
21 April	Aircraft in maintenance
22 April	Aircraft in maintenance
23 April	Data taken on ground link; aircraft grounded because of mechanical problems and unavailable remainder of week because of other commitments

The principal problem in the analysis of these data resulted from the intermittent nature of the signal as the tracking was on and off target. When the tracking was off target, the signal consisted only of background noise. This can be seen in Figure 31, which shows examples of 15-s time-exposure photographs of the CRO display for selected runs. At the longer ranges, the signal-to-noise ratio (SNR) was frequently low and the laser signal envelope merged with the background noise envelope. These two distributions are superimposed upon one another, as indicated in the sample histograms shown in Figure 32. In the first example in this figure the signal and noise distributions are rather clearly separated, but there were many runs similar to the second example where the two distributions were merged together more closely.

Table V

LASER DATA SUMMARY, SLANT-PATH EXPERIMENT

Run No.	Date	Start Time (CST)	Aircraft Altitude (ft above ground)	Ground Distance (miles)	Slant Range (m)	Tape Numbers Slant	Tape Numbers Horizontal	Weather, Remarks
1	4/19/69	1018:00	5000	1.6	3000	4	3	○ 25 150°/9 mph 78° F
2		1026:45	5000	1.6	3000	4	3	Same
3		1036:45	5000	1.6	3000	4	3	Same
4		1047:43	6000	1.6	3150	4	3	Same
5		1057:45	6000	1.6	3150	5	3	Same
6		1107:10	6000	1.6	3150	5	3	○ 25 160/10 79°
7		1120:15	3000	1.0	1850	5	3	Same
8		1129:00	3000	1.0	1850	5	3	Same
9		1136:40	3000	1.0	1850	5	3	○ 15 135/12
10		1147:00	1500	0.5	950	5	4	Ground oper. couldn't track
11		1155:15	3000	1.0	1850	6	4	○ 15 140/10
12		1206:15	6000	1.6	3150	6	4	Same
13		1331:00	6000	1.0	2450	6	4	○ 25 150/13+17
14		1342:30	6000	1.6	3150	6	4	Same
15		1352:00	4000	1.3	2400	7	4	Abort--tape ran out
16		1406:05	4000	1.3	2400	7	4	Abort
17		1410:00	4000	1.3	2400	7	4	○ 25 150/12+15
18		1418:15	3000	1.0	1850	7	4	Same
19		1424:00	3000	1.0	1850	7	4	Same
20		1432:00	4000	1.3	2400	7	5	Same
21		1440:00	4000	1.3	2400	7	5	Same--few cu
22		1449:45	6000	1.6	3150	7	5	○ 25 150/14+17 81°
23		1458:00	6000	1.6	3150	8	5	No turb. abv. 7000 ft
24		1512:20	8000	2.0	4050	8	5	○ 25 150/12
25	4/20/69	1018:15	8000	2.0	4050	8	5	A90 ◐/⊕ 15 090/7 86°
26		1027:00	8000	2.0	4050	8	5	Same
27		1044:20	3000	1.0	1850	8	5	Same
28		1108:00	3000	1.0	1850	9	6	Same
29		1119:10	3000	1.5	2600	9	6	80 ◐/◐ 15 070/7
30		1129:20	3000	2.0	3350	9	6	Same 73°
31		1143:30	3000	2.5	4150	9	6	Same
32		1156:40	3000	1.0	1850	9	6	50 ◐ 25 120/8
33		1210:45	3000	1.5	2600	10	6	Same
34		1219:30	3000	0.8	1600	10	6	50 ◐ 5 120/8
35		1344:00	3000	1.0	1850	10	6	50 ◐/◐ 25 160/10+14 74°
36		1352:00	3000	1.0	1850	10	6	30 ◐ /60 ◐ 25 170/8
37		1403:30	3000	1.5	2600	10	6	Same
38		1412:00	3000	2.0	3350	10	7	Same
39		1418:10	3000	2.5	4150	11	7	A40 ◐ 25 160/6 75° (Mounting strap broke on airborne receiver)

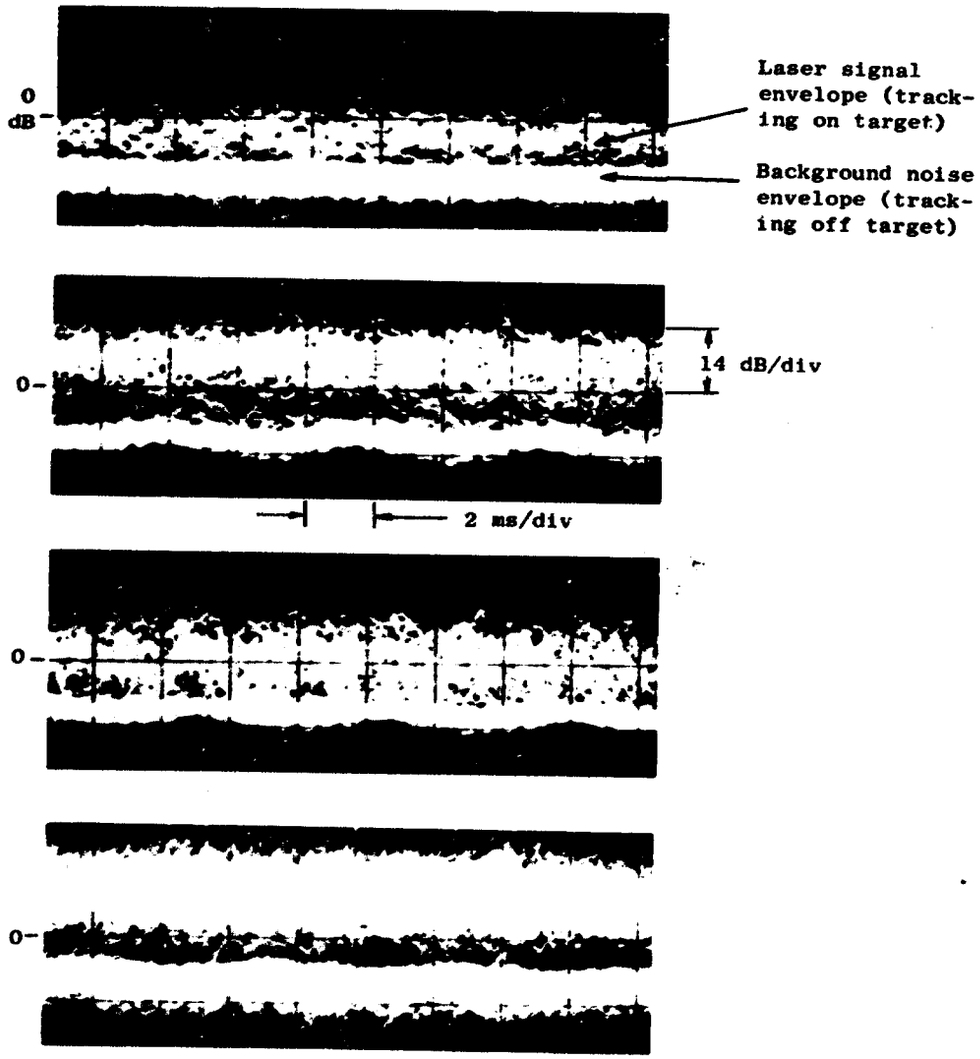

Run No.	Start Time (CST)	Elev Angle	Slant Range (m)
26	1031	37°	4050
27	1044	30°	1850
29	1119	21°	2600
34	1219	35°	1600

TA-7472-35

FIGURE 31 EXAMPLES OF SLANT-PATH LASER DATA FROM 20 APRIL 1969 IN THE FORM OF 15-SECOND OSCILLOSCOPE TIME EXPOSURES OF SIGNAL OUTPUT FROM LOG AMPLIFIER

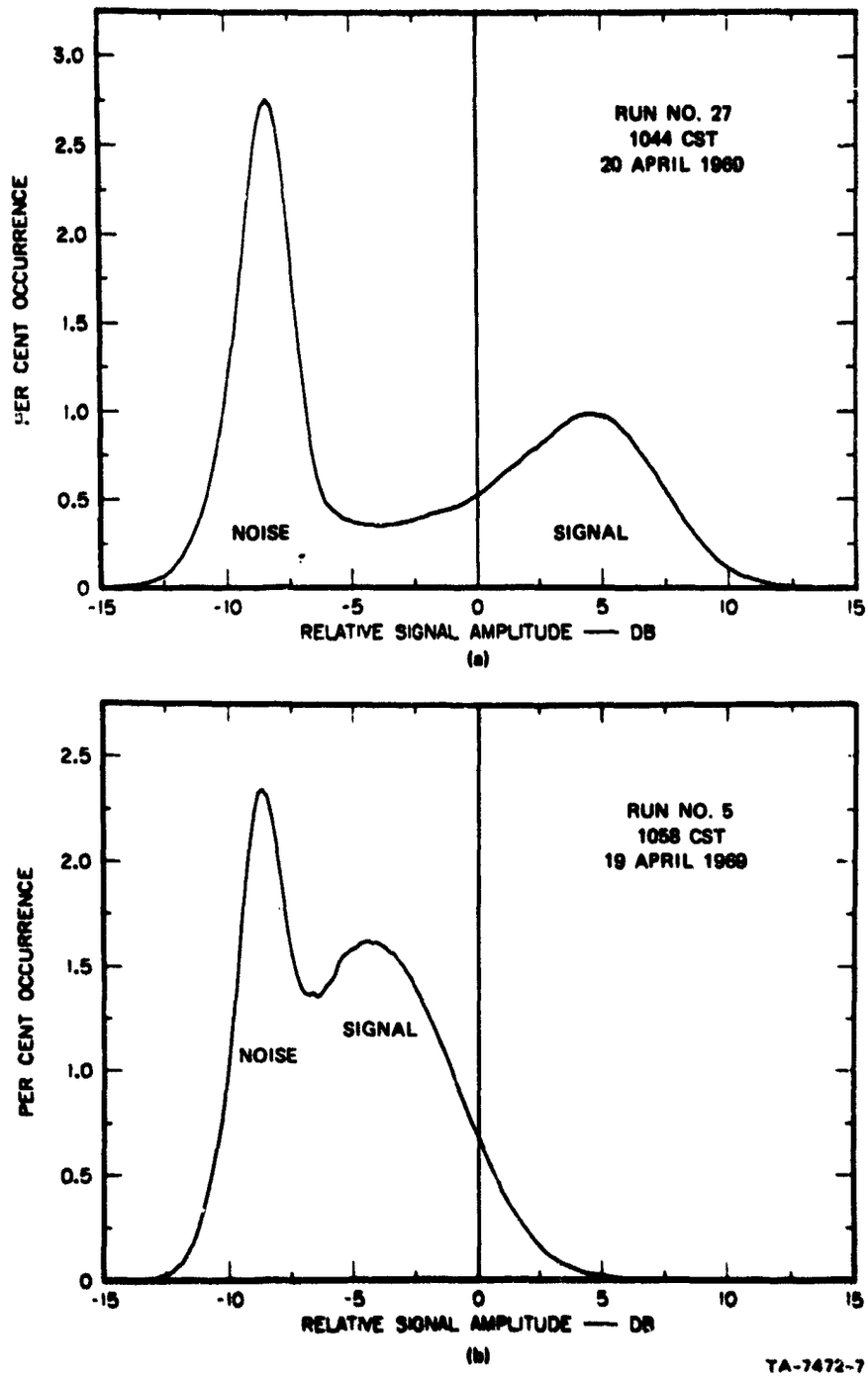

FIGURE 32 SAMPLE HISTOGRAMS FOR SLANT-PATH EXPERIMENT SHOWING (a) GOOD SIGNAL-TO-NOISE RATIO (SNR), AND (b) POOR SNR

The analysis technique used to find the standard deviation of the signal distribution was simply to locate the mode (peak value) of this distribution on the histogram--if there was a distinguishable mode--and then to use the high-amplitude half of the distribution to graphically compute the standard deviation, assuming that the distribution is Gaussian. It is recognized that this procedure will give only approximate results. More accurate values should be obtained when a new technique currently under development is completed. This new procedure involves the use of a nonlinear least-squares computer program to fit a model distribution to the entire observed histogram. One of the model parameters obtained from this fitting routine is the standard deviation of the signal distribution. The model attempts to take into account and remove the influence of the "artificial" signal intensity fluctuation that occurs when the beam--which has a Gaussian intensity profile--is scanned across the receiver in the course of normal tracking.

The chart records of the standard deviations produced by the Sigma Meter for the horizontal-path laser signal and the differential thermometer were digitized at 15-s intervals by means of a Benson-Lehner LARR-M digitizer. The resulting data were written on magnetic tape to facilitate later use.

F. Results

1. Meteorological and Horizontal Control Path Measurements

Ground-based measurements were obtained on three days during this experiment; the slant-path measurements were limited to two days because of the problem with aircraft availability. The results of the ground-based measurements are illustrated in Figures 33-37. Figure 33 presents scatter diagrams for the three experimental days for the measured values of scintillation (σ_m) on the 350-m horizontal control range versus C_n as obtained from the differential thermometer measurements.

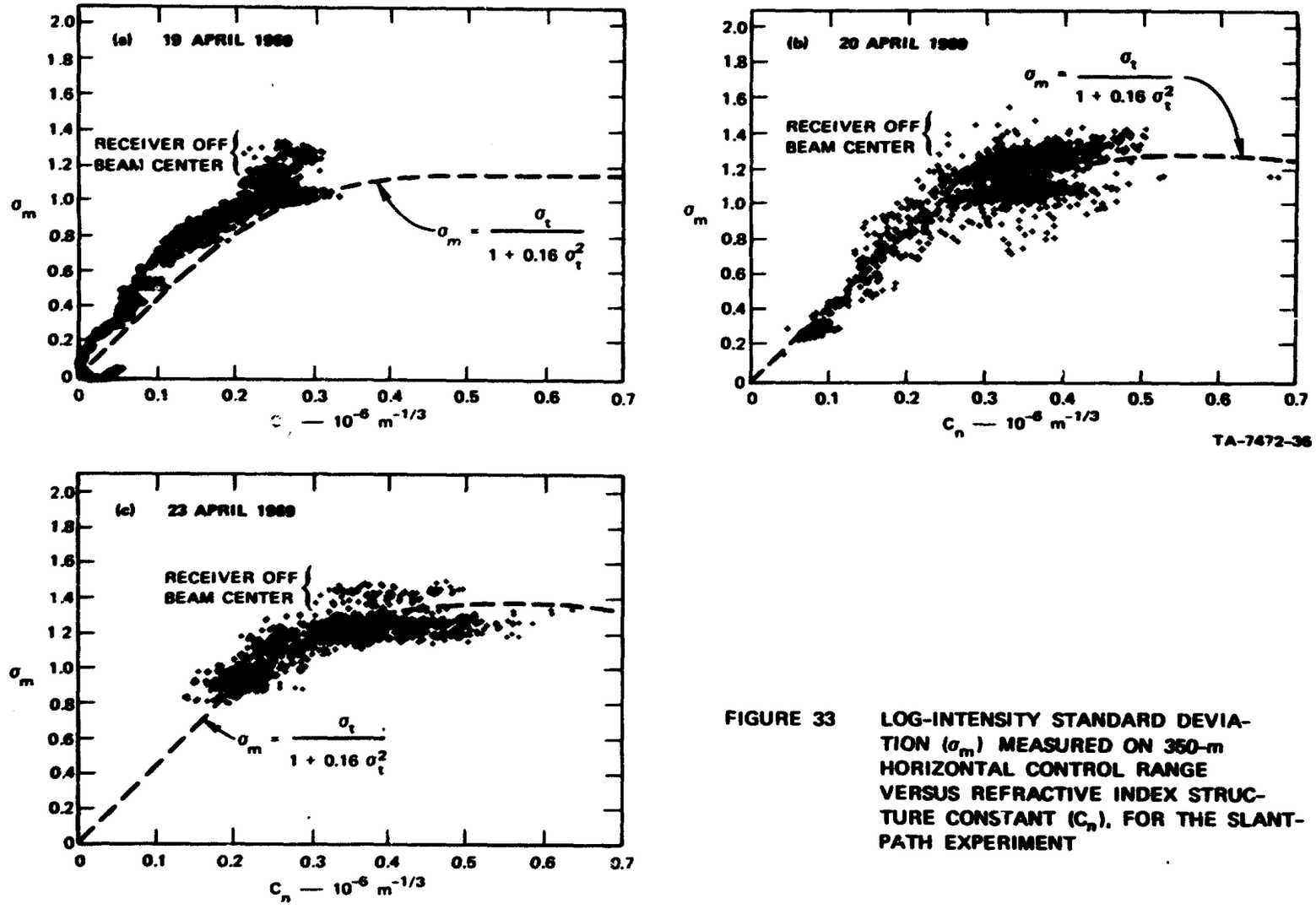

FIGURE 33 LOG-INTENSITY STANDARD DEVIATION (σ_m) MEASURED ON 350-m HORIZONTAL CONTROL RANGE VERSUS REFRACTIVE INDEX STRUCTURE CONSTANT (C_n), FOR THE SLANT-PATH EXPERIMENT

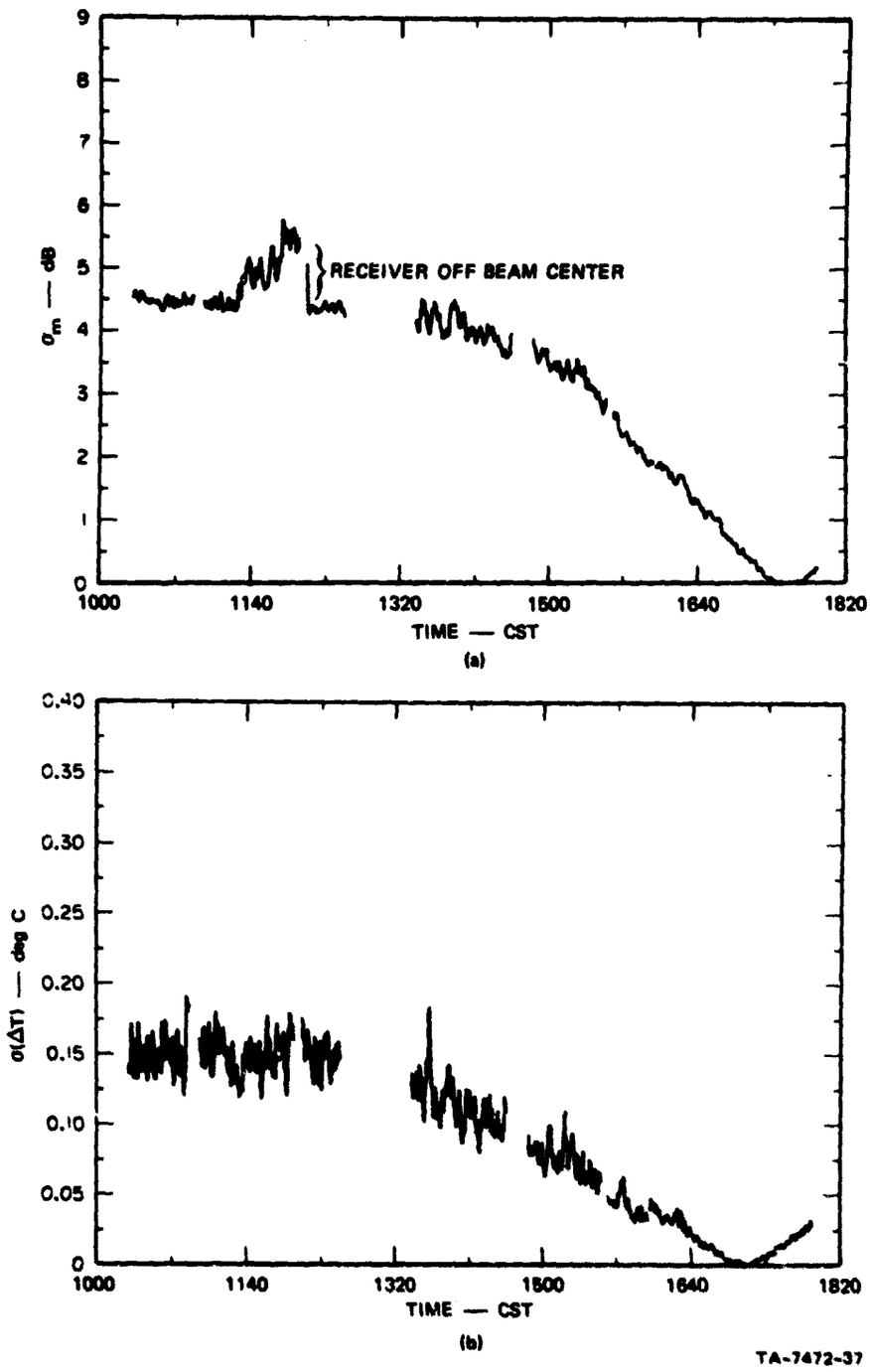

FIGURE 34 TIME VARIATIONS ON 19 APRIL 1969 OF (a) LASER SCINTILLATION ON 350-m HORIZONTAL CONTROL RANGE (σ_m), AND (b) THERMAL TURBULENCE LEVEL [$\sigma(\Delta T)$]

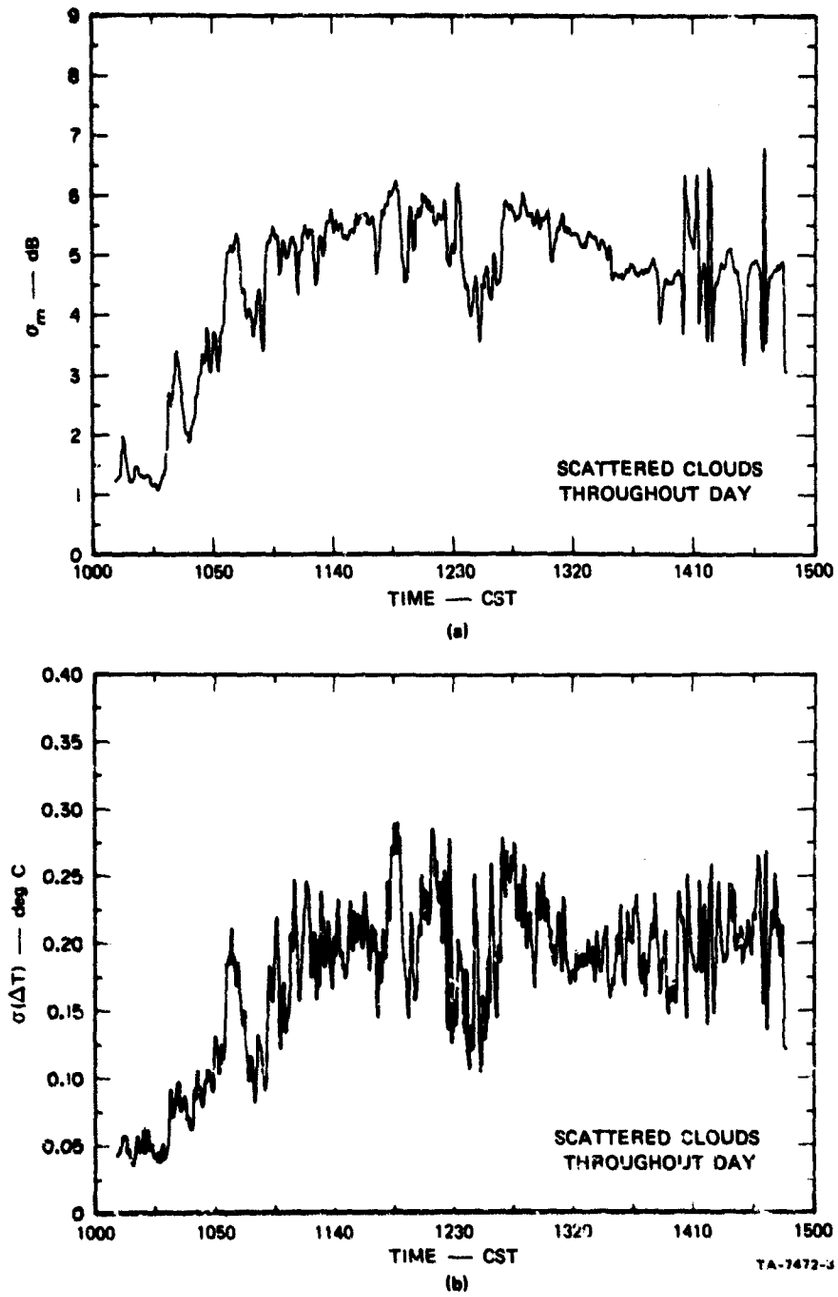

FIGURE 35 TIME VARIATIONS ON 20 APRIL 1969 OF (a) LASER SCINTILLATION ON 350-m HORIZONTAL CONTROL RANGE (σ_m), AND (b) THERMAL TURBULENCE LEVEL [$\sigma(\Delta T)$]. Downward excursions of traces were caused by cloud shadows drifting across range

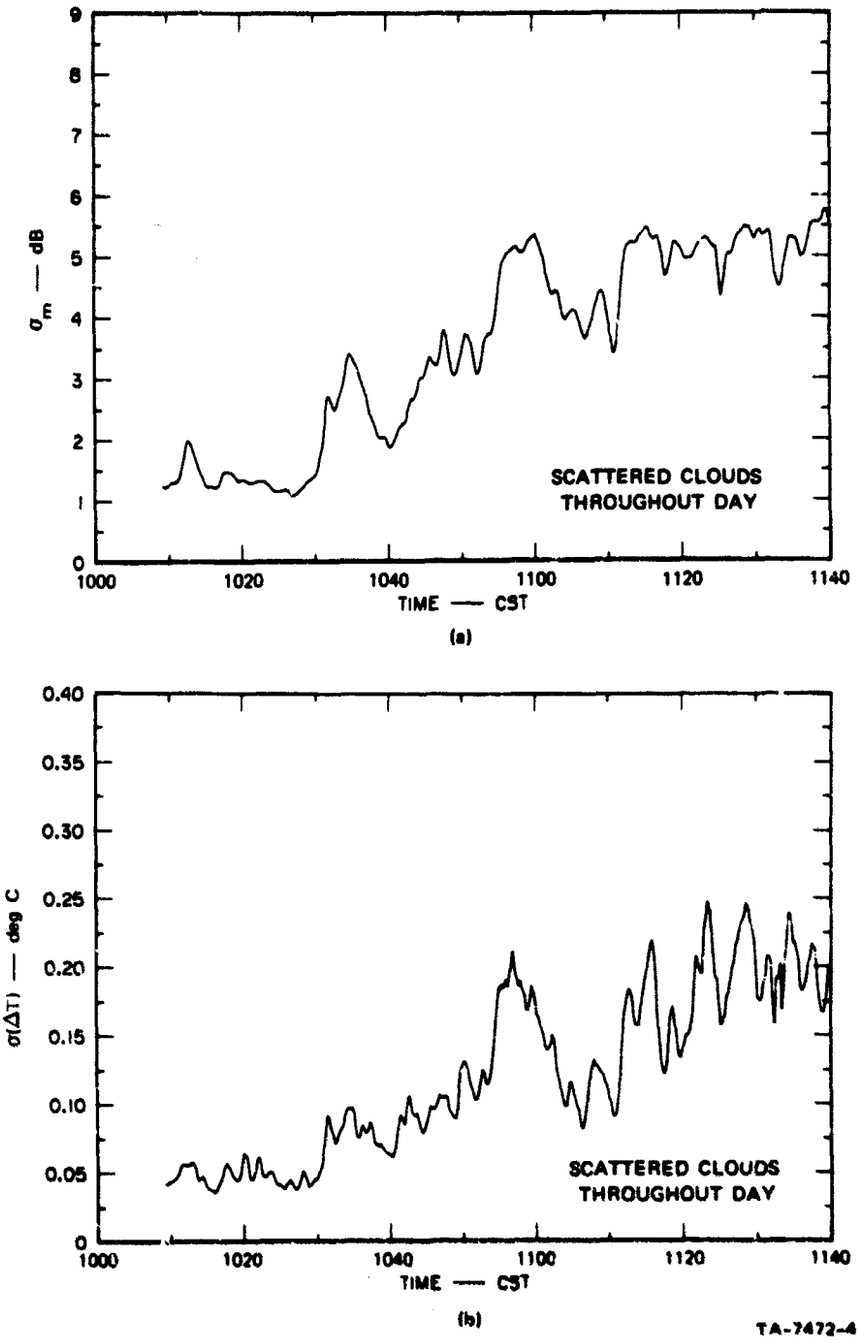

FIGURE 36 INITIAL PORTION OF FIGURE 35 ON ENLARGED TIME SCALE, SHOWING DEGREE OF CORRELATION BETWEEN LASER SCINTILLATION AND THERMAL TURBULENCE LEVEL

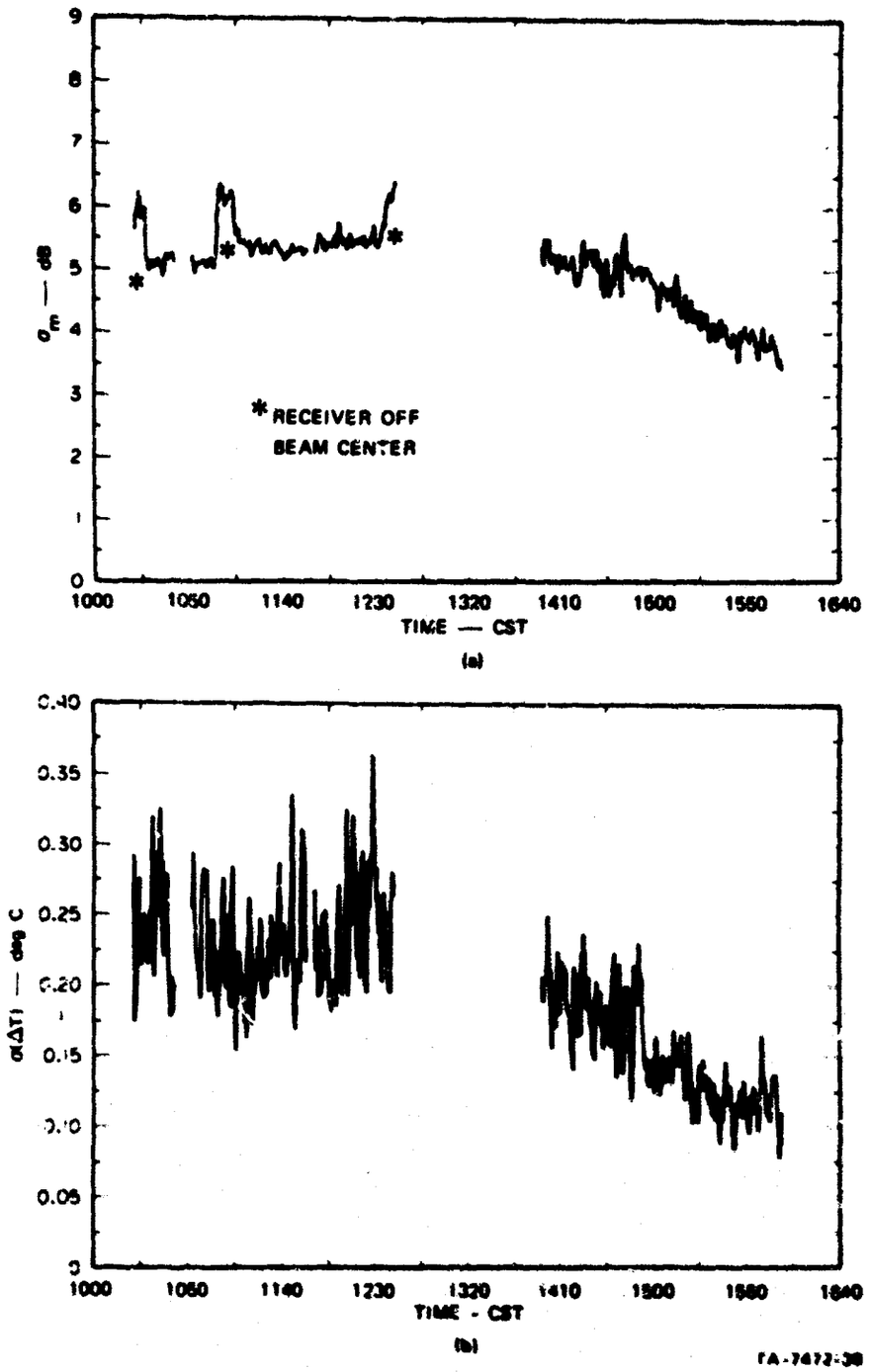

FIGURE 37 TIME VARIATIONS ON 23 APRIL 1969 OF (a) LASER SCINTILLATION ON 350-m HORIZONTAL CONTROL RANGE (σ_m), AND (b) THERMAL TURBULENCE LEVEL [$\sigma(\Delta T)$]

The analog standard deviations used here, as obtained from the Sigma Meter, have been corrected by means of Eqs. (13) and (15), Section III.

The dashed curves in this figure represent the empirical function fit to the data from the Woodland horizontal propagation experiment. The curve fits the data on 20 and 23 April reasonably well, but seems to underestimate the measured values on 19 April. The reason for this is not known, but it could be due to an error in calibration of the amplifier for the differential thermometer on that day, since the measured values of C_n seem abnormally low in comparison with those on the other two days, when the general weather conditions were similar.

A number of the σ_m data points on the three days are anomalously high. As was discussed in Section III, an increase in scintillation magnitude occurs when the laser beam drifts and the receiver is no longer located in the center of the beam. This is what occurred at various times during the experiment. When this condition was noticed, it was immediately corrected by recentering the receiver in the beam. The effect of this realignment procedure is apparent in Figure 34(a) from the character of the trace at about 1200 CST. This figure illustrates the variation of σ_m and $\sigma(\Delta T)$ with time on 19 April. It may be noted that, probably because of the slightly sloping nature of the site, the transition from unstable to adiabatic to stable conditions occurs sooner at the location of the differential thermometer (at the west end of the range) than over the 350-m range as a whole. The adiabatic condition is indicated by the minimum in $\sigma(\Delta T)$ at 1720 CST and the σ_m minimum at 1740 CST. This out-of-phase condition explains the reason for the strange shape in the envelope of data points near the origin in Figure 33(a).

Figure 35 illustrates the time variation in σ_m and $\sigma(\Delta T)$ on 20 April. Although higher frequencies occur in the latter trace because $\sigma(\Delta T)$ represents a point measurement, rather than a line integral as

does σ_m, there is a good correlation between σ_m and $\sigma(\Delta T)$. This can be seen more clearly in Figure 36, which has an expanded time scale. The dips in the traces were caused by cloud shadows drifting across the range from time to time.

The time variation of σ_m and $\sigma(\Delta T)$ on 23 April is presented in Figure 37. As indicated, there were several occasions when beam drifting caused the receiver to be off-center and necessitated realignment. No slant-path data were collected on 23 April.

Figure 38 illustrates the vertical temperature profiles obtained by means of the instrument mounted on the C-131 aircraft. On 19 April at 1215 CST there were temperature inversions present at approximately 1200 m (3900 ft) and 2000 m (6600 ft) above ground. By that afternoon at 1520 CST, the two inversions had apparently merged to form a single inversion layer from 1700 to 2000 m (5600 to 6600 ft). Little structure is apparent in the profiles for 20 April, except for isothermal layers at 1500 m (4900 ft) at 0955 CST and at 1700 m (5600 ft) at 1320 CST.

2. Slant-Path Measurements

For a slant path of length R with the origin of coordinates at the receiver, Tatarski (1961) has shown theoretically that

$$\sigma_t = 1.49\ (2\pi/\lambda)^{7/12} \left[\int_0^R C_n(\vec{r}) r^{5/6} \right]^{1/2} . \qquad (16)$$

In order to evaluate the integral, it is necessary to specify C_n as a function of distance along the slant path. For our work, we have assumed that C_n is horizontally uniform and decreases exponentially with height (z) according to the model

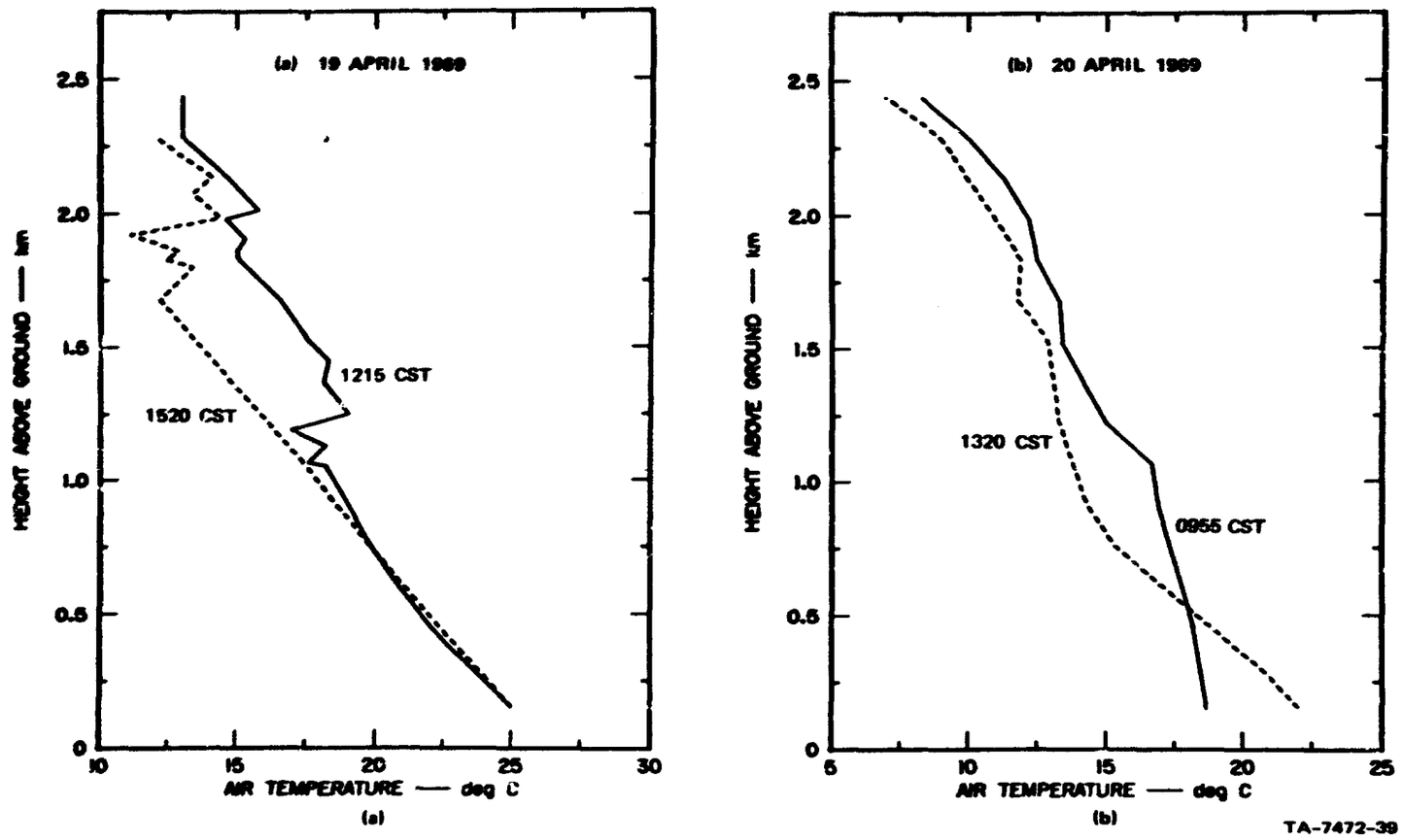

FIGURE 38 VERTICAL TEMPERATURE PROFILES OBTAINED DURING SLANT-PATH EXPERIMENT

$$C_n = C_{no} e^{-kz} \quad , \tag{17}$$

where k is a selectable parameter with units of m^{-1} and C_{no} is the near-ground (2 m) value of C_n. This function is graphed in Figure 39 for two reasonable values of k.

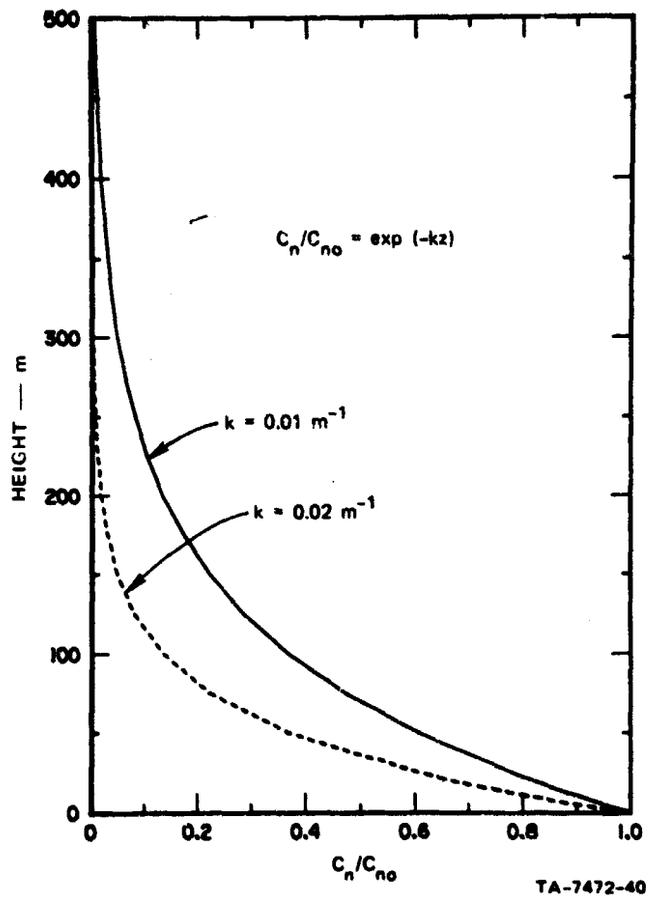

FIGURE 39 ASSUMED EXPONENTIAL FORM FOR VERTICAL PROFILE OF NORMALIZED REFRACTIVE INDEX STRUCTURE CONSTANT

When the C_n profile is substituted into Eq. (16), and geometrical considerations, involving the slant-path elevation angle θ, are taken into account, we obtain the following:

$$\sigma_t = 1.43(2\pi/\lambda)^{7/12} C_{no} A^{1/2} \quad , \tag{18}$$

where the range integral (a) is given by

Case I (ground-based laser):

$$A = A_1 = \int_o^R e^{-B(R-r)} r^{5/6} dr \tag{19}$$

Case II (airborne laser):

$$A = A_2 = \int_o^R e^{-Br} r^{5/6} dr \tag{20}$$

and $B = k \sin \theta$. The value of the constant in Eq. (18) has been changed slightly from Tatarski's plane-wave value to incorporate our results from the horizontal propagation experiment.

The integrals A_1 and A_2 in Equations (19) and (20) are not solvable analytically and must be integrated numerically. Since our experiment involved a ground-based laser, Eq. (20) was used, and values of σ_t were calculated for each run for which a measured value of σ_m on the slant path was available, using values of C_{no} derived from the ground-based measurements. Values of σ_m were obtained from a total of 28 runs; the remaining 10 runs could not be analyzed because of poor

signal-to-noise ratios, or else the data were invalid because of equipment malfunctions.

The measured values (σ_m) are compared with the theoretical values (σ_t) in Table VI and Figure 40. The dashed curves in the figure

Table VI

REDUCED SLANT-PATH DATA, APRIL 1969 EXPERIMENT

Run No.	σ_m (slant)	(°C) $\sigma(\Delta T)$	σ_t (slant) k = 0.01	σ_t (slant) k = 0.02
1	0.80	0.140	1.63	1.17
4	0.94	0.152	1.68	1.17
5	0.87	0.148	1.63	1.14
6	0.94	0.156	1.71	1.20
7	0.71	0.152	1.44	1.04
8	0.69	0.140	1.32	0.95
12	1.10	0.160	1.73	1.21
13	0.99	0.120	1.02	0.71
14	1.13	0.160	1.72	1.20
15	0.80	0.120	1.25	0.90
16	0.64	0.100	1.04	0.75
17	0.67	0.108	1.12	0.81
18	0.62	0.112	1.04	0.75
19	0.69	0.100	0.93	0.68
20	0.62	0.096	1.01	0.72
21	0.71	0.088	0.92	0.66
22	0.92	0.080	0.87	0.61
23	0.80	0.076	0.83	0.58
24	0.85	0.084	1.00	0.70
26	0.76	0.080	1.00	0.70
27	0.71	0.096	0.95	0.69
28	0.83	0.120	1.17	0.85
29	1.29	0.180	2.39	1.73
30	1.17	0.200	3.33	2.39
32	0.87	0.188	1.82	1.32
36	0.67	0.180	1.75	1.27
37	0.67	0.160	2.10	1.52
38	0.67	0.048	0.79	0.57

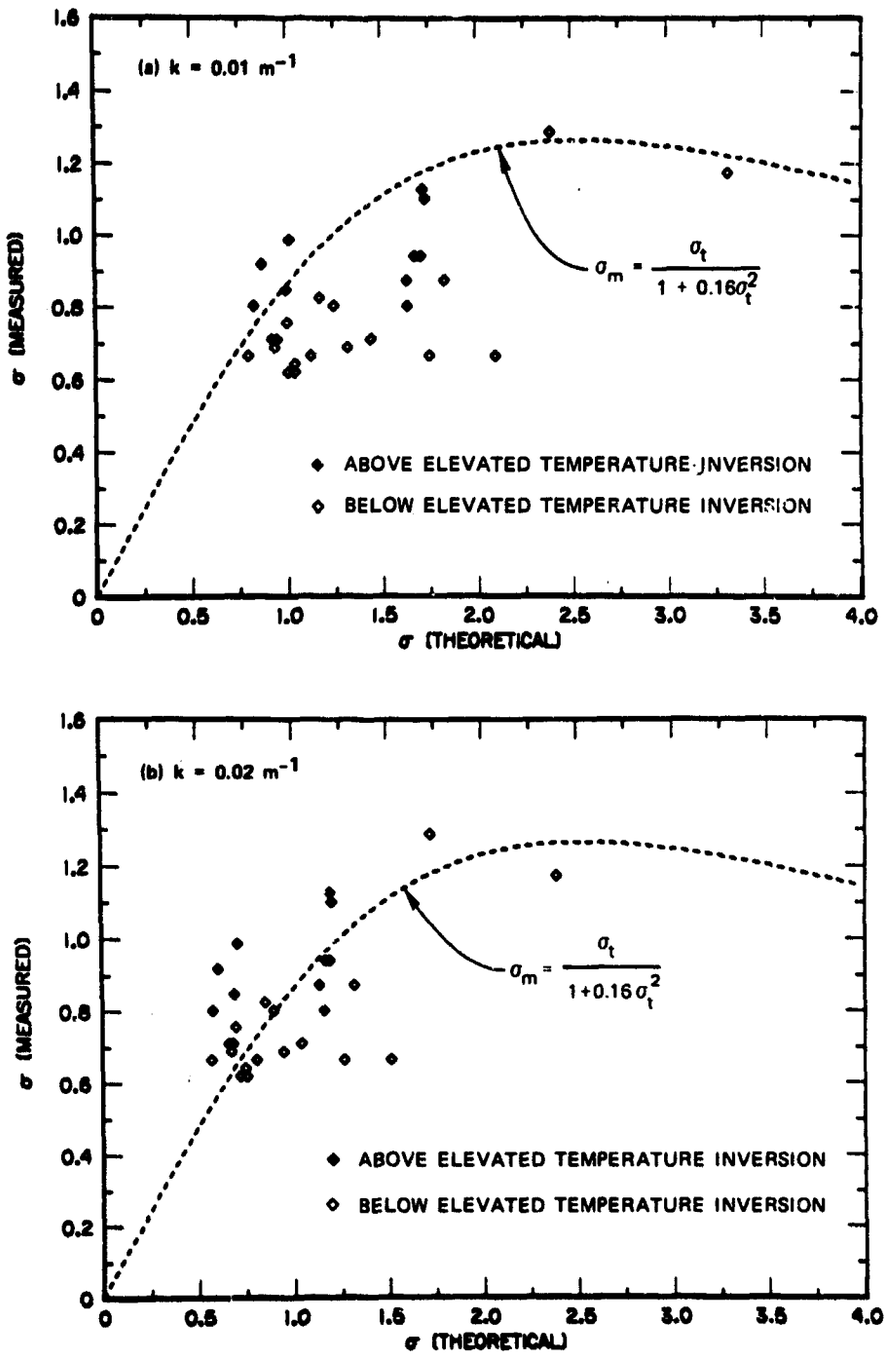

FIGURE 40 MEASURED LOG-INTENSITY STANDARD DEVIATION ON THE SLANT PATH AS A FUNCTION OF THE THEORETICAL VALUE, ASSUMING TWO VALUES OF k IN THE EXPONENTIAL MODEL $C_n = C_{no} \exp(-kz)$. The dashed curves represent the empirical function previously fit to the data from the horizontal propagation experiment

represent the same empirical function previously fit to the data from the Woodland horizontal propagation experiment. Although there is a fairly large scatter in the data points, the data are represented reasonably well by the empirical function, at least for $k = 0.02\ m^{-1}$.

It is apparent from Figure 40 that the values of σ_t obtained during the experiment were not large enough to provide an adequate test of the supersaturation effect with regard to scintillation magnitude that was found during the Woodland experiment. The laser we used for the slant-path experiment did not have enough power to permit measurements at longer ranges, which would have given larger values of σ_t. There is some evidence from these slant-path data that scintillation saturation is occurring in the range from $\sigma_t = 1.5$ to 3.0, but measurements at longer ranges will be necessary to confirm the supersaturation effect on the slant path.

As shown in Figure 40, there is a slight tendency for the measured scintillation values to be greater when the propagation path went through an elevated temperature inversion layer, indicating that the thermal turbulence frequently present in such layers may be significant in enhancing scintillation.

Although no power spectra were computed for t slant-path data, it was apparent in the raw data (see Figure 31, Secti IV-E) that the scintillation frequencies were much higher than those observed during the horizontal-path experiment. The dominant frequencies of scintillation on the slant path were typically in the range 1000-4000 Hz, while those in the Woodland experiment were generally on the order of 100-200 Hz. These higher frequencies are caused by the pseudo-wind effects caused by the movement of the aircraft and laser beam.

Before proceeding to the next section, it is worth noting that Eqs. (18), (19), and (20) predict that, for the same range, wavelength,

and ground-level C_n value, the scintillation magnitude will be largest for a near-ground horizontal path [for which Eq. (18) reduces to Eq. (9)], next largest for a slant path with a ground-based laser, and least for the same slant path but with an airborne laser. This is the case because thermal turbulence has the most effect near the laser source. The equations also show that for a given range, the scintillation magnitude decreases with increasing slant-path elevation angle, and reaches a minimum for a vertical (90°) propagation path.

V INCORPORATION OF EXPERIMENTAL RESULTS INTO LASER EYE SAFETY GUIDELINES

A. General

In the previous report on this project (Johnson et al., 1968), a procedure was described for estimating the probability of eye damage from exposure to a laser beam. Similar work has been reported by Deitz (1968, 1969). The new eye-hazard evaluation procedure presented in this section incorporates revisions that (1) reflect the results of our latest experimental work, and (2) streamline the procedure to make it easier to use on an operational basis. The equations and assumptions underlying each part of the eye-hazard evaluation procedure (as represented by Figures 41-48 and Tables VII and VIII) will be briefly explained in a subsequent section.

It should be emphasized that these eye-safety guidelines should be considered tentative and used with caution until the new experimental results that they reflect can be confirmed for a variety of laser-beam and propagation-path configurations.

B. Eye-Hazard Evaluation Procedure

The input parameters required for the eye-hazard evaluation procedure are as follows:

Φ, latitude (deg)

U, surface wind speed (knots)

V, atmospheric visibility (miles)

N, cloud cover (tenths)

θ, slant path elevation angle (deg)

R, range (km)

P, laser peak power (W)

Q, laser pulse rate (pulses/s)

λ, laser wavelength (μ)

β, laser beam divergence (mrad)

d, minimum beam diameter (m)

T, exposure time (s)

Laser type (CW, long pulse, or Q-switched)

Type of slant path (ground-based or airborne laser)

Date and time

Using the above information, the probability of eye damage may be estimated by the method outlined below.

(1) In the case of relatively low-power lasers, go to Step (2). For other lasers, skip to Step (3).

(2) Divide the LASER POWER P (W) by the minimum beam area $\pi d^2/4$ (m^2), using the MINIMUM BEAM DIAMETER d (m) to compute the maximum power density available for eye damage (W/m). If this value does not exceed the appropriate MAXIMUM SAFE POWER DENSITY LEVEL (I_{safe}) given in Table VIII, then the laser can be considered safe and the rest of the procedure disregarded.

(3) Use TIME OF YEAR, HOUR OF DAY, and LATITUDE ϕ in Figure 41 to find SOLAR ELEVATION ANGLE α. Interpolate between graphs for dates between those given. For

latitudes in the southern hemisphere, reverse the dates on graphs (a) and (c). For nighttime, proceed to Step (5).

(4) Use α and CLOUD COVER N (tenths) in Figure 42 to find INSOLATION CATEGORY S (strong, moderate, or weak).

(5) For daytime, use S and SURFACE WIND U (knots) in Table VII to find NEAR-GROUND REFRACTIVE INDEX STRUCTURE CONSTANT C_n ($10^{-6} m^{-1/3}$). For nighttime, use last two columns of table, given N.

(6) For a near-ground horizontal propagation path, proceed to Step (8). For a slant path, use RANGE R (km) and SLANT PATH ELEVATION ANGLE θ in Figure 43 to find RANGE INTEGRAL A ($m^{-11/6}$).

(7) For a slant path, use A, C_n, and LASER WAVELENGTH λ (μ) in Figure 44 to find LOG-INTENSITY STANDARD DEVIATION σ. [Proceed to Step (9)].

(8) For a near-ground horizontal path, use R, C_n, and LASER WAVELENGTH λ (μ) in Figure 45 to find LOG-INTENSITY STANDARD DEVIATION σ.

(9) Use ATMOSPHERIC VISIBILITY V (miles), LASER BEAM DIVERGENCE β (milliradians), and R in Figure 46 to find NORMALIZED MEAN POWER DENSITY $\bar{I}/P$ (m^{-2}).

(10) Multiply $\bar{I}/P$ by LASER POWER P (W) to obtain MEAN POWER DENSITY $\bar{I}$ ($W\ m^{-2}$).

(11) Use λ and LASER TYPE (Q-switched, long pulse, or CW) in Table VIII to obtain MAXIMUM SAFE POWER DENSITY

I_{safe} ($W\ m^{-2}$). For a CW laser, use the following exposure times: (1) < 1 ms for a slant path involving an aircraft; (2) 1-10 ms for static paths and U > 10 knots; (3) 10 ms - 1 s for static paths and U ≤ 10 knots.

(12) Divide I_{safe} by $\bar{I}$ to obtain SAFE-TO-MEAN-POWER-DENSITY RATIO $I_{safe}/\bar{I}$.

(13) Use σ and $I_{safe}/\bar{I}$ in Figure 47 to obtain INSTANTANEOUS PROBABILITY OF EYE DAMAGE γ.

(14) Use γ and EVENT FREQUENCY F (s^{-1}) in Figure 48 to obtain INTEGRATED PROBABILITY OF EYE DAMAGE Γ, for given EXPOSURE TIME T. For pulsed lasers, set F equal to the LASER PULSE RATE Q (pulses/s). For CW lasers, set F equal to the values given below:

Static path

U ≤ 10 knots: F = 500

U > 10 knots: F = 1000

Aircraft path: F = 5000

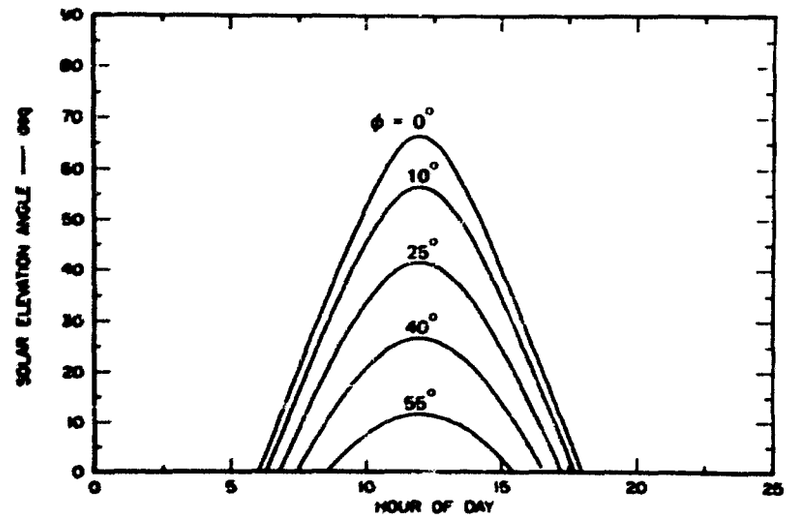

(a) NORTHERN HEMISPHERE WINTER SOLSTICE (DECEMBER 21)

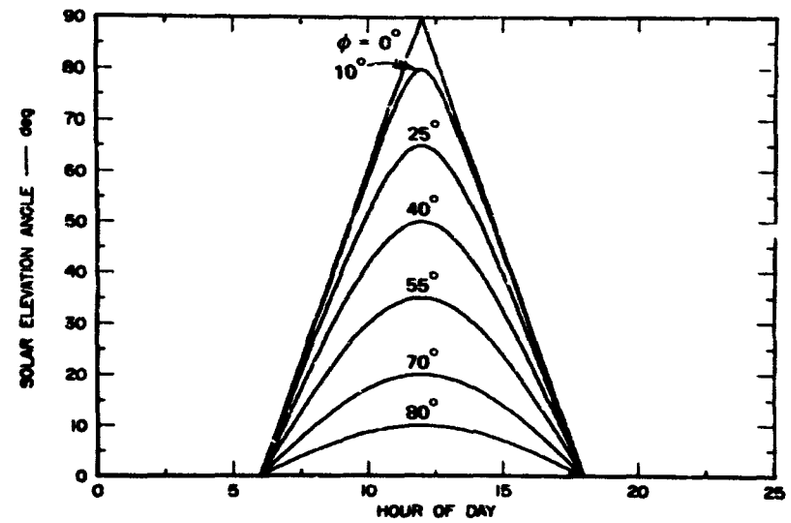

(b) EQUINOXES (MARCH 21 AND SEPTEMBER 31)

TA-7472-50

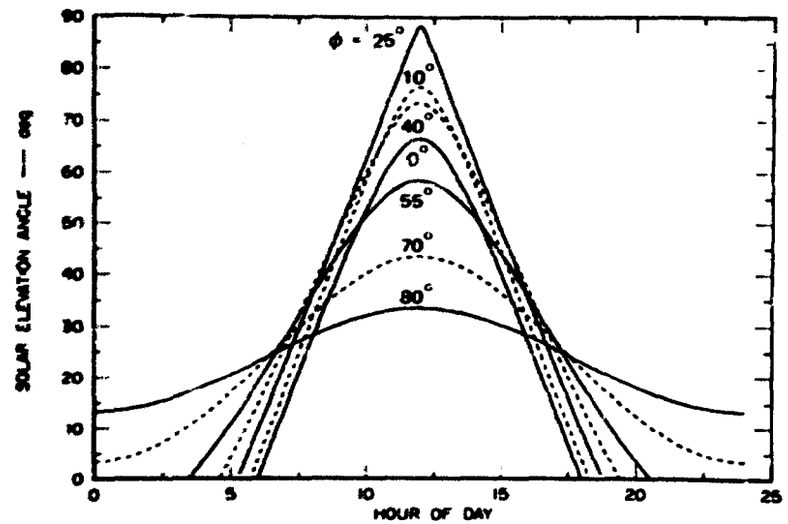

(c) NORTHERN HEMISPHERE SUMMER SOLSTICE (JUNE 21)

FIGURE 41 SOLAR ELEVATION ANGLE (α) AS A FUNCTION OF HOUR OF DAY AND LATITUDE (ϕ) FOR VARIOUS TIMES OF YEAR

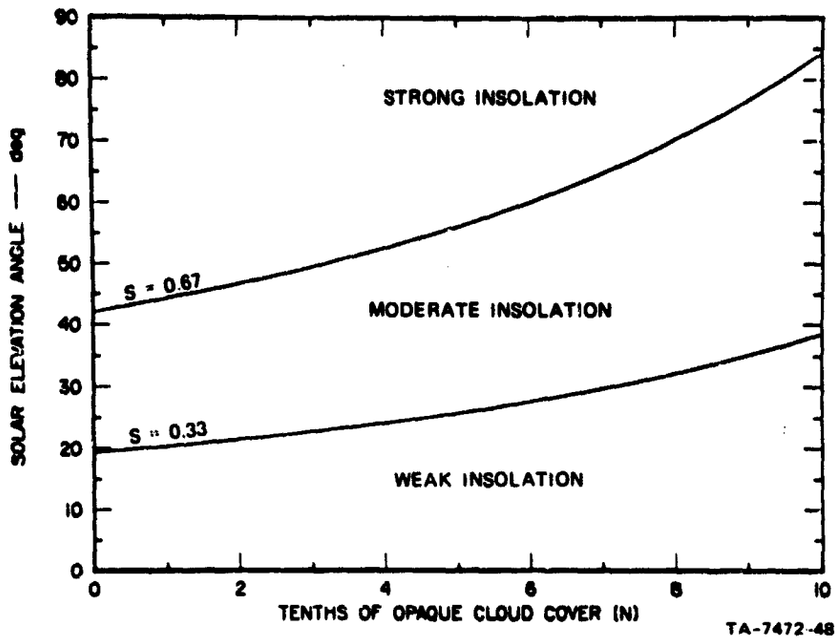

FIGURE 42 INSOLATION CATEGORY (S) AS A FUNCTION OF SOLAR ELEVATION ANGLE (γ) AND TENTHS OF OPAQUE CLOUD COVER (N)

Table VII

RELATION OF NEAR-GROUND (2 m) REFRACTIVE INDEX STRUCTURE CONSTANT (C_n) TO WEATHER CONDITIONS

Surface Wind (knots)	C_n (10^{-6} $m^{-1/3}$)				
	Daytime Insolation Category (S)			Nighttime Conditions	
	Strong	Moderate	Weak	Thin Overcast or ≥ 5/10 Cloudiness	≤ 4/10 Cloudiness
< 3	0.60	0.50	0.40	0.30	0.40
3-6	0.50	0.40	0.25	0.20	0.35
6-10	0.40	0.25	0.15	0.10	0.20
10-12	0.20	0.12	0.05	0.05	0.05
> 12	0.12	0.05	0.05	0.05	0.05

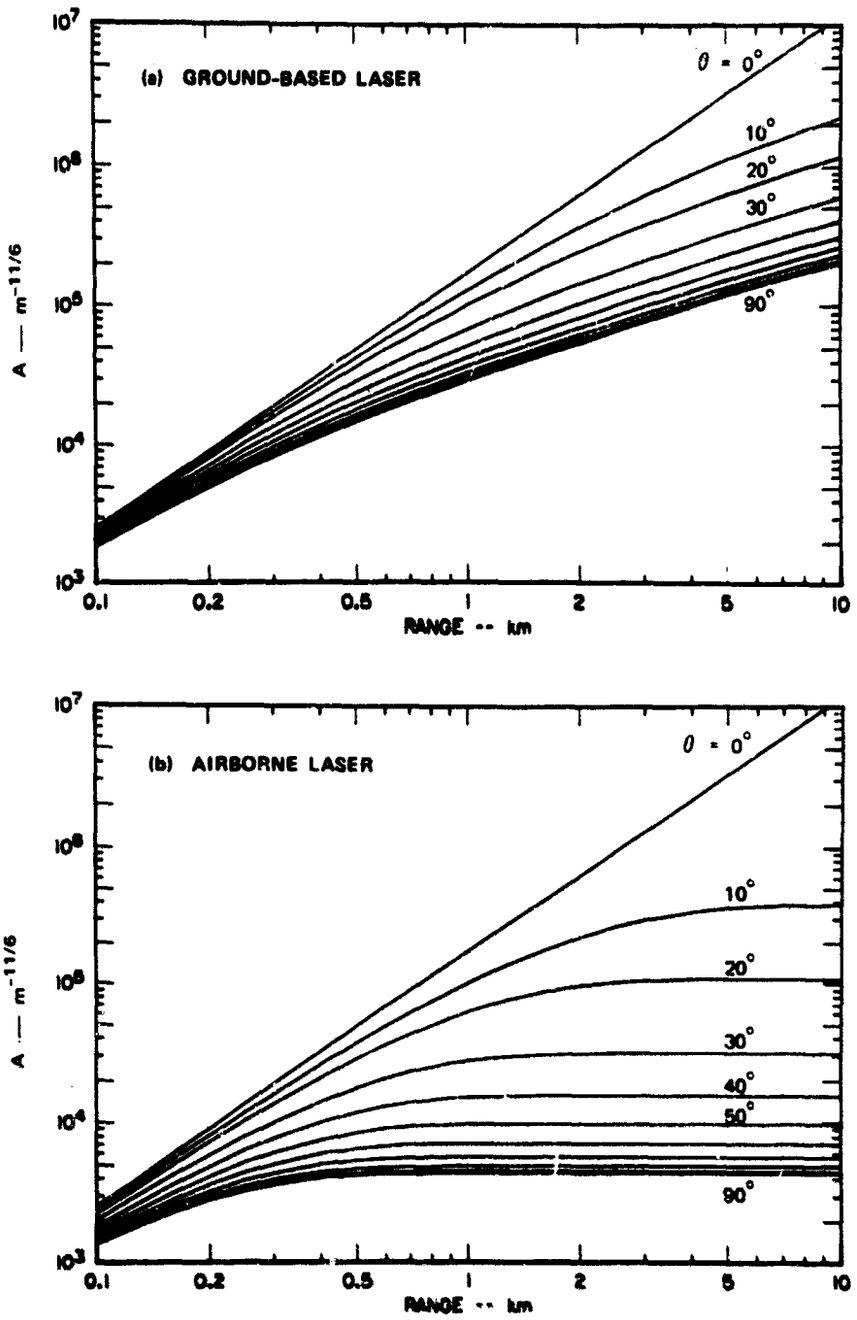

FIGURE 43 RANGE INTEGRAL (A) AS A FUNCTION OF RANGE (R) AND SLANT-PATH ELEVATION ANGLE (θ), FOR THE TWO TYPES OF SLANT PATHS

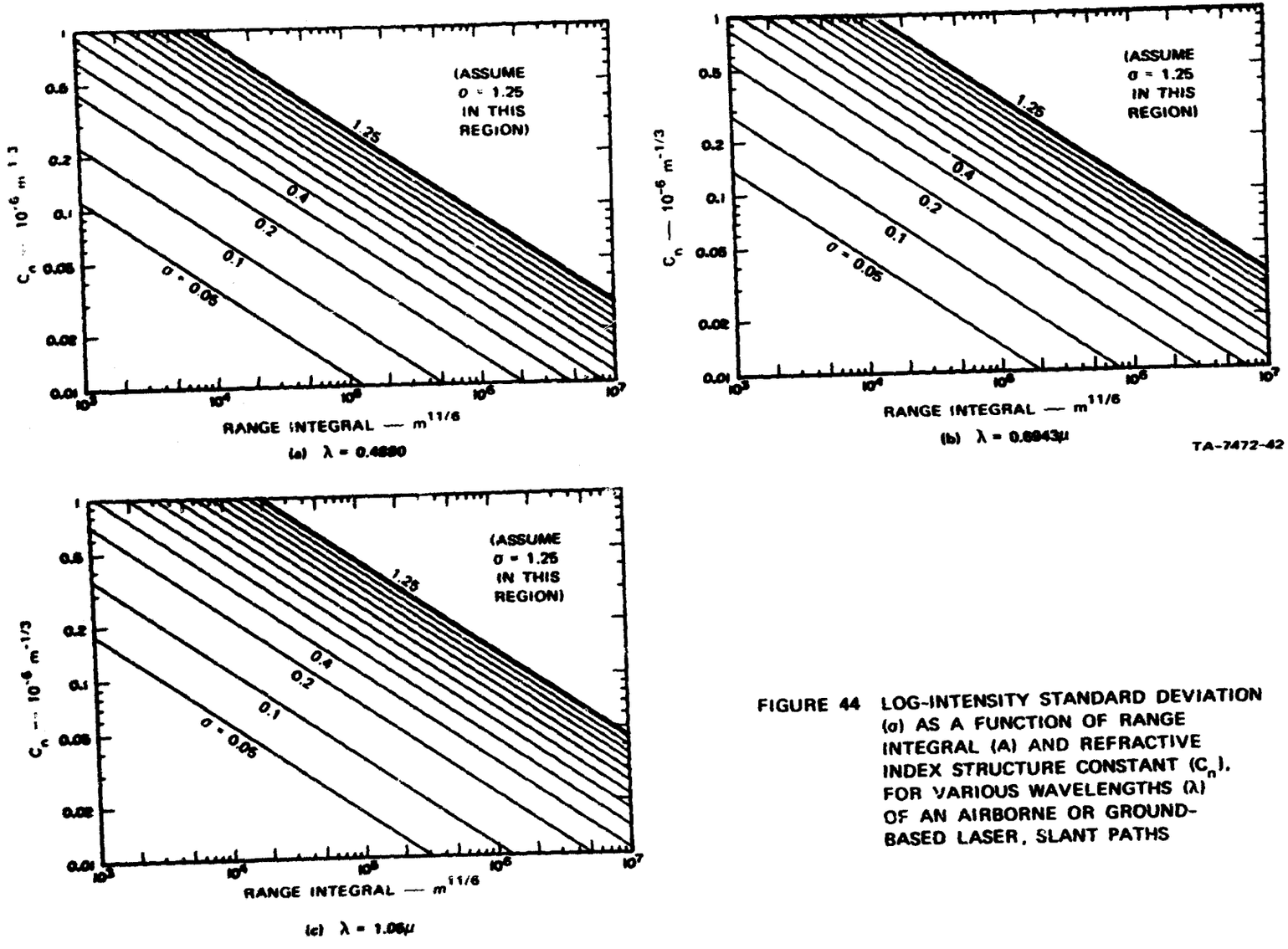

FIGURE 44 LOG-INTENSITY STANDARD DEVIATION (σ) AS A FUNCTION OF RANGE INTEGRAL (A) AND REFRACTIVE INDEX STRUCTURE CONSTANT (C_n), FOR VARIOUS WAVELENGTHS (λ) OF AN AIRBORNE OR GROUND-BASED LASER, SLANT PATHS

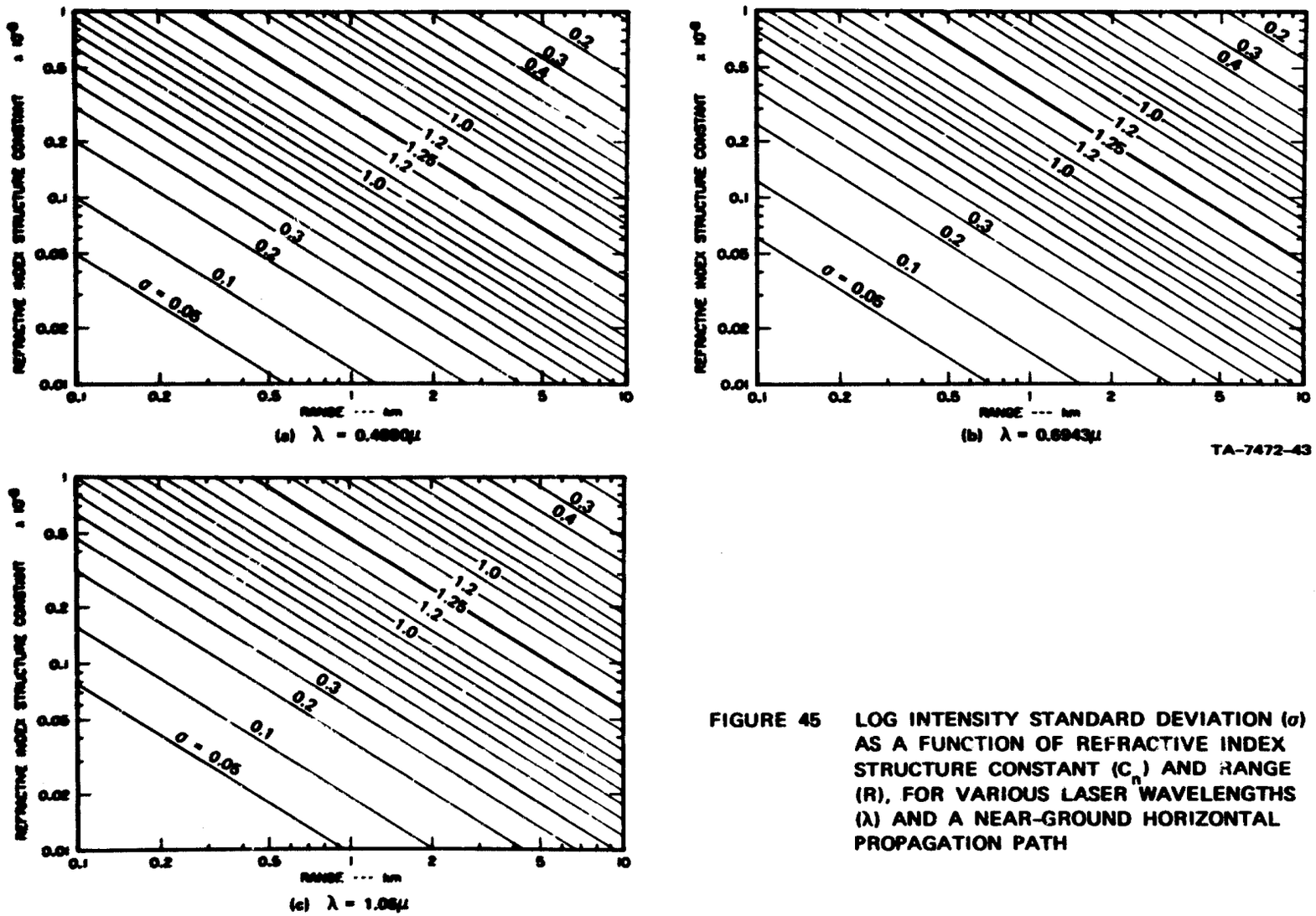

FIGURE 45 LOG INTENSITY STANDARD DEVIATION (σ) AS A FUNCTION OF REFRACTIVE INDEX STRUCTURE CONSTANT (C_n) AND RANGE (R), FOR VARIOUS LASER WAVELENGTHS (λ) AND A NEAR-GROUND HORIZONTAL PROPAGATION PATH

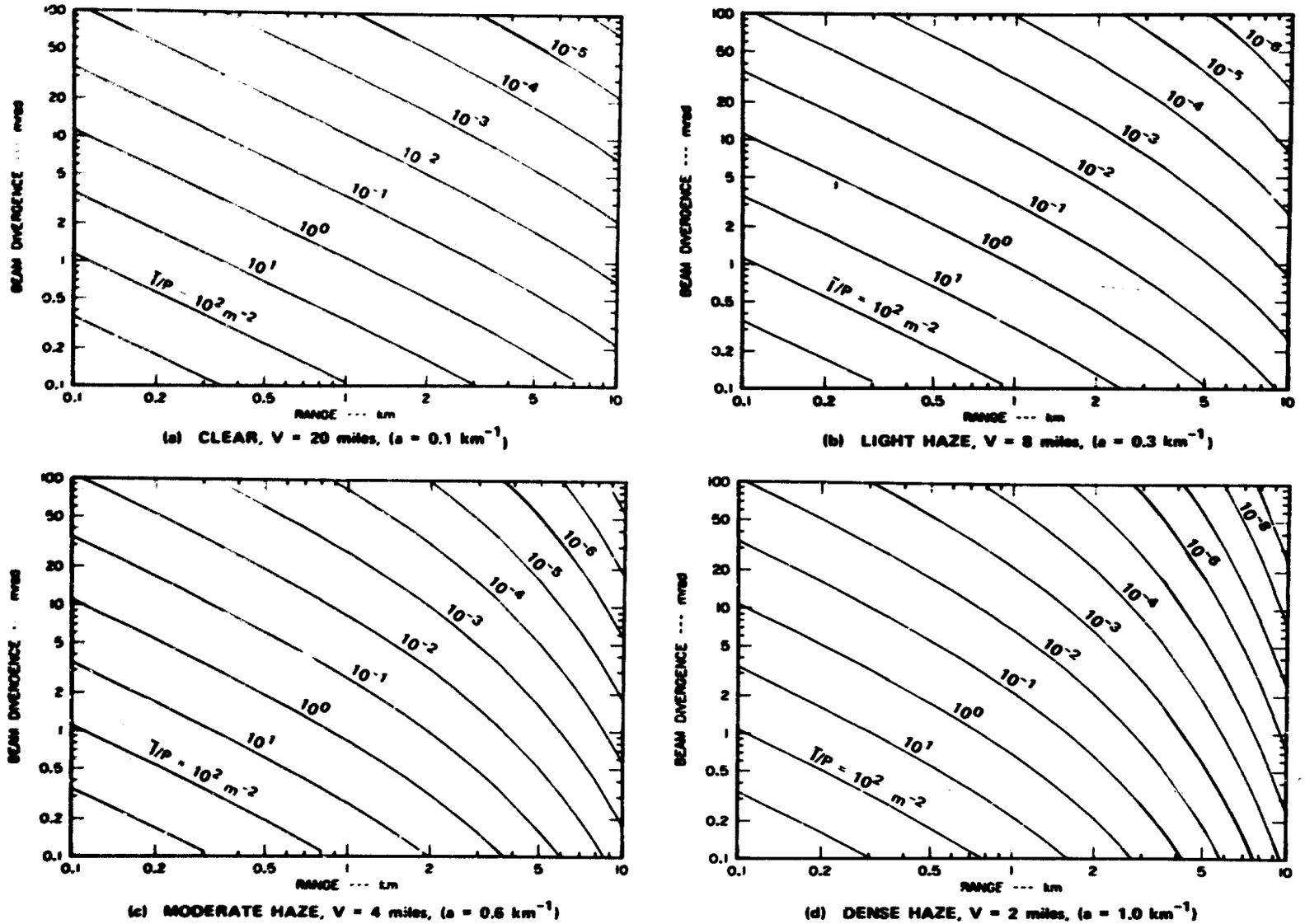

FIGURE 46 NORMALIZED MEAN POWER DENSITY ($\bar{I}/P$) AS A FUNCTION OF BEAM DIVERGENCE ANGLE (β) AND RANGE (R), FOR VARIOUS VALUES OF ATMOSPHERIC VISIBILITY (V)

Table VIII

MAXIMUM SAFE POWER DENSITY LEVELS (I_{safe})
FOR CORNEAL EXPOSURES (RECOMMENDED
BY USAF MANUAL AFM 161-8, 1969)

I_{safe} (W/m^2)

Laser Wavelength (μ)	Time	Q-Switched (20 ns)	Long Pulse (1 ms)	CW <1ms	CW 1-10ms	CW 10ms-1s
1.0600	Day	3.21×10^{8}	7.15×10^{4}	---	---	---
	Night	0.59×10^{8}	1.30×10^{4}	---	---	---
0.6943 - 0.6328	Day	5.35×10^{6}	1.43×10^{4}	2.86×10^{3}	1.43×10^{3}	7.15×10^{2}
	Night	0.98×10^{6}	0.26×10^{4}	0.52×10^{3}	0.26×10^{3}	1.30×10^{2}
0.5145 - 0.4880	Day	---	---	2.86×10^{3}	1.43×10^{3}	7.15×10^{2}
	Night	---	---	0.52×10^{3}	0.26×10^{3}	1.30×10^{2}

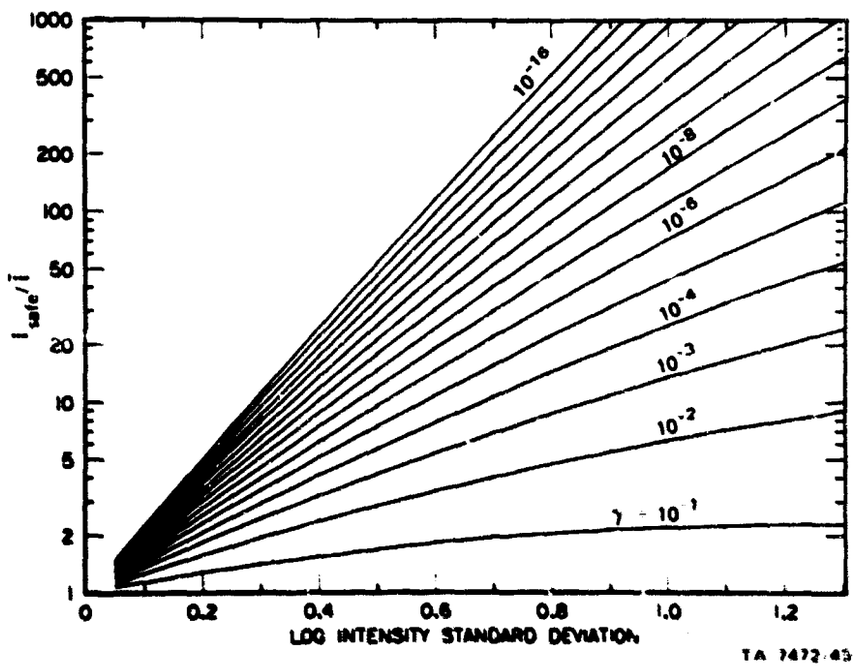

FIGURE 47 INSTANTANEOUS PROBABILITY OF EYE DAMAGE (γ) AS A FUNCTION OF LOG-INTENSITY STANDARD DEVIATION (σ) AND SAFE-TO-MEAN POWER DENSITY RATIO ($I_{safe}/\bar{I}$)

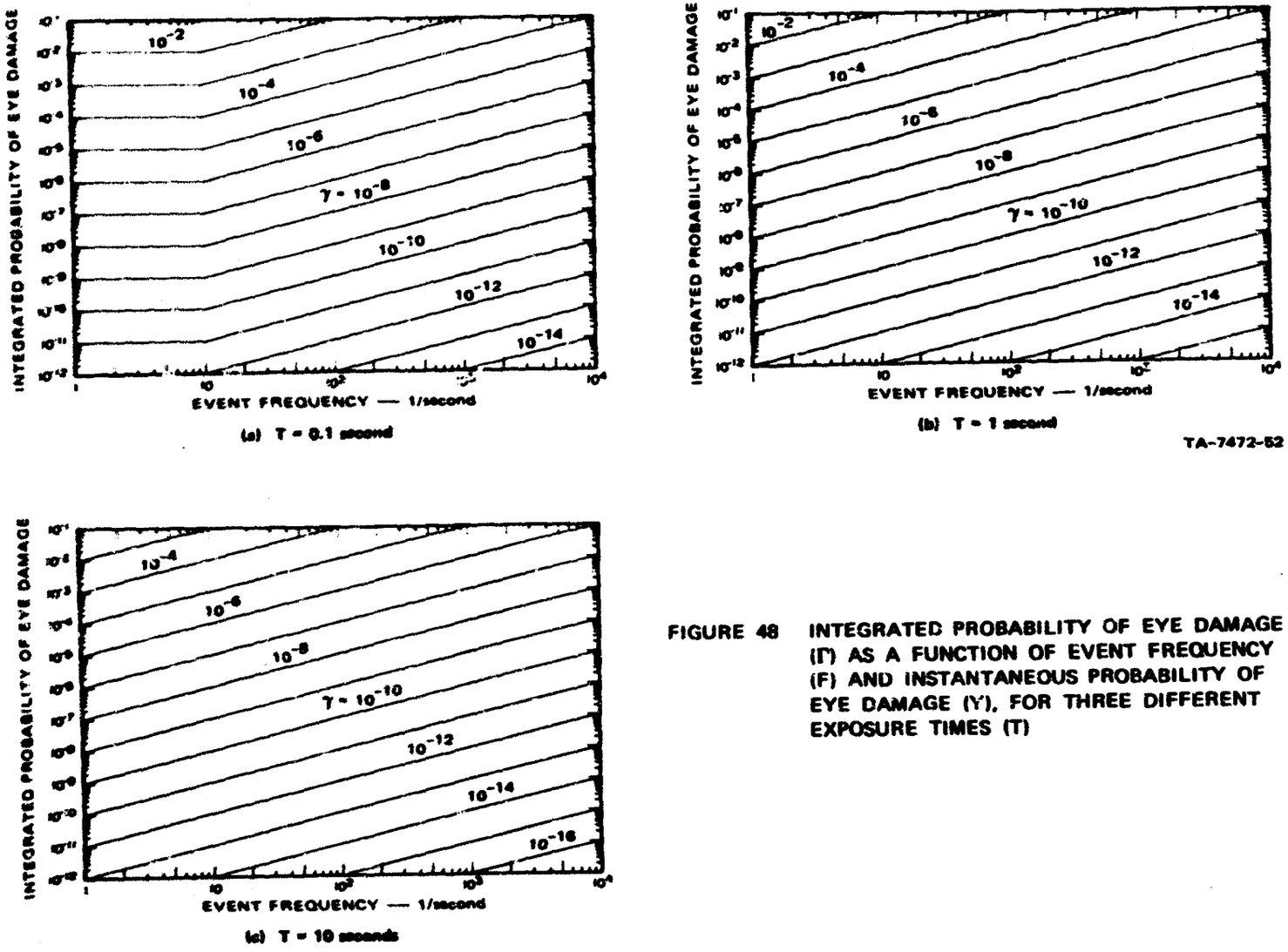

FIGURE 48 INTEGRATED PROBABILITY OF EYE DAMAGE (Γ) AS A FUNCTION OF EVENT FREQUENCY (F) AND INSTANTANEOUS PROBABILITY OF EYE DAMAGE (γ), FOR THREE DIFFERENT EXPOSURE TIMES (T)

C. Basis for Eye Hazard Evaluation Procedure

1. Figure 41

The curves in this figure are based upon the following equation (Smithsonian Meteorological Tables, 1963):

$$\alpha = \sin^{-1}\left\{\sin\Phi\sin\zeta + \cos\Phi\cos\zeta\cos[0.262(h-12)]\right\} \quad , \qquad (21)$$

where α = solar elevation angle

Φ = latitude

ζ = solar declination

h = hour of day.

2. Figure 42

The relative insolation strength (S), on a scale from zero to one, is given by

$$S = \sin\alpha \qquad (22)$$

for a cloudless, nonattenuating atmosphere. When the cloud cover (N) in tenths is considered and the albedo of the clouds is taken to be 0.5, Eq. (22) becomes

$$S = \sin[\alpha(1 - 0.5N/10)] \quad , \qquad (23)$$

which is the basis for Figure 42. The categories of S (strong, moderate, and weak insolation) were determined simply by dividing the range of S into three equal intervals: 0 - 0.33, 0.33 - 0.67, and 0.67 - 1.0.

3. Table VII

This table is based principally upon empirical data from our experiments and those of other investigators, such as Wright and Schutz (1967), Fried et al. (1967), Davis (1966), and Goldstein et al. (1965).

Unfortunately, most of the values of C_n reported by these other workers have not been accompanied by a full account of the concurrent meteorological conditions. Hence the dependence of C_n upon weather conditions as given in the table is based largely upon our measurements. The values in the table must be considered only as approximate, since some extrapolation was required, and also since at least one important variable, ground condition, has been omitted for the sake of simplicity.

The basic structure of the table is patterned after that given by Pasquill and Meade (see Slade, 1968) for the estimation of atmospheric stability categories. Since C_n is related to the absolute value of the stability, appropriate values of C_n were substituted for those of stability category.

4. Figure 43

Equations (19) and (20) (Section IV-F) were used for the computations for the curves presented in this figure. The value of the constant k was taken to be 0.01 (see Figure 39, Section IV-F) in order that the eye-hazard estimates be on the conservative (safe) side.

5. Figure 44

This figure was based upon Eq. (18), Section IV-F, for the slant-path configuration, but we have limited σ to a maximum value of 1.25. The curves are thus derived from the Tatarski relationship but take into account the saturation effect indicated by experimental results. Since the occurrence of scintillation supersaturation on the slant path has not yet been adequately confirmed, we have not made any allowance for this. In not doing so, we have erred, if at all, on the safe side.

6. Figure 45

This figure uses Eqs. (9) and (11), Section III-F, and incorporates the supersaturation effect as observed during the horizontal propagation experiment. It is significant in the eye-hazard context

that, as shown in the figure, the scintillation magnitude (σ) reaches a maximum value of 1.25 and then decreases for increasing range and C_n.

7. Figure 46

This figure is derived principally from considerations of the laser-beam geometry, represented by the equation

$$\bar{I}/P = \frac{4G}{\pi\beta^2 R^2} \quad , \tag{24}$$

where $\bar{I}$ = mean power density (W/m^2) (assumed to be uniform across the beam)

P = laser output peak power (W)

β = beam divergence (milliradians)

R = range (km)

G = atmospheric transmission.

The transmission is given by

$$G = e^{-aR} \quad , \tag{25}$$

where a is the attenuation coefficient (km^{-1}). To a first approximation, the relation between the atmospheric visibility (V, miles) and the attenuation coefficient is given by

$$V = 2.43/a \tag{26}$$

for visible and near-infrared wavelengths.

8. Table VIII

The maximum safe power density levels (I_{safe}, W/m^2) given in this table are those recommended by the U.S. Air Force in AFM 161-8 (1969).

9. Figure 47

The curves in this figure were computed by means of the following equations:

$$\gamma = \frac{1}{\sqrt{2\pi}} \int_{M}^{\infty} \exp(-x^2/2)dx \quad , \tag{27}$$

where γ is the instantaneous probability of eye damage, x is a dummy variable, and

$$M = \sigma/2 + \sigma^{-1} \ln (I_{safe}/\bar{I}) \quad , \tag{28}$$

where σ is the log intensity standard deviation. The development of these equations, as detailed in the last report (Johnson et al., 1968), involves the assumption of a log-normal probability distribution of intensity fluctuations. For convenience, these derivations are reproduced in the Appendix.

10. Figure 48

When one looks at a laser beam continuously for T seconds, the integrated probability of eye damage (Γ) over that period will be greater than the instantaneous probability of eye damage (γ). One simple way to assess this increased probability is to assume that the intensity peaks occurring at a single observational point represent separate events. If ($1-\gamma$) corresponds to the probability of no damage for a single event (i.e., the probability that any one intensity peak will not exceed I_{safe}), then the integrated probability of no damage ($1-\Gamma$) for a given number of occurrences (M) in the time period (T) is given simply by multiplying the individual probabilities:

$$1-\Gamma = (1-\gamma)^M \quad ,$$

$$\text{or} \qquad \Gamma = 1 - (1-\gamma)^M \quad .$$

Since M = FT, where F is the frequency of events,

$$\Gamma = 1 - (1-\gamma)^{FT} \quad . \tag{29}$$

This equation forms the basis for Figure 48.

The event frequency F may be considered to be equivalent to the pulse rate for a pulsed laser, or to the scintillation frequency in the case of a CW laser. If we assume the turbulent elements separated by a mean correlation distance (ρ_o) to move with the wind, then to a first approximation we have

$$F = U_n/\rho_o \quad ,$$

where U_n is the wind component perpendicular to the propagation path. Since the variation in ρ_o with range that is predicted by theory disagrees with that measured, it seems best for our purposes to assume that F depends only upon wind speed and beam sweep rate. On the basis of our measurements, the following values have been selected as being representative of the cases given:

Static paths

$U \leq 10$ knots: $F = 500$

$U > 10$ knots: $F = 1000$

Aircraft slant paths: $F = 5000$

These coefficients allow for the maximum scintillation frequencies observed during our experiments.

11. Setting a Level of Acceptable Risk

After the probability of eye damage (Γ) is found, it becomes necessary to compare this value with a preestablished value (Γ_{safe}) representing the highest probability judged to be an acceptable risk. The magnitude of Γ_{safe} may change as the nature of the situation changes, but values in the range of 10^{-3} to 10^{-5} (1 chance of eye damage in 1000 to 100,000 occurrences) seem reasonable. By way of comparison, the probability of an average American being killed in an automobile accident in the year 1968 was 1 in 3600, or 2.8×10^{-4}, while the probability of being injured in an automobile accident was 1 in 100, or 10^{-2} (World Almanac, 1970).

D. Examples of Use of Eye-Hazard Evaluation Procedure

To illustrate the use of the procedure given above, four examples are presented in Table IX. The input parameters for these examples were selected to be as representative and realistic as possible and to cover a variety of conditions. Example 2 represents the conditions of an actual recent field experiment.

Table IX

EXAMPLES OF LASER EYE-HAZARD EVALUATION

Parameter	Example 1	Example 2	Example 3	Example 4	
A. SPECIFIED PARAMETERS					
Date	21 Dec	1 May	21 June	21 June	
Time	2200	1200	1500	1500	(LST)
Φ	30°N	40°N	20°S	20°S	
N	2	0	6	6	(tenths)
U	5	8	12	12	(knots)
V	20	8	20	20	(miles)
Path Type	Slant	Slant	Horiz.	Horiz.	
Laser Site	Airborne	Ground	---	---	
θ	60°	20°	0°	0°	
R	0.4	5	1	6	(km)
λ	0.4880	0.6943	1.06	1.06	(μ)
Q	---	0.5	10	10	(pulses/s)
β	0.5	0.5	0.5	0.5	(mrad)
d	2	---	---	---	(10^{-3}m)
P	1	2.5×10^{7}	10^{7}	10^{7}	(W)
T	1	0.1	0.1	0.1	(s)
Laser Type	CW	Q-sw.	Q-sw.	Q-sw.	
B. DERIVED PARAMETERS					
Step No.					
3	α	0°	60°	30°	30°	
4	S	---	Strong	Mod.	Mod.	
5	C_n	0.35	0.40	0.25	0.25	($10^{-6}m^{-1/3}$)
6	A	6×10^{3}	6×10^{5}	---	---	($m^{11/6}$)
7,8	σ	0.4	1.25	1.23	0.80	
9	$\bar{I}/P$	30	5×10^{-2}	4	9×10^{-2}	(m^{-2})
10	$\bar{I}$	30	1.25×10^{6}	4×10^{7}	9×10^{5}	(W/m^2)
11	I_{safe}	1.3×10^{2}	5.35×10^{6}	3.21×10^{8}	3.21×10^{8}	(W/m^2)
12	$I_{safe}/\bar{I}$	4.3	4.28	8.0	360	
13	γ	6×10^{-5}	4×10^{-2}	10^{-2}	10^{-14}	
14	Γ	2×10^{-2}	$>10^{-1}$	$>10^{-1}$	10^{-12}	
15	Safe ?*	no	no	no	yes	

*Based upon a selected value of $\Gamma_{safe} = 10^{-3}$.

Appendix

DERIVATION OF EQUATIONS FOR PROBABILITY OF EYE DAMAGE FROM A SINGLE EVENT

Let

$$\chi \equiv \ln (A/A_o) \qquad \text{(A-1)}$$

where

A = field amplitude

A_o = field amplitude reference value .

Now

$$I = A^2 \qquad \text{(A-2)}$$

where

I = field intensity .

Also, from Eq. (A-1),

$$A = A_o e^{\chi} ,$$

hence

$$I = A_o^2 e^{2\chi} \qquad \text{(A-3)}$$

Now we assume that χ is a normal random variable. This is equivalent to assuming that A/A_o follows a log-normal distribution. Then it can be shown (Mood, 1950) that the mean value of I is given by

$$\bar{I} = A_o^2 \overline{(e^{2\chi})} = A_o^2 \exp\left(2\bar{\chi} + 2\sigma_\chi^2\right) \qquad \text{(A-4)}$$

where $\bar{X}$ and σ_X^2 are the mean and variance of X.

We are interested in the event

$$I \geq I_{safe} \text{ , or } I/\bar{I} \geq I_{safe}/\bar{I} \text{ ,} \tag{A-5}$$

or from Eqs. (A-3) and (A-4),

$$\exp\left[2(X - \bar{X}) - 2\,\sigma_X^2\right] \geq I_{safe}/\bar{I} \quad . \tag{A-6}$$

This converts to

$$2(X - \bar{X}) - 2\,\sigma_X^2 \geq \ln\left(I_{safe}/\bar{I}\right)$$

or

$$(X - \bar{X})/\sigma_X \geq \left[\sigma_X^2 + 0.5 \ln\left(I_{safe}/\bar{I}\right)\right]/\sigma_X \quad . \tag{A-7}$$

If the instantaneous probability of eye damage, γ, is defined as

$$\gamma = \text{Prob}\left(I \geq I_{safe}\right) \quad ,$$

which is the probability that the event specified in Eq. (A-5) occurs, then from Eq. (A-7) this is equivalent to

$$\gamma = \text{Prob}\left\{(X - \bar{X})/\sigma_X \geq \left[\sigma_X^2 + 0.5 \ln\left(I_{safe}/\bar{I}\right)\right]/\sigma_X\right\} \quad . \tag{A-8}$$

Since $x = (X - \bar{X})/\sigma_X$ is simply a normally distributed variable with zero mean and unity variance, the probability represented by γ in Eq. (A-8) is equivalent to the area in the tail of a standard normal distribution beyond the point

$$M = \left[\sigma_X^2 + 0.5 \ln\left(I_{safe}/\bar{I}\right)\right]/\sigma_X \quad , \tag{A-9}$$

as given by

$$\gamma = \int_{M}^{\infty} \frac{1}{\sqrt{2\pi}} e^{-x^2/2} dx \quad . \qquad \text{(A-10)}$$

Since the relation between the log amplitude standard deviation (σ_χ) and the log intensity standard deviation (σ) is

$$\sigma_\chi = \sigma/2 \quad ,$$

we can also write M as

$$M = \sigma/2 + \sigma^{-1} \ln\left(I_{safe}/\bar{I}\right) \quad . \qquad \text{(A-11)}$$

REFERENCES

Davis, J. I., 1966: Consideration of Atmospheric Turbulence in Laser Systems Design. Appl. Opt., 5, 139-147.

Deitz, P. H., 1968: Twelve Eye Safety Nomographs. Technical Note No. 1709, Ballistic Research Laboratories, Aberdeen Proving Ground, Maryland.

Deitz, P. H., 1969: Probability Analysis of Ocular Damage Due to Laser Radiation Through the Atmosphere. Appl. Optics, 8, 371-375.

Deitz, P. H. and N. J. Wright, 1969: Saturation of Scintillation Magnitude in Near-Earth Optical Propagation. J. Opt. Soc. Amer., 59, 527-535.

DeWolf, D. A., 1968: Saturation of Irradiance Fluctuations Due to Turbulent Atmosphere. J. Opt. Soc. Am., 58, 461-466.

Fried, D. L., G. E. Mevers and M. P. Keister, Jr., 1967: Measurements of Laser Beam Scintillation in the Atmosphere. J. Opt. Soc. Am., 57, 787-797.

Goldstein, I., P. A. Miles and A. Chabot, 1965: Heterodyne Measurements of Light Propagation Through Atmospheric Turbulence. Proc. IEEE, 1172-1180.

Gracheva, M. E., 1967: Izv. VUZ, Radiofizika, 10, 775.

Gracheva, M. E. and A. S. Gurvich, 1965: Strong Fluctuations in the Intensity of Light Propagated Through the Atmosphere Close to the Earth. Radiofizika, 8, 717-724.

Johnson, W. B., Jr., J. K. Omura and A. Vassiliadis, 1968: Atmospheric Effects--Laser Safety Criteria (U). Final Report, Contract F33615-67-C-1959, AFAL-TR-68-243, SRI Project 6725, Stanford Research Institute, Menlo Park, California, CONFIDENTIAL.

Kerr, J. R., 1970: Multiwavelength Laser Propagation Study--II. Quarterly Progress Report No. 2, ARPA Order No. 306, Oregon Graduate Center for Study and Research, Portland, Oregon.

Mevers, G. E., M. P. Keister, Jr. and D. L. Fried, 1969: Saturation of Scintillation. Paper presented at 1969 Spring Meeting, Opt. Soc. of Amer., San Diego, 12 March 1969.

Mood, A. M., 1950: Introduction to the Theory of Statistics. McGraw-Hill Book Co., New York, 433 pp.

Ochs, G. R., 1969: Atmospheric Effects on a Laser Beam in Strong Turbulence. Paper presented at 1969 Spring Meeting, Opt. Soc. of Amer., San Diego, 12 March 1969.

Ryznar, E., 1965: Dependency of Optical Scintillation Frequency on Wind Speed. Appl. Opt., 4, 1416-1418.

Slade, D. H. (Editor), 1968: Meteorology and Atomic Energy. USAEC Division of Technical Information, Oak Ridge, Tennessee. (TID-24190, CFSTI, National Bureau of Standards, U.S. Dept. of Commerce, Springfield, Virginia).

Smithsonian Meteorological Tables, 1963: Publication 4014, The Smithsonian Institution, Washington, D.C. (R. J. List, Editor).

Tatarski, V. I., 1961: Wave Propagation in a Turbulent Medium. Translated by R. A. Silverman (McGraw-Hill Book Company, Inc., New York, New York).

Tatarski, V. I., 1966: On Strong Fluctuations of Light Wave Parameters in a Turbulent Medium. Soviet Physics JETP, 22, 1083-1088.

USAF AFM 161-8, 1969: Laser Health Hazards Control. School of Aerospace Medicine, U.S. Air Force, Brooks AFB, Texas.

Vassiliadis, A., R. C. Rosan and H. C. Zweng, 1969: Research on Ocular Laser Thresholds. Final Report, Contract F41609-68-C-0041, SRI Project 7191, Stanford Research Institute, Menlo Park, California.

World Almanac, 1970: Newspaper Enterprises Association, Inc., 230 Park Ave., New York, New York 10017, p. 73.

Wright, N. J. and R. J. Schutz, 1967: Measurements of the Refractive Index Structure Coefficient C_n. Memo. Report No. 1885, Ballistic Research Laboratories, Aberdeen Proving Ground, Maryland.

ABSTRACT (continued)

either a ground-based or airborne laser, as well as near-ground horizontal propagation. The airborne-laser slant-path configuration is shown to give the lowest eye-damage probability, other factors being the same.

UNCLASSIFIED

Security Classification

DOCUMENT CONTROL DATA - R & D

(Security classification of title, body of abstract and indexing annotation must be entered when the overall report is classified)

1. ORIGINATING ACTIVITY (Corporate author) Stanford Research Institute Menlo Park, California 94025	2a. REPORT SECURITY CLASSIFICATION Unclassified 2b. GROUP

3. REPORT TITLE

ATMOSPHERIC EFFECTS UPON LASER EYE SAFETY (PART I)

4. DESCRIPTIVE NOTES (Type of report and inclusive dates)

Final Report

5. AUTHOR(S) (First name, middle initial, last name)

Warren B. Johnson, William E. Evans, Edward E. Uthe

6. REPORT DATE April 1970	7a. TOTAL NO. OF PAGES 124	7b. NO. OF REFS 22
8a. CONTRACT OR GRANT NO. F41609-69-C-0001 new b. PROJECT NO. c. d.	9a. ORIGINATOR'S REPORT NUMBER(S) SRI Project 7472 9b. OTHER REPORT NO(S) (Any other numbers that may be assigned this report)	

10. DISTRIBUTION **This document is subject to special export controls and each transmittal to foreign governments or foreign nationals may be made only with prior approval of USAFSAM(RAT), Brooks AFB, TX, 78235.**

11. SUPPLEMENTARY NOTES	12. SPONSORING MILITARY ACTIVITY United States Air Force School of Aerospace Medicine Aerospace Medical Division Brooks Air Force Base, Texas

13. ABSTRACT

The results of two laser scintillation experiments in the atmosphere are presented, as is a revised laser eye-hazard evaluation procedure incorporating these results. The objective of the research is to determine the influence of atmospheric thermal turbulence on laser eye safety.

The experimental work on a 3.5-km near-ground horizontal propagation path was designed to determine the effect of range upon laser scintillation magnitude, represented by the log intensity standard deviation (σ). It was found that for very short ranges and low thermal turbulence, the measured values (σ_m) agree well with theory (σ_t). However, for longer ranges and higher thermal turbulence, the values of σ_m reached a maximum value of approximately 1.25 at $\sigma_t = 2.50$, and then decreased beyond, fitting the empirical function $\sigma_m = \sigma_t/(1 + 0.16\sigma_t^2)$ fairly well. This "supersaturation effect" is quite significant in reducing eye-damage probabilities for typical ranges and thermal turbulence conditions.

The second experiment was an attempt to confirm that scintillation saturation occu on a slant path between a ground-based laser and a receiver on an orbiting aircraft. Some evidence of saturation was found, but the effect was not clearly established because of the limited ranges necessitated by the laser used.

The eye-hazard evaluation procedure is quite generally applicable, and requires only readily available input data. The method covers propagation on a slant path wit

DD FORM 1 NOV 65 1473 (PAGE 1)

S/N 0101-807-6801

UNCLASSIFIED

Security Classification

UNCLASSIFIED

Security Classification

14 KEY WORDS	LINK A ROLE	LINK A WT	LINK B ROLE	LINK B WT	LINK C ROLE	LINK C WT
Laser propagation						
Eye safety						
Light scintillation						
Atmospheric turbulence						
Laser safety						
Atmospheric effects						

DD FORM 1 NOV 65 1473 (BACK)

(PAGE 2)

UNCLASSIFIED

Security Classification